REDOX STATE OF ECLOGITE XENOLITHS FROM THE WESTERN KAAPVAAL CRATON (BELLSBANK AND BOBBEJAAN KIMBERLITES)

David Robert Greyling

Supervisor: Dr Katie Smart – Department of Geoscience, University of the Witwatersrand
Co-Supervisor: Prof Sebastian Tappe – Department of Geology, University of Johannesburg

A dissertation submitted to the Faculty of Science, University of the Witwatersrand, in partial fulfilment of the requirements for the degree of Master of Science

Johannesburg, 2020

CONTENTS **PAGE**

DECLARATION

I declare that this dissertation is my own, unaided work. It is being submitted for the Degree of Master of Science at the University of the Witwatersrand, Johannesburg. It has not been submitted before for any degree or examination at any other University.

(Signature of candidate)

17th day of August 2020 at Johannesburg

ABSTRACT

Mantle eclogite xenoliths from the Bellsbank and Bobbejaan Group II ca. 118 Ma kimberlite located on the western margin of the Kaapvaal craton, South Africa, show geochemical and stable isotopic evidence for a protolith derived from recycled oceanic crust. The xenoliths (n = 26) represent a geochemically diverse suite of kyanite, corundum and bi-mineralic eclogites. The eclogite xenoliths were classified as Gabbroic, High-Mg and High-Ca based on bulk rock Eu anomalies and garnet major element chemistry. Gabbroic samples resemble modern ocean gabbro in terms of whole-rock major element composition, having distinct positive Eu anomalies (Eu* = 1.10 – 2.59), and flat to mildly fractionated HREE patterns (Lu/Gd = 1.0 – 4.7). High-Mg and High-Ca samples are basaltic-picritic in composition, have less pronounced Eu anomalies (Eu* 0.68 – 1.05), and show less fractionated HREE patterns comparable to an Archean picrite. Stable isotope data and forward modelling reveal paragenesis by subduction of ocean gabbro and basalt, followed by partial melting and kimberlite related metasomatism. Garnet $\delta^{18}O$ values range between +2.74 and +6.25 ± 0.12 ‰. Corrected $Fe^{3+}/\Sigma Fe$ contents are variable from 0.009 to 0.039 ± 0.01. Gabbroic eclogites have equilibrium pressures and temperatures (3.4 - 5.6 GPa and 860 - 1194 °C) slightly lower than High-Mg samples (4.5 - 6.0 GPa and 1028 to 1259 °C). Determined oxygen fugacity (fO_2) of the xenoliths follows known depth trends, with values between -1.4 to -4.2 log units below the Fayalite-Magnetite-Quartz (FMQ) buffer corresponding to depths ~ 100 – 200 km within the Kaapvaal CLM. Oxidative metasomatism has obscured the systematic decrease in oxygen fugacity with depth trend, whereby diamond-stable eclogite xenoliths have been oxidized to carbonate stable conditions. The cause and extent of this potentially diamond-destructive metasomatism remains speculative, however appears to be concentrated ~200 km within the Kaapvaal CLM.

ACKNOWLEDGMENTS

I would first and foremost like to thank Dr. K. Smart for her supervising of this project, and for sharing her excellent knowledge of mantle eclogites with me. I would also like to thank Prof. S. Tappe for his valuable input as a co-supervisor, for organizing field work to the Bellsbank kimberlite and the visit to Finsch diamond mine.

Thank you to the National Research foundation for providing funding, through CIMERA, for this project. It would not have been possible without them and I am forever grateful for that.

I would also like to thank my colleagues, the academic staff at WITS as well as my friends and family for the support offered throughout this project.

LIST OF FIGURES

Figure 6: Calculated whole rock multi-element variation diagrams depicting compositions (wt. %) of Bellsbank and Bobbejaan eclogites. Global MORB data shown by the blue stippled line from Jenner & O'Niel., (2012). Altered and fresh modern oceanic gabbro compositions shown by the green field from Bach et al. (2001). Ventersdorp mafic volcanics (yellow squares) from Crow and Condie. (1988), Marsh et al. (1992). Picrite from Eggins (1993). **(a)** Comparative Al_2O_3 vs. MgO plot showing Bellsbank and Bobbejaan eclogites broadly plotting close to oceanic gabbro and MORB fields, although many gabbroic eclogites have elevated Al_2O_3 contents. High-Mg samples plot close to picrite compositions and fall outside of the field for oceanic gabbro and MORB. **(b)** Na_2O vs. MgO reveals a close association of the gabbroic and high-Ca eclogite samples with modern oceanic gabbro and MORB fields. High-Mg samples plot closer to picrite compositions. **(c)** FeO vs. MgO plot showing gabbroic and high-Ca eclogites plotting close to samples from modern oceanic gabbro and MORB. **(d)** SiO_2 vs. MgO plot showing gabbroic, high-Mg and high-Ca samples plot outside of the fields for modern oceanic gabbro and MORB. Trend lines depict fractionation trends modelled at 1 GPa (black line) and 3 GPa (black stippled line) using pMelts software (Ghiorso et al., (2002) from starting composition (red star). Data from partial melting experiments of Yaxley and Sobolev. (2007) shown in (d). Kaapvaal eclogite compositions calculated from (MacGregor and Manton, 1986; Ongley et al., 1987; Caporuscio and Smyth, 1990; Appleyard et al., 2004; Viljoen et al., 2005; Jacob et al., 2009; Gréau et al., 2011; Aulbach and Viljoen, 2015; Riches et al., 2016b; Shu et al., 2016; Aulbach et a., 2016; Huang et al., 2016; Aulbach, Woodland, et al., 2017). Eclogites have been classified into gabbroic, high-Mg and high-Ca groups after Aulbach and Jacob (2016). See section 3.4 for further classification details. Further details on partial melt modelling (d) and pMelts forward modelling (a - c) can be found in section 4.2.2 33

Figure 7: Calculated bulk eclogite multi-element diagram normalized to primitive mantle (values from McDonough, Sun, 1995). Gabbroic eclogites plotted in **(a)** and non-gabbroic (see section 3.4 for classification details) eclogites plotted in **(b)**. REE primitive mantle normalized plots of gabbroic eclogites plotted in **(c)** and non-gabbroic eclogites in **(d)**. The eclogites have been further grouped according to their oxygen isotope composition (Table 2) in comparison to the known $\delta^{18}O$ value of the mantle (+5.5 ± 0.4‰; Mattey et al., 1994). Blue solid circles: gabbroic eclogites with $\delta^{18}O$ values < +5.1 ‰; yellow solid circles: non-gabbroic eclogites with $\delta^{18}O$ values within the mantle range (+5.1 to +5.9 ‰); red solid circles: non-gabbroic eclogites with $\delta^{18}O$ values < +5.1 ‰; green lines non-gabbroic eclogites with $\delta^{18}O$ values >+5.9 ‰. Grey field in a) and c) shows metasomatized eclogites from Robert Victor kimberlite Radu et al., (2019). Yellow field in b) and d) shows non-metasomatized eclogites from Robert Victor kimberlite Radu et al., (2019). Black stippled line (Type A) and blue stippled line (Type B) represent metasomatized eclogite average whole rock compositions from Jacob et al., (2009). 34

Figure 8: Equilibration pressures and temperatures for the Bellsbank and Bobbejaan eclogite xenoliths based on the Fe-Mg exchange thermometer of Krogh Ravna (2000) (T_{KR}) iteratively with the Finsch peridotite derived geotherm (P_{FPG}) using data from Lazarov et al., (2009) and Skinner, (1989). Blue plus symbols: equilibration pressures and temperatures for the Bellsbank and Bobbejaan eclogite xenoliths based on the Fe-Mg exchange thermometer of Krogh Ravna (2000) (T_{KR}) solved iteratively with the barometer of Beyer et al., (2015) (P_{B15}) starting at an assumed pressure of 5 GPa. Blue squares: pressure and temperature results for Bellsbank and Bobbejaan eclogites from Shu et al., (2014). Grey region: published eclogite compositions from the Kaapvaal craton (MacGregor and Manton, 1986; Ongley et al., 1987; Caporuscio and Smyth, 1990; Appleyard et al., 2004; Viljoen et al., 2005; Jacob et al., 2009; Gréau et al., 2011; Aulbach and Viljoen, 2015; Riches et al., 2016b; Shu et al., 2016; Aulbach et al.,

LIST OF TABLES

CHAPTER ONE – INTRODUCTION

1.1 Overview and motivation

This project aims to investigate the redox state of mantle eclogite xenoliths from the Kaapvaal craton of southern Africa and the diamond potential of eclogite in the lithospheric mantle. Eclogitic mantle xenoliths are bimineralic rocks derived mainly from kimberlite intrusions. They serve as important indicators of geodynamic processes within the Earth's upper mantle through time, due to their potential link with the crust (Jacob, 2004). Mantle eclogites are plagioclase-free metamorphic rocks consisting mostly of clinopyroxene (omphacite-jadeite) and garnet (pyrope-grossular-almandine). They have mafic bulk compositions and record equilibration pressures and temperatures that are typical of the conditions within cratonic lithospheric mantle (Coleman *et al.*, 1965; Jacob, 2004).

The origins of mantle eclogites have been debated for decades; however, they have either been considered to have formed as high pressure cumulates from basaltic melts within the upper mantle (Green and Ringwood, 1967; O'Hara *et al*., 1975; Barth *et al.*, 2002; Griffin and O'Reilly, 2006), or as subducted oceanic crust recycled into the upper mantle (Helmstaedt and Doig, 1975; Jacob *et al.*, 1994; Barth *et al.*, 2001; Jacob, 2004; Smart *et al.*, 2014a; Aulbach and Viljoen, 2015). Detailed geochemical and $\delta^{18}O$ isotope studies of mantle eclogites have revealed strong links to ancient recycled oceanic crust, with radiometrically-constrained formation ages as old as the Neoarchean (Jacob and Foley, 1999; Jacob *et al*., 2003; Schmidberger *et al.*, 2005; Tappe *et al.*, 2011), making the study of mantle eclogites crucial to the understanding of crust-mantle interaction through time.

Mantle eclogites reside within cratonic lithospheric mantle (CLM), which represents the chemically depleted, relatively cool and stable lithospheric

roots that underlie Archean to Paleoproterozoic cratonic crust (Lee *et al.*, 2011). Less than 1% to 4% of the CLM consists of eclogite, based on xenocryst studies (Schulze, 1989; McLean *et al.*, 2007). However, nearly one third of naturally occurring diamonds from primary deposits are eclogitic in origin (Stachel and Harris, 2008). Mantle eclogites are thus a significant host for diamonds and an economically important diamond source rock.

The links between mantle eclogite and diamond formation are intriguing yet unresolved. Two pertinent factors in diamond formation and preservation are the oxygen fugacity of potential diamond host rocks and subsequent secondary processes affecting the CLM such as melt/fluid-driven metasomatism (Creighton *et al.*, 2009; Smart *et al.*, 2012; Stachel and Luth, 2015; Stagno *et al.*, 2015). Oxygen fugacity refers to the activity of oxygen in a multicomponent system and is reported relative to a buffer, the most frequently applied being the Fayalite-Magnetite-Quartz (FMQ) buffer (Frost and McCammon, 2008). The redox state of the Earth's mantle has important implications for the initiation of partial melting (Yaxley *et al.*, 2017), the compositions of partial melts produced (Foley, 2011), and, of importance to this study, the speciation and stability of carbon and its compounds (Woodland and Koch, 2003; Stagno *et al*., 2015).

Oxygen fugacity directly determines both the carbon species involved in the formation of diamond and the suitability of eclogite as diamond host (Stagno *et al.*, 2015). Diamond may form during redox reactions involving carbon-bearing melts or fluids. Diamond stability within the CLM requires relatively reducing conditions with secondary oxidative metasomatic events being typically considered as diamond destructive (Shirey *et al*., 2004; Stachel and Luth, 2015). The strong association between diamond and eclogite relates to the transition from carbonate to diamond stable conditions at favourable redox conditions, specifically at around 1 log unit above the Enstatite-Magnesite-Forsterite-Graphite/Diamond (EMOD) buffer curve (Stachel and Luth, 2015). The redox state of the mantle is known to decrease with depth, resulting in the deeper lithospheric mantle being more reducing (Frost and McCammon, 2008). Investigations on CLM-derived

peridotites are characterized by a decrease in oxygen fugacity with increasing depth (Woodland and Koch, 2003). The oxidation state of the CLM is, however, laterally and vertically heterogeneous (Creighton *et al.*, 2009), whereby CLM peridotites deviate from a systematic oxygen fugacity versus depth trend due to possibly oxidative metasomatic effects (Creighton *et al.*, 2009; Yaxley *et al.*, 2017). This has been found to be destructive to diamonds within the CLM (Stachel and Luth, 2015). It therefore becomes pertinent to understand the redox states of peridotites and eclogites before being able to understand the formation and preservation of diamond in the lithospheric mantle.

This project will be focused on the redox state and diamond potential of the eclogitic composition of the western Kaapvaal lithospheric mantle. Mantle-derived eclogite xenoliths from the Bellsbank and Bobbejaan kimberlites are discussed herein to investigate how the redox states of these eclogite xenoliths relate to the diamond potential of the eclogitic portion of the CLM. This is accomplished through detailed petrological, mineral chemistry, thermobarometry and stable isotope geochemistry analyses. Constraining the redox states of the Kaapvaal CLM and its spatial variability will add to models for cratonic lithosphere formation and evolution, as well as provide further insights into some of the factors that influence diamond forming processes in nature.

1.2 Previous studies

1.2.1 Geology of the Kaapvaal craton

The Bellsbank and Bobbejaan kimberlite dykes are located within the Barkley West district of the Northern Cape province in South Africa, approximately 110 km NW of Kimberley (Figure 1). The 120 - 110 Ma dyke and fissure systems strike N30°E and are hosted within Paleoproterozoic

Campbellrand dolomites of the Transvaal Supergroup on the western terrane of the Kaapvaal craton (Smith et al., 1985; Mitchell, 1995; Gurney and Kirkley, 1996).

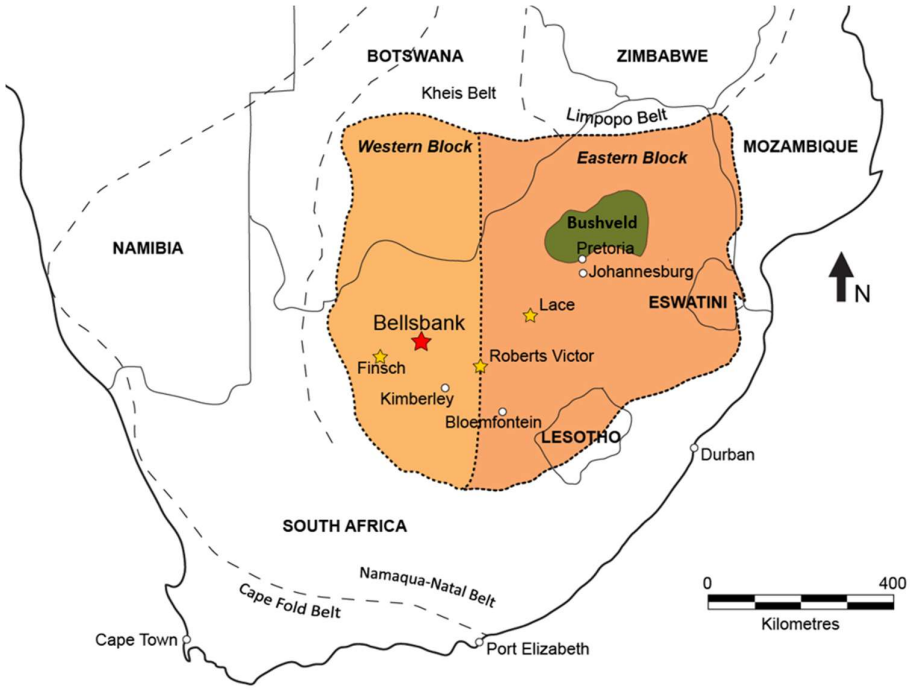

Figure 1. *Map of southern Africa showing position of the Kaapvaal craton. Brown: eastern-block; Orange: western block; green – Bushveld complex. The 120 - 110 Ma Bellsbank kimberlite is shown with a red star: Group 2 kimberlites with ages of approximately 120 Ma (e.g. Finsch, Roberts Victor and Lace) are indicated with yellow stars. Map modified after Griffin et al. (2003).*

The Kaapvaal craton hosts well preserved Archean fragments of continental crust and hence provides a wealth of information about the processes responsible for their formation. A two-stage craton formation model has been proposed by De Wit *et al.* (1992). The first stage occurred between 3.7 - 3.1 Ga as the separation of continental lithosphere from the ambient upper mantle by plate tectonic processes similar to those occurring in modern ocean basins. The second stage is continental growth at convergent plate margins between 3.1 - 2.6 Ga with subduction and collisions plus associated felsic crust forming igneous activity.

The oldest rocks of the Barberton Greenstone Belt, the Ancient Gneiss Complex (ca. 3.68 Ga), arguably form the nucleus of the Kaapvaal craton (Kröner *et al.,* 1996). Continued volcanism and sedimentation until the end of the Moodies Group deposition (ca. 3.22 Ga) was followed by increased

plutonic activity, marked by terrane accretion (Anhaeusser, 2006). The stabilizing 'cratonic' nucleus was able to support sedimentary deposition into the Dominion, Witwatersrand and Pongola basins (ca. 3.0 – 2.8 Ga) until onset of the Ventersdorp volcano-sedimentary succession, which extended across the eastern (Witwatersrand block) and western (Kimberley block) Kaapvaal craton (England *et al.,* 2001; Eglington and Armstrong, 2004; Eriksson *et al.,* 2011).

Limpopo mobile belt granulites (ca. 2.67 Ga) to the north provide evidence for regional orogenic activity, which facilitated the development of syn-tectonic and post-tectonic granitoids on the Kaapvaal craton. This was followed by protracted Transvaal Supergroup deposition on the craton, lasting until the Rooiberg Group volcanics (ca. 2.057 Ga) extruded coeval to the Bushveld Complex igneous activity (ca. 2.056 Ga) (Eriksson *et al.,* 2001, 2011; Zeh *et al.,* 2015). Subsequent to emplacement of the Bushveld Complex, extensive terranes and mobile belts developed along the Kaapvaal craton margins during the Kheis (ca. 1.9 Ga), Kibaran (ca. 1.2 Ga) and Namaqua-Natal (ca. 1.1 Ga) orogonies (Jacobs and Thomas, 1996; Moen, 1999; Eglington and Armstrong, 2004; McCourt *et al.,* 2006; Cornell, 2017). Along the western margin of the Kaapvaal craton, kimberlite intrusions discordantly cut across thick sedimentary and volcanogenic back-arc rock assemblages associated to the Karoo supergroup.

The Palaeozoic-Mesozoic Karoo Supergroup (300 to 180 Ma) sedimentary and volcanic rocks are commonly intruded by kimberlites on the western Kaapvaal craton (Johnson *et al*., 1996; le Roex, 2003; McKay *et al*., 2015).

Group I kimberlite magmatism on the Kaapvaal craton is characterised by a wide range of eruption ages (e.g., Cretaceous, Permian, Cambrian, and Proterozoic) (Griffin *et al*., 2014; Tappe *et al*., 2018). The geochemical signatures of these kimberlite suggest that they are derived from the asthenospheric mantle, with possible relations to hot-spot volcanic activity (Becker and le Roex, 2006; Mitchell, 1995). In contrast, Group II kimberlite magmatic activity occurred over a much shorter time period between 200

and 110 Ma (for a summary see Tappe *et al*., 2018). These more potassic kimberlite varieties have, geochemical signatures suggestive of derivation from old metasomatized lithospheric mantle (Bosch, 1971; Smith *et al.,* 1985; Mitchell, 2006). The eclogite xenolith-bearing Bellsbank and Bobbejaan dykes near Kimberley studied here are typical Group II kimberlites of the Kaapvaal craton (Mitchell, 1995).

1.2.2 Kaapvaal craton mantle lithosphere

A major goal with developing a comprehensive model for diamond formation is to relate the structure of the lithosphere to the age and chemical variation of diamonds, peridotites and eclogites (Shirey *et al*., 2004).

Early work on the Kaapvaal lithosphere argued that peridotites with low equilibration temperatures (< 1100 °C) are strongly depleted in Fe, have similar olivine content (45 – 80 wt. %) to fertile pyrolite, and originated as residue of partial fusion events (Boyd and Mertzman, 1987). High temperature peridotites (> 1100 °C) have increased modal olivine and garnet, with compositions akin to basalt, suggesting to have originated from subducted ocean crust. Boctor and Boyd, (1982) argue this subduction could coincide with the formation of the Namaqua-Natal mobile belt (ca. 1 Ga). The recycling of subducted components is further argued as a possible way in which some of the low-temperature Kaapvaal craton peridotites formed (Simon *et al.,* 2007). Peridotite xenoliths from the Group II Finsch kimberlite pipe have calculated temperatures (1080 – 1160 °C) and pressures corresponding to the diamond stability field, coarse textures with low modal garnet, and are suggested to represent a residue of the upper mantle (Skinner, 1989). The ~2.6 Ga Finsch peridotites are thought to represent Kaapvaal lithospheric mantle, which is the residue of adiabatic decompressive melting between 1.5 to 4.5 GPa (Lazarov *et al*., 2012), followed by related metasomatic enrichment (Gibson *et al*., 2008).

Petrogenesis of Group I kimberlites from the Kimberley area involves phlogopite metasomatism of the SCLM by a fluid or melt which is later partially melted (~1%) by an upwelling mantle plume to produce kimberlite magma with similarities to ocean island basalt (OIB) (le Roex, 2003). The Group II Bellsbank kimberlite contains an abundance of phlogopite as macrocrysts, groundmass and aggregates. Groundmass phlogopite is likely derived from late-stage kimberlite fluids post emplacement, whereas macrocrystic phlogopite is considered to have crystallized from the kimberlitic magma. The kimberlitic magma is derived from a garnet lherzolite source that was affected by metasomatism through equilibrium with LREE-enriched and CO_2 rich vapours (Boctor and Boyd, 1982).

Geophysical methods have more recently found evidence supporting the presence of a stalled segment of oceanic lithosphere beneath the southern margin of the Namaqua-Natal mobile belt, which further supports a basalt related formation of the cratonic lithosphere (Wang *et al.,* 2019).

The present-day Kaapvaal craton is underlain by a thick lithospheric mantle that has been intensively studied over time. Peridotite mantle xenoliths derived from the Kimberley, Newlands and Finsch kimberlite pipes show an abundance of known model ages (ca. 2.9 Ga) coinciding with age of the 'suturing' of the western and eastern blocks (Schmitz *et al.,* 2004). Moreover, sulphide diamond inclusion data provides evidence for a MORB like protolith, suggesting the subduction of oceanic crust to eclogite-facies at ca. 2.9 Ga (Aulbach *et al.,* 2009).

Eclogite xenoliths investigated from a variety of kimberlites on the Kaapvaal craton reveal broadly oceanic crustal protoliths and Archean formation ages (Neal *et al.,* 1990; Jacob, 2004; Aulbach and Viljoen, 2015).

1.2.3 Previous investigations of eclogite xenoliths from the Bellsbank kimberlite

Eclogite xenoliths from the ca. 118 Ma Bellsbank and Bobbejaan Group II kimberlite have previously been investigated for their geochemical compositions. The textural and geochemical characteristics of these economically important rocks have been well described since the 1970's (MacGregor and Carter, 1970; McCandless and Gurney, 1989; Neal *et al.,* 1990). Macgregor and Carter (1970) have on a textural basis classified Type I eclogites as having subhedral or rounded garnets in a clinopyroxene matrix, occasionally displaying layering. In contrast, they classify Type II eclogites as having anhedral garnet and an interlocking texture between garnet and clinopyroxene. Jacob (2004) suggests that classic textural classification schemes based on southern African eclogite samples can be successfully applied to most eclogite suites worldwide, however, the trace element based classification scheme provided by Aulbach and Jacob (2016) is employed here (see section 3.4).

An investigation on a suite of 62 Bellsbank eclogite xenoliths including kyanite and corundum bearing samples, revealed crystallization temperatures of 1350 to 1550°C and pressures of 3 to 5 GPa (Smyth and Caporuscio, 1984). Smyth *et al*. (1989) proposed a model in which mantle eclogites from the Bellsbank kimberlite evolved from grospydites to bimineralic eclogites at high pressures by igneous fractionation, despite $\delta^{18}O$ values (+2.2 to +8.5 ‰) giving evidence for a low pressure origin. The authors ultimately put forward a model to explain $\delta^{18}O$ values by low-temperature alteration of ocean crust, subduction and subsequent melting. A positive Eu anomaly in Group C eclogites from the Bellsbank kimberlites is suggested to support the role of plagioclase in their petrogenesis (Taylor and Neal, 1993).

The Bellsbank eclogite samples classified as Group A display evidence in support of petrogenesis by fractional crystallization of basalt or komatiite.

Group B and C xenoliths are suggested to represent the metamorphosed products of ancient subducted oceanic crust (Neal *et al.,* 1990). Group A eclogites are characterized by low jadeite content in clinopyroxene, with Mg and Cr rich garnet. Group B eclogites have moderate jadeite content in clinopyroxene, and Fe rich garnet. Group C eclogites have high clinopyroxene jadeite content, and Ca rich garnets.

Group A eclogites have $\delta^{18}O$ (+4.8 to +5.1 ‰) and $^{87}Sr/^{86}Sr$ (0.7042 – 0.7046) values as typical for mantle derived materials as well as REE (very low Sm/Nd) and isotope signatures which can be modelled as crystallising from a Group II kimberlite magma (ca. 1 – 1.5 Ga) (Neal *et al.,* 1990). Group B and C eclogites have $\delta^{18}O$ (+2.9 to +4.7 ‰) and $^{87}Sr/^{86}Sr$ (0.708 – 0.710) values typical for Archean subducted ocean crust, with elevated REE (Sm/Nd = 1.6) patterns indicative of cryptic metasomatism and re-crystallization of MORB during eclogite subduction ca. 2.4 Ga (Neal *et al.*, 1990).

Viljoen (1995) presents graphite $\delta^{13}C$ values (-7 to -2.8 ‰) for diamond and graphite bearing eclogite xenoliths, which is in the range for inclusion free Bellsbank kimberlite derived diamonds. The authors therefore suggest a shared source of carbon at equilibrium temperatures (1150 °C) and pressures (5 GPa).

More recent studies on eclogites and garnet pyroxenites from the Bellsbank kimberlite have revealed a range of equilibrium temperatures (842 - 1173 °C) and pressures (3.7 GPa - 6.3 GPa), as well as Sm-Nd two point isochron ages corresponding to a geothermal gradient between 46 mW/m^2 to 38 mW/m^2 at 120 Ma (Shu *et al.,* 2014). Studies on peridotite xenoliths from the Group II Finsch kimberlite (ca. 118 Ma) reveal a geothermal gradient between 40 mW/m^2 and 41 mW/m^2 down to ~200 km depth, which makes it reasonable to assume a similar geothermal gradient for the nearby Bellsbank kimberlite (Lazarov *et al.*, 2009).

Furthermore, positive Eu anomalies combined with low REE abundances and $\delta^{18}O$ values lower than that for earth's mantle are used to argue for a

low-pressure cumulate origin for some Bellsbank kimberlites, with plagioclase and olivine as major cumulate phases (Shu *et al.,* 2016). The authors found a minimum age of 3.2 Ga for two of the eclogite xenoliths and argued for kyanite and corundum bearing samples having originated as plagioclase-free high pressure cumulates of highly aluminous clinopyroxene, spinel and olivine.

1.2.4 Redox states of the Kaapvaal craton mantle lithosphere

Although diamond-bearing eclogite xenoliths and eclogitic diamond inclusions are well known from the Kaapvaal craton (Stachel and Harris, 2008), there is to date limited work compiled on the oxidation state of the eclogite host rocks.

Early investigations on garnet and spinel peridotites from the Kaapvaal craton which covered a depth range of 80 - 220 km revealed a systematic decrease in oxygen fugacity (fO_2) with depth. The decreasing oxygen fugacity with depth trend was found to be greater between 80 - 150 km (~ 3 log units), than at deeper intervals between 150 - 220 km (~ 0.8 log units) (Woodland and Koch, 2003). While the decreasing oxygen fugacity with depth trend can be understood as a crystal-chemical affect due to the incorporation of Fe^{3+} into garnet, the authors argue that variable oxygen fugacity with depth is connected to oxidative metasomatism. That is, at deeper portions of the upper Kaapvaal CLM, redox melting facilitates the upward migration of CH_4-rich fluids into more oxidized peridotite.

Peridotite xenoliths from Finsch kimberlite on the western Kaapvaal craton were mostly found to demonstrate mineral equilibrium at temperatures from 1050 - 1250°C and pressures between 4.4 - 6.5 GPa. The authors found a distinct decrease with oxygen fugacity with depth (~ 1.0 log unit per GPa) for the sample group which had fO_2 values between -2.5 to -4.7 (FMQ) (Lazarov *et al*., 2009).

Creighton *et al.* (2009) also found the Kaapvaal CLM to be progressively more reduced with depth, whereby with fO_2 values approach -4 (FMQ) at depths ~210 km. They argue that oxidation driven by metasomatism obscures the crystal chemical-controlled depth trend, which causes portions of the CLM to oxidize to such an extent that diamond would be converted into carbonate. A study on Wesselton kimberlite derived peridotite xenoliths also found a link between metasomatism and diamond-destructive oxidation within the Kaapvaal CLM, and suggest a potential source of the oxidation to be a carbonated silicate melt (Hanger *et al.,* 2015).

The only published oxygen fugacity investigation of eclogite xenoliths from the Kaapvaal craton is on a suite of eclogites from the (ca. 132 Ma) Lace kimberlite on the eastern block's Kroonstad cluster. These eclogite xenoliths are argued to have formed from the low-pressure fractionation of oceanic crust, followed by partial melt loss during subduction and eclogitisation (Aulbach and Viljoen, 2015). Aulbach *et al.* (2017) used $Fe^{3+}/\sum Fe$ data and two oxybarometers (Stagno *et al.,* 2015; Vasilyev, 2016) to determine fO_2 values between -1.3 and -4.6 (FMQ) for the Lace eclogite xenoliths. The reducing conditions demonstrated are argued imply that diamond would have formed from methane rich fluids migrating into the ambient mantle during redox melting in the Archean.

1.3 Aim

Determine the redox state of 26 Bellsbank and Bobbejaan eclogite xenoliths, while developing a holistic petrogenetic model of these eclogite xenoliths, in order to understand how this relates to the diamond potential and formation of the eclogitic portion of the Kaapvaal cratonic lithospheric mantle. The specific goals of this project include:

- Classification of eclogites by petrographic and geochemical schemes.

- Determine the major and trace element composition, oxygen isotopic composition and equilibration pressure and temperature conditions of the eclogite samples.
- Comparison of the Bellsbank and Bobbejaan eclogites to other eclogite suites from the Kaapvaal craton and selected cratons worldwide, to assess both the petrogenesis of the eclogite suite and the understanding of craton formation and evolution.
- Determine garnet Fe^{3+} content by Mössbauer spectroscopy and calculate oxidation states of the eclogites.
- Evaluate the redox states of the Bellsbank and Bobbejaan eclogites in order to (a) assess diamond potential, (b) compare to host peridotitic cratonic lithospheric mantle to gain an understanding of the role of metasomatism, and (c) contrast with other eclogite suites in other parts of the Kaapvaal craton and worldwide.

1.4 Hypothesis

The underlying working hypothesis of the here proposed study is that a prominent negative correlation exists between the redox state of cratonic mantle materials (e.g. peridotites and eclogites) and their depths of residence within the lithosphere. Deviations from this trend have been observed in the past for many cratons and evidence has been presented that oxidative metasomatism may obscure the first-order crystal chemically controlled fO_2 – depth relationship. During the here proposed study it will be attempted to establish the position of classic eclogite xenoliths suites from the western Kaapvaal craton in fO_2 – depth space, and to explain possible deviations from predicted trends. Given that the Bellsbank and Bobbejaan kimberlites are diamondiferous, and provided that diamonds are derived from eclogites, then I expect that the eclogites will follow established P-fO_2 trends. The combination of fO_2 determinations with geochemical and petrologic methods will allow for the development of a tectono-magmatic

model of eclogite formation and modification within Archean cratonic lithosphere, with important implications for diamond genesis.

CHAPTER TWO – METHODS

2.1 Sample collection, preparation and petrographic analysis

Twenty-six eclogite xenoliths from the Bellsbank (n = 8) and Bobbejaan (n = 18) kimberlite were prepared for analyses at the University of the Witwatersrand. The eclogite samples (n = 26) were hand-picked from a sorting pile at the processing plant of the DeBruyn and Martin Mine by Prof. Sebastian Tappe, who selected the samples based on their coarse garnet and clinopyroxene mineral assemblage. Additionally, extensively infiltrated and altered samples were avoided.

The eclogite xenoliths have maximum lengths of 3 - 6 cm and were cut length ways using a diamond saw at the University of Witwatersrand to be mounted on thin section glass slides from which “thick” sections (approximately 100 μm thick, suitable for in-situ laser ablation analyses) were prepared. Samples that were too small or irregularly shaped were cut and set in an epoxy to create mounted blocks. All 26 samples were polished and left uncovered for electron microprobe analysis. The remaining material from each sample was double wrapped in plastic bags and crushed using a hammer, then sieved to remove fine particles. Clean and crack free garnet and clinopyroxene was then separated in ethanol filled petri-dishes by hand under a binocular microscope.

A detailed petrographic study to identify mineral phases, modal abundances, textures and any other important petrographic features was performed with an Olympus BX51. Full section scanned images (Figure 2) were taken using an Olympus BX53M/DP74 automated stage microscope and camera set up. A summary description of the samples is given in Table

1 along with representative scanned thin section images in Figure 2 and sample photographs in Appendix Figure 1. The xenoliths are coarse grained (most minerals are > 5mm in diameter) and present as mostly massive and equigranular textures (Figure 2), with a few samples showing foliated textures (DGE-4, DGE-7, DGO-5, DGO-6, DGO-18) (Table 1, Figure 2).

Most Bellsbank and Bobbejaan eclogites have bi-mineralic assemblages in varying proportions of clinopyroxene and garnet (Table 1). Some samples (DGE-3, DGO-1, DGO-3, DGO-11, DGO-8, DGO-13, DGO-16 and DGO-18), however, also contain trace to minor amounts of corundum (< 10 %), kyanite (< 10 %), and rutile (< 5 %) (Table 1, Figure 2). Most eclogite xenoliths contain additional secondary minerals (e.g. phlogopite, sericite and carbonates, Figure 2) associated with small veinlets of kimberlite infiltration. Garnet occurs as deep red to light orange-brown euhedral crystals but also (e.g. sample DGO-4; Figure 2) as small anhedral blebs or exsolution lamellae included within clinopyroxene. Garnet crystals are either fresh with clear cores or are crosscut by an array of small cracks, fractures and veins (Figure 2). In some cases, garnet crystals appear foliated, with thin kelyphite rims (Figure 2). Clinopyroxene is present as medium to dark green crystals that are mostly smaller than surrounding garnet, and in some samples (e.g. DGO-3 and DGO-4; Table 1) clinopyroxene are surrounded by large fine crystalline alteration rims, yielding a ‘spongy’ texture (Figure 2).

2.2 Mineral major and minor element concentrations

The major and minor element compositions of garnet, clinopyroxene, kyanite and corundum from 26 Bellsbank and Bobbejaan eclogites were analysed at Spectrum, located at the University of Johannesburg. A Cameca SX-100 Microprobe with 4 vertically mounted WDS detectors and a BSE detector was used to target three fresh touching garnet and

clinopyroxene mineral pairs per sample (3 spots for each mineral ~ 18 spots per sample). Beam diameter was set to 1 μm at a current of 20 nA and an accelerating voltage of 19.9 KeV. The following elements were analysed on their Kα lines, calibrated to natural mineral reference materials (RM) for the elements; Na (Jadeite), Fe (Hematite), Mg (Olivine), Al (Almandine), Si (Diopside), K (Orthoclase), Ca (Wollastonite), and Mn (Rhodonite). Synthetic crystal reference materials (RM) were used for the elements; Ti (Rutile), Cr (Cr_2O_3), and Ni (NiO). Counting times of 20 seconds was used to obtain quantitative peak intensities for major and minor elements, expressed as weight percent oxides (Table 2, 3). Oxygen content was calculated by stoichiometry, assuming common oxidation states for the cations. Mn and Fe were assumed to be divalent.

2.3 Mineral trace element concentrations

Trace element compositions of garnet (n = 25) and clinopyroxene (n = 26) Bellsbank and Bobbejaan eclogites xenoliths were obtained by in-situ laser ablation quadrupole inductively coupled plasma mass spectrometry of "thick" sections and mineral blocks. The same mineral pairs that were analysed for major and minor element content (EMPA) were targeted here for trace elements (LA-ICPMS). Sample DGE-7 showed visible extreme enrichments in kimberlite infiltration, with no clinopyroxene suitable for analysis. A minimum of three fresh touching pairs of garnet and clinopyroxene (± kyanite, ± corundum where possible) were ablated per sample (~ 18 spots per xenolith). Analyses were performed at the University of the Witwatersrand, with the use of an Australian Scientific Instruments (ASI) Resonetics Resolution 193 nm ArF excimer (SE 155) system coupled to a Thermo Scientific Fisher sector-field ICPMS (Element XR), running in low resolution and electrostatic scanning modes. Data was acquired via single spot analysis (spot size of 30 to 80 μm), using a laser repetition rate of 8 Hz and a fluence of 2.5 Jcm^{-2} .

Table 1. Petrography of the Bellsbank and Bobbejaan eclogite xenoliths

Sample	Type	Grt (%)	Cpx (%)	Crd (%)	Ky (%)	Rt (%)	Trace	Comments
DGE-1	1	45	55	-	-	-	Sulphides, Phlogopite	Massive. Subhedral to rounded coarse garnet (> 4 mm), interstitial to medium clinopyroxene (2 - 3 mm) crystals with large (1 - 2 mm) fine crystalline rims.
DGE-2	2	50	50	-	-	Trace	Sulphides	Massive. Euhedral coarse garnet (> 5 mm) with thin Kelyphite rims. Clinopyroxene (2 - 3 mm) with spongy fine crystalline rim (1 - 2 mm).
DGE-3	2	50	45	-	-	-	Sulphides, Phlogopite	Massive. Euhedral coarse garnet (> 5 mm). Medium clinopyroxene (2 - 3 mm) with spongy fine crystalline rim (1 - 2 mm). Garnet exsolution lamellae and blebs within clinopyroxene. Coarse phlogopite.
DGE-4	2	45	45	-	-	Trace	Sulphides	Foliated. Subhedral coarse garnet (> 5 mm) with cracks and fractures filled with phlogopite and secondary clinopyroxene. Medium to coarse clinopyroxene (2 - 3 mm) with cracked cores and spongy fine crystalline aggregated rims preserving original shape. Phlogopite/Calcite alteration products.
DGE-5	2	60	40	-	-	Trace	Sulphides	Massive. Subhedral coarse garnet (> 5 mm) largely fractured/cracked. Medium coarse clinopyroxene (2 - 4 mm), replaced by phlogopite/calcite and fine crystalline clinopyroxene at rim.
DGE-6	2	50	50	-	-	Trace	Sulphides, Phlogopite	Massive. Euhedral coarse garnet (> 5 mm). Medium clinopyroxene (2 - 3 mm) with fresh cores. Minor white opaque accessory mineral 5% as thin veinlet cross-cutting thin section.
DGE-7	2	80	20	-	-	-	Phlogopite, K-rich infiltration	Foliated. Extensive kimberlite infiltration. Little to no remaining fresh clinopyroxene.
DGE-8	2	50	50	-	-	Trace	Phlogopite, K-rich infiltration	Massive. Euhedral medium to coarse (2 - 3 mm) garnet. Coarse clinopyroxene (> 5 mm) with large spongy rims.
DGO-1	1	40	40	10	10	-	Sulphides	Massive. Granoblastic medium garnet (1 - 2 mm) and clinopyroxene (1 - 2 mm) remnant shape, now pseudomorphs as corundum blebs (1 mm) and kyanite laths (0.5 mm).
DGO-2	2	60	40	-	-	-	Sulphides	Massive. Subhedral coarse garnet (> 5 mm) largely fractured/cracked. Clinopyroxene poorly preserved, being replaced by phlogopite/calcite and other minerals.
DGO-3	2	50	40	5	5		Sulphides	Massive. Subhedral coarse garnet (> 5 mm). Medium clinopyroxene (2 - 3 mm) with spongy fine crystalline rim (1 - 2 mm). Minor sulphides in interstitial glassy to fine phlogopite/carbonate reaction cracks/veinlets. Small (1 mm) Kyanite elongated crystals.
DGO-4	2	60	40	-	-	-	Sulphides	Massive. Euhedral coarse garnet (> 5 mm). Medium clinopyroxene (2 - 3 mm) with spongy fine crystalline rim (1 - 2 mm). Garnet exsolution lamellae and blebs within clinopyroxene. Coarse phlogopite.
DGO-5	2	50	50	-	-	-	Sulphides	Foliated. Subhedral coarse garnet (> 5 mm). Medium to coarse clinopyroxene (2 - 3 mm). Alteration around garnet rims appears as secondary clinopyroxene.
DGO-6	2	60	40	-	-	-	Sulphides, K-rich infiltration	Foliated. Coarse fractured and pitted garnet dominates the sample. Medium to coarse clinopyroxene (2 - 3 mm) with thin (< 1 mm) spongy fine crystalline rim. Phlogopite and K-rich material pervasive throughout.
DGO-7	2	50	45	-	5	-	Sulphides	Massive. Euhedral coarse garnet (>> 5 mm) with medium clinopyroxene (1 - 3 mm).
DGO-8	1	50	45	-	-	Trace	Sulphides, Spinel	Massive. Equigranular anhedral garnet (1 - 3 mm) and euhedral clinopyroxene (1 - 3 mm). Sample is highly fractured with medium to coarse veinlets and fine crystalline secondary phlogopite/calcite. Euhedral hercynitic spinel grain (1 mm).
DGO-9	1	50	50	-	-	-	Sulphides	Massive. Euhedral to subhedral garnet and clinopyroxene with (1 - 2 mm) spongy textured reaction rims.
DGO-10	1	45	40	10	5	-	Sulphides	Massive. Coarse anhedral to rounded garnet (3 - 5 mm) in matrix of mostly altered and infiltrated clinopyroxene. Garnet exsolution lamellae in clinopyroxene. Coarse phlogopite and K-rich infiltration.
DGO-11	2	60	35	-	5	-	Sulphides	Massive. Subhedral coarse garnet (>> 5 mm) with reaction rims and textures. Medium to coarse clinopyroxene (2 - 3 mm) with cracked cores and spongy fine crystalline aggregated rims preserving original shape. Phlogopite/Calcite alteration products.
DGO-12	2	55	45	-	-	Trace	Sulphides, Phlogopite	Massive. Euhedral coarse garnet (> 5 mm). Small specks of clinopyroxene (1 - 2 mm).
DGO-13	2	45	40	5	10	-	Sulphides	Massive. Euhedral coarse garnet (>> 5 mm) with medium clinopyroxene (1 - 3 mm). Interstitial mix of fine crystalline phlogopite and medium to coarse crystalline (1 - 3 mm) corundum and kyanite laths.
DGO-14	2	55	45	-	-	-	Infiltration	Massive. Coarse anhedral to rounded garnet (3 - 5 mm) in matrix of mostly altered and infiltrated clinopyroxene (1 - 2 mm).
DGO-15	2	55	45	-	-	-	Sulphides, K-rich infiltration	Massive. Euhedral coarse garnet (> 5 mm) with medium clinopyroxene (1 - 3 mm). Minor white opaque accessory mineral 5% as thin veinlet cross-cutting thin section.
DGO-16	1	55	45	5	-	-	Phlogopite, K-rich infiltration	Massive. Coarse anhedral to rounded garnet (3 - 5 mm) in matrix of mostly altered and infiltrated clinopyroxene. Garnet exsolution lamellae in clinopyroxene. Coarse phlogopite and K-rich infiltration.
DGO-17	2	55	45	-	-	-	Sulphides, Phlogopite, K-rich infiltration	Massive. Euhedral to subhedral garnet (> 5 mm) and clinopyroxene with (1 - 2 mm) spongy textured fine crystalline rims.
DGO-18	2	55	50	5		Trace	Phlogopite, K-rich infiltration	Foliated. Subhedral coarse garnet (> 5 mm). Medium clinopyroxene (2 - 3 mm) with spongy fine crystalline rims.

Type 1: texturally similar to group I as in Macgregor and Carter (1970); Type 2: texturally similar to group II as in Macgregor and Carter (1970); Grt: garnet; Cpx: clinopyroxene; Crd: corundum; Ky: kyanite; Rt: rutile

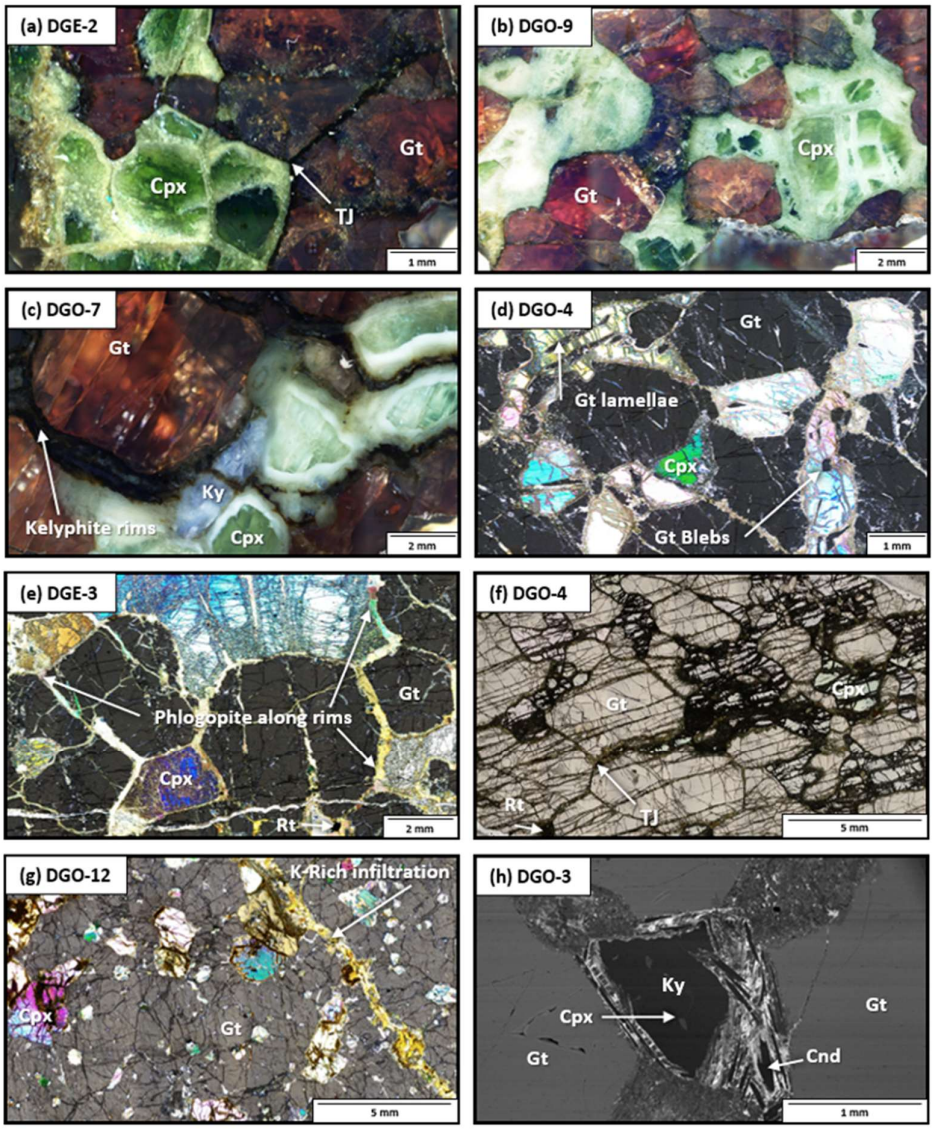

Figure 2. *Images of select Bellsbank and Bobbejaan eclogite xenoliths:* ***(a)*** *Sample DGE-2 showing interlocking triple junctions (TJ) between garnet and clinopyroxene typical for the textural Type II eclogite classification of Mac-Gregor & Carter (1970).* ***(b)*** *Sample DGO-9 showing subhedral garnet in a clinopyroxene matrix, with clinopyroxene having 'spongy' reaction rims of fine crystalline material, typical for the textural Type I eclogite classification of Mac-Gregor & Carter (1970).* ***(c)*** *Sample DGO-7 (Group II) showing subhedral kyanite interstitial to garnet and clinopyroxene. Kelyphite rims surround subhedral garnet crystals. Crossed-polarised light (XPL) photomicrograph of sample DGE-3 having a group II texture, coarse (~ 1 mm) secondary phlogopite around garnet and clinopyroxene grain boundaries.* ***(d)*** *XPL photomicrograph of sample DGO-4 (Group II) showing fresh clinopyroxene and secondary material along grain boundaries. Garnet lamellae and blebs are present within clinopyroxene.* ***(e)*** *Crossed-polarised light (XPL) photomicrograph of sample DGE-3 having a group II texture, coarse (~1 mm) secondary phlogopite around garnet and clinopyroxene grain boundaries, as well as a small (< 0.5 mm) rutile crystal.* ***(f)*** *Plain-polarized light (PPL) photomicrograph of sample DGO-4 (Group II) showing a sheared/foliated texture with parallel pervasive cracks cross-cutting garnet and clinopyroxene while retaining triple-junctions. Small (> 1 mm) rutile.* ***(g)*** *XPL photomicrograph of sample DGO-12 showing massive coarse garnet (> 5 mm) with small (1 - 2 mm) anhedral clinopyroxene. K-rich infiltrated material dominates thin veins.* ***(h)*** *Back Scattered Electron (BSE) image of sample DGO-3 (Group II) showing ~1 mm kyanite crystal interstitial to garnet with small inclusions of clinopyroxene, surrounded corundum needles.*

The surface of each target spot was cleaned by two laser pulses before each analysis. Total signal acquisition time for each analysis was 60 seconds; with 20 seconds of pre- and post-ablation (gas blank) and 20 seconds of ablation measurements.

Laser sampling took place in a SE155 dual-volume ablation cell (Laurin Technic, Canberra, Australia) using a mixed He-Ar and N_2 atmosphere. Gas flow rates were as follows; He (300 - 400 ml/min), Ar (800 - 1200 ml/min) and N_2 (2 - 6 ml/min). Internal calibration of the synthetic glass NIST 612 (Jochum *et al.,* 2011) was used and the NIST 610, NIST 614, BHVO2, and BCR-2 (Jochum *et al.,* 2016) glasses were analyzed as unknowns to evaluate accuracy and precision (Appendix Table 3). NIST 612, NIST 614, BHVO2 and BCR-2 glasses were interspersed between in run to monitor instrumental drift and data quality. The isotope ^{29}Si was used as in internal standard.

The following masses were measured in triple mode; ^{29}Si, ^{43}Ca, ^{45}Sc, ^{47}Ti, ^{51}V, ^{53}Cr, ^{59}Co, ^{60}Ni, ^{65}Cu, ^{85}Rb, ^{88}Sr, ^{89}Y, ^{90}Zr, ^{93}Nb, ^{139}La, ^{140}Ce, ^{141}Pr, ^{146}Nd, ^{147}Sm, ^{151}Eu, ^{157}Gd, ^{159}Tb, ^{163}Dy, ^{165}Ho, ^{166}Er, ^{169}Tm, ^{174}Yb, ^{175}Lu, ^{178}Hf, ^{181}Ta, ^{208}Pb, ^{232}Th, ^{238}U. Data reduction was done with the Iolite software plugin for Wavemetrics' Igor Pro using the data reduction scheme "X_Trace_Elements_IS", and the methods outlined by Paton *et al.* (2010, 2011).

The analysis of external standards (compared to reference values of Jochum et al., 2016) NIST612, BCR2-G and BHVO-G are favourable (Appendix Table 3). Trace element percentage errors for NIST612 (n = 101) are less than 5%, except for Ta which is at 6.4%. The percentage errors of BCR2-G (n = 32) are all below 10% except for Zr, Gd, Tb and Y, which are 10.3%, 10.3%, 11.4% and 11.7% respectively. Standard BHVO-G (n = 33) results are within the same range of percentage errors as BCR2-G.

The element Rb was below the detection limit (DT) in garnet from the Bobbejaan and Bellsbank eclogite xenoliths, except for sample DGO-14

(0.4 ppm). Ta and Pb in garnet were below the detection limit in numerous instances (Appendix Table 6)

For clinopyroxene from the Bobbejaan and Bellsbank eclogite xenoliths, the element Rb was below the detection limit except for samples DGEO-4 (0.02 ppm), DGE-6 (0.14 ppm), DGE-8 (0.08 ppm), DGO-2 (0.07 ppm), DGO-3 (0.07 ppm), DGO-4 (0.04 ppm), DGO-11 (0.02 ppm) and DGO-12 (0.38 ppm) (Appendix Table 5). Trace elements in low abundance (e.g. LREE's in garnet and HREE's in clinopyroxene) have large uncertainties, and trace elements in high abundance (e.g. HREE's in garnet ad LREE's in clinopyroxene) have lower uncertainties (Appendix Table 4 and 5). The sample standard deviation (S.D) was calculated for each trace-element analysis, and relative percentage difference was used to estimate where contamination might be present (Appendix Table 5).

2.4 Garnet oxygen isotope compositions

The oxygen isotopic compositions reported as $\delta^{18}O$ values in Table 3, were measured from individual clean (alteration, crack and inclusion-free) garnet separates for 24 Bellsbank and Bobbejaan eclogite xenoliths. Garnet crystals weighing between 1 - 2 mg were placed into a reaction vessel containing a nickel plate sample holder, filled with 10 kPa BrF_5 reagent and were then ablated with a NuWave laser. Oxygen as $\delta^{17}O$ and $\delta^{18}O$ was then absorbed onto a 5 Angstrom molecular sieve and analysed using a Finnigan Delta XP dual-inlet gas source multi-collector ICM-MS at the University of Cape Town, following the laser fluorination methods of Harris and Vogeli, (2010). The weight of each sample was inferred from the inlet gas pressure and was all within analytical limits. Data was calibrated to the known Monastry Garnet standard (MON-GT) and normalized relative to Standard Mean Oceanic Water (SMOW). The average $\delta^{18}O$ value for MON-GT obtained over three separate runs was +5.83 ‰ (2σ = +0.22 ‰; n = 6) which represents an 8.32 % error from the accepted reference value of

+5.38 ‰ (Harris and Vogeli, 2010). The long-term laboratory reproducibility of MON-GT is 0.115 ‰ (1SD = 0.077 ‰) (C. Harris, Pers. Comm. 2019). The maximum uncertainty for the $\delta^{18}O$ values of garnet from the Bellsbank and Bobbejaan eclogite xenoliths is therefore ±0.12 ‰.

2.5 Garnet Fe^{3+} measurement

$Fe^{3+}/\Sigma Fe$ content in ultra-pure garnet separates of the Bellsbank and Bobbejaan eclogites (n = 24) were measured by Mössbauer spectroscopy at the Gothe-Universität (Frankfurt am Main, Germany). Powdered samples (~ 2 - 4 mg) at room temperature (293K) were placed into a Pb sample stage and subject to a ~50mCi ^{57}Co in Rh source at a velocity ramp of ~5 mm/s. In order to minimise saturation effects, the diameter of each samples was adjusted in order to maintain an absorber thickness of <5 mg Fe/cm^2. The α-Fe metal foil calibrated garnet mirror image spectra were collected over 512 channels, followed by fitting and correction for recoil-free fraction effects (Woodland and Koch, 2003). Absolute uncertainties of ± 0.01 are shown in Table 5.

CHAPTER THREE – RESULTS

3.1 Major and minor element mineral compositions

Major and minor element chemistry of the eclogite minerals are listed in Table 2, Table 3 and Appendix Tables 1, 2, 4 and 5. Corrected garnet Fe^{3+} contents are reported (with absolute uncertainties of ± 0.01) as $Fe^{3+}/\Sigma Fe$ (Table 3) and range from 0.009 to 0.039. All Fe content is therefore reported as FeO total for clinopyroxene, garnet and whole-rock (Tables 2, 3 and 4 respectively)

Bellsbank and Bobbejaan eclogite garnet have MgO contents between 6.2 and 17.8 wt.%, and Cr_2O_3 contents less than 0.2 wt.%. Garnet have variable FeO (8.5 - 18.3 wt.%) and CaO (3.8 - 23 wt.%) contents, with Mg-

numbers (atomic Mg/(Mg+Fe)*100) from 47 to 70, and Ca-numbers (atomic Ca/(Ca+Mg+Fe+Mn)*100) from 10 to 60. Using the Mg-Fe-Ca garnet compositional classification scheme of Coleman *et al.* (1965), most Bellsbank and Bobbejaan samples plot as group B (Figure 3; Table 3), with several samples plotting in the groups A (samples DGE-1, DGE-3, and DGO-8) and C (sample DGO-1) fields. Kaapvaal eclogite data are given in the caption to Figure 3.

Samples that contain minor amounts of kyanite (5 - 10% modal abundance) contain garnet with on average higher CaO contents (13.1 wt.%) compared to those eclogites where kyanite is absent (average 11.3 wt.%). Garnet from the eclogite xenoliths of this study compares to previous studies on the Bellsbank and Bobbejaan eclogite xenoliths (Shervais *et al.,* 1988; Caporuscio and Smyth, 1990; Neal *et al.,* 1990; Shu *et al.,* 2016), which have similar MgO (8.6 - 21.7 wt.%), FeO (7.5 - 19.6 wt.%) and CaO (3.6 - 18.3 wt.%) contents. Kyanite-bearing samples from previous studies also have higher CaO contents in garnet compared to kyanite free samples (14.9 vs. 5.4 wt.%). While garnet Al_2O_3 content does not vary considerably between samples, Group A garnet has higher MgO (15.3 – 17.8 wt.%) than Group B garnet (9.0 – 13.3 wt.%) but lower CaO (3.9 – 5.1 wt.% vs. 9.0 – 16.0 wt.%)

Clinopyroxene from the Bellsbank and Bobbejaan eclogites have variable Na_2O (3.6 - 8.7 wt.%), CaO (10.5 - 17.9 wt.%), MgO (5.7 - 14.2 wt.%), FeO (1 - 5 wt.%) and Al_2O_3 (4.8 – 18 wt.%) contents. The clinopyroxene Mg# ranges from 66 to 92, and jadeite components (molar [Na - Cr - (2*Ti)]) from 0.22 to 0.59. Using the MgO – Na_2O classification scheme of Taylor and Neal, (1989), the clinopyroxenes plot into groups B and C, and in general follow the trend observed for Kaapvaal eclogites (Figure 4).

Clinopyroxene from the eclogite xenoliths of this study compares well to previous studies (Shervais *et al.,* 1988; Caporuscio and Smyth, 1990; Neal *et al.,* 1990; Shu *et al.,* 2016) on the Bellsbank and Bobbejaan eclogite xenoliths, which show similar Na_2O (1.4 - 9.7 wt.%), CaO (9.5 - 22.3 wt.%),

Table 2. Major and trace element compositions of clinopyroxene for Bellsbank and Bobbejaaan eclogite xenoliths

Sample	DGE-1	DGE-2	DGE-3	DGE-4	DGE-5	DGE-6	DGE-8	DGO-1	DGO-2	DGO-3	DGO-4	DGO-5	DGO-6	DGO-7	DGO-8	DGO-9	DGO-10	DGO-11	DGO-12	DGO-13	DGO-14	DGO-15	DGO-16	DGO-17	DGO-18
Class	B	B	B	B	C	B	B	C	C	C	C	B	B	B	B	B	C	B	B	C	C	C	C	C	B
SiO_2	55.1	54.9	54.9	54.6	55.0	54.5	54.9	54.3	55.7	54.8	54.5	55.0	53.8	54.3	53.6	55.6	56.8	54.8	54.4	55.0	54.4	55.9	55.6	56.0	54.6
TiO_2	0.4	0.2	0.4	0.2	0.2	0.2	0.2	0.1	0.2	0.1	0.2	0.3	0.2	0.2	0.3	0.1	0.1	0.2	0.1	0.1	0.3	0.2	0.2	0.1	0.2
Al_2O_3	4.8	8.4	4.8	8.1	13.8	6.3	9.2	18.0	14.8	16.1	17.3	10.3	10.2	7.8	5.8	10.8	16.5	11.0	8.5	16.3	12.7	15.7	13.7	16.3	8.9
Cr_2O_3	0.08	0.14	0.09	0.05	0.06	0.30	0.05	0.01	0.02	0.03	0.07	0.12	0.03	0.03	0.22	0.06	0.02	0.12	0.01	0.02	0.10	0.09	0.23	0.02	0.04
FeO	5.0	3.5	5.0	3.3	2.6	4.0	3.8	1.2	1.6	1.0	1.1	2.4	2.7	3.1	4.6	3.0	1.2	2.2	3.7	1.2	1.9	1.6	1.7	1.2	3.0
MnO	0.12	0.03	0.13	0.03	0.02	0.03	0.04	0.00	0.02	0.00	0.01	0.02	0.02	0.03	0.04	0.02	0.01	0.01	0.03	0.01	0.01	0.01	0.01	0.01	0.03
MgO	14.2	10.9	14.0	11.3	7.7	12.2	10.1	5.7	7.8	6.9	6.1	10.2	10.1	11.6	12.4	9.5	6.5	9.9	10.7	6.7	8.6	6.8	8.2	6.6	10.8
CaO	16.6	16.4	16.7	17.1	12.5	17.9	16.0	10.5	12.5	11.3	10.7	15.6	15.3	16.9	17.4	15.0	10.8	15.1	16.5	10.9	13.4	11.5	13.0	10.9	16.2
Na_2O	3.6	5.2	3.6	4.9	7.6	4.3	5.3	8.7	7.6	8.4	8.7	5.7	6.0	4.7	4.2	6.1	8.3	6.1	5.1	8.6	7.1	8.1	7.4	8.6	5.3
K_2O	0.03	0.00	0.03	0.01	0.02	0.01	0.03	0.13	0.01	0.01	0.01	0.01	0.01	0.01	0.01	0.01	0.01	0.01	0.01	0.01	0.01	0.00	0.01	0.01	0.01
NiO	0.04	0.07	0.03	0.08	0.07	0.11	0.03	0.05	0.18	0.17	0.15	0.15	0.08	0.14	0.08	0.08	0.20	0.15	0.06	0.21	0.18	0.09	0.11	0.20	0.10
Total	100.0	99.6	99.7	99.6	99.5	99.8	99.6	98.6	100.4	99.0	99.0	99.9	98.4	98.9	98.8	100.1	100.5	99.5	99.2	99.0	98.7	100.1	100.1	99.9	99.2
Mg#	83	85	83	86	84	84	66	89	89	92	91	88	87	87	83	85	91	89	84	91	89	88	90	91	86
xJd	0.22	0.35	0.22	0.33	0.51	0.28	0.35	0.59	0.50	0.57	0.58	0.37	0.41	0.32	0.28	0.41	0.55	0.41	0.35	0.58	0.48	0.54	0.49	0.57	0.36
V	506	724	468	919	718	879	749	-	199	227	703	885	594	563	542	1032	170	319	1047	164	919	647	662	288	631
Ni	422	683	403	985	790	1256	374	-	1586	1847	1569	1619	1106	1429	876	780	2241	1567	668	2096	1844	927	1294	3395	1134
Sc	36	27	36	32	14	11	38	-	6.2	2.1	6	13	10	14	21	24	1.6	12	43	1.8	9	5	5	3	13
Rb	0	0	0	0.02	0	0.14	0.08	-	0.07	0.07	0.04	0	0	0	0	0	0	0.02	0.38	0	0.02	0	0	0	0
Th	0.06	0.17	0.06	0.19	0.02	0.28	0.07	-	0.06	0.05	0.07	0.16	0.18	0.19	0.32	0.08	0.04	0.04	0.23	0.04	0.10	0.06	0.05	0.06	0.19
U	0.02	0.01	0.02	0.02	0.01	0.03	0.03	-	0.03	0.00	0.00	0.01	0.01	0.01	0.02	0.01	0.00	0.01	0.02	0.00	0.01	0.00	0.00	0.01	0.01
Nb	0.99	0.22	1.04	0.32	0.42	0.92	0.17	-	0.21	0.02	0.10	0.99	0.35	0.00	0.01	0.21	0.04	0.19	0.60	0.03	0.01	0.92	0.33	0.04	0.47
Ta	0.149	0.013	0.167	0	0.020	0.030	0.008	-	0.011	0.001	0.004	0.037	0.023	0	0	0.007	0.007	0.003	0.030	0.004	0.001	0.023	0.011	0.012	0.027
La	3.2	1.5	3.5	1.6	0.5	2.8	1.5	-	0.4	0.3	0.5	1.8	1.6	1.4	3.5	0.8	0.5	1.3	3.8	0.5	1.5	0.5	0.7	0.8	1.9
Ce	11.8	4.0	12.6	2.8	1.6	10.6	5.4	-	1.0	0.5	0.8	3.7	3.0	2.1	7.9	1.3	1.2	2.7	10.1	1.3	2.7	1.3	1.0	1.9	2.9
Pr	1.92	0.41	2.15	0.23	0.25	1.51	0.66	-	0.12	0.05	0.06	0.36	0.24	0.25	0.89	0.11	0.15	0.28	1.23	0.17	0.22	0.12	0.09	0.24	0.19
Pb	0.26	0.57	0.30	0.14	0.03	0.42	0.07	-	0.07	0.02	0.06	0.11	0.17	0.31	0.39	0.09	0.04	0.27	1.08	0.03	0.18	0.01	0.02	0.07	0.20
Sr	192	37	188	39	57	82	92	-	28	16	9	48	23	77	66	20	34	44	117	36	32	25	25	54	26
Nd	10.3	1.01	10.4	0.60	1.27	5.98	2.39	-	0.65	0.22	0.18	0.98	0.70	1.17	3.10	0.36	0.47	0.73	4.49	0.42	0.71	0.36	0.27	0.67	0.44
Sm	2.52	0.21	2.58	0.18	0.29	0.90	0.56	-	0.39	0.04	0.06	0.27	0.22	0.46	0.88	0.08	0.04	0.16	0.66	0.04	0.22	0.09	0.06	0.06	0.22
Zr	40.8	3.3	41.7	3.8	5.3	12.3	12.9	-	10.6	1.0	0.7	8.0	6.2	11.9	12.3	1.7	1.1	3.9	5.3	1.2	6.5	0.9	1.4	1.6	6.4
Hf	1.60	0.32	1.71	0.34	0.39	0.83	0.61	-	0.50	0.11	0.10	0.54	0.50	0.65	0.78	0.21	0.14	0.32	0.34	0.12	0.65	0.12	0.20	0.19	0.46
Eu	0.75	0.09	0.78	0.11	0.09	0.37	0.18	-	0.31	0.00	0.02	0.15	0.13	0.33	0.41	0.03	0.00	0.09	0.18	0.03	0.10	0.02	0.05	0.04	0.14
Ti	3929	1566	3794	1372	2194	1847	1927	-	1830	1257	1996	2616	1709	1864	2580	917	1094	1716	1225	1125	2280	1529	1683	1833	1653
Gd	2.17	0.46	2.17	0.48	0.21	0.62	0.58	-	0.46	0	0.08	0.29	0.26	0.56	1.56	0.21	0.00	0.09	0.52	0.01	0.22	0.10	0.05	0.01	0.37
Tb	0.293	0.074	0.327	0.083	0.029	0.079	0.086	-	0.084	0.001	0.011	0.040	0.051	0.063	0.213	0.036	0.003	0.018	0.081	0.001	0.037	0.007	0.008	0.003	0.049
Dy	1.57	0.45	1.58	0.45	0.11	0.34	0.45	-	0.47	0.01	0.04	0.21	0.20	0.36	1.11	0.24	0.02	0.10	0.45	0.01	0.20	0.03	0.05	0.01	0.26
Y	6.39	1.74	6.85	1.85	0.50	1.07	1.65	-	2.53	0.04	0.19	0.66	0.62	1.08	3.69	1.06	0.01	0.28	1.89	0.03	0.72	0.13	0.13	0.05	0.74
Ho	0.278	0.077	0.298	0.089	0.029	0.045	0.072	-	0.097	0.001	0.008	0.030	0.032	0.048	0.163	0.044	0.001	0.007	0.082	0.002	0.030	0.004	0.006	0.001	0.033
Er	0.641	0.171	0.654	0.186	0.043	0.097	0.157	-	0.260	0	0.009	0.089	0.067	0.101	0.298	0.091	0.002	0.022	0.172	0.005	0.074	0.007	0.016	0	0.070
Tm	0.074	0.020	0.083	0.020	0.004	0.006	0.019	-	0.034	0	0.004	0.009	0.008	0.013	0.034	0.012	0	0.003	0.019	0	0.007	0	0.001	0	0.006
Yb	0.39	0.11	0.36	0.13	0.01	0.03	0.10	-	0.28	0	0.01	0.06	0.01	0.05	0.16	0.05	0	0.00	0.09	0.00	0.04	0.00	0.00	0.01	0.04
Lu	0.049	0.016	0.049	0.015	0.005	0.001	0.007	-	0.047	0.002	0.001	0.015	0.002	0.005	0.013	0.007	0	0	0.010	0.001	0.003	0.000	0.000	0	0.005
Eu*	1.0	0.9	1.0	1.1	1.1	1.4	1.0	-	2.2	0.4	0.8	1.7	1.6	2.0	1.1	0.7	0.0	2.1	0.9	3.6	1.4	0.6	2.6	3.6	1.5
Sr*	1.3	1.6	1.2	2.9	2.9	0.8	2.1	-	3.0	4.6	2.6	2.2	1.6	4.1	1.1	2.8	3.6	2.7	1.4	3.7	2.3	3.4	4.5	3.8	2.5
La/Sm	0.82	4.53	0.87	5.87	1.05	2.02	1.79	-	0.74	4.85	4.60	4.40	4.81	1.94	2.55	5.74	9.33	5.13	3.70	9.51	4.40	3.71	7.32	8.79	5.51
∑HREE	3.29	0.91	3.36	0.98	0.24	0.60	0.89	-	1.27	0.01	0.09	0.45	0.37	0.63	1.99	0.48	0.02	0.15	0.91	0.02	0.39	0.05	0.08	0.02	0.46

*Major elements in wt.% of oxides ; Trace elements in ppm ; Mg# calculated as molar((Mg/(Mg+Fe))*100; xJd (jadeite proportion) calculated as molar Na – Cr – [2*Ti]; "-": below detection limit; "*": no value; 2σ standard errors are reported in Appendix table 4; Eu*: Eu/(0.5*Gd + 0.5*Sm), primitive mantle normalized (McDonough and Sun, 1995); Sr*: Sr/(0.5*Pr + 0.5*Nd), primitive mantle normalized (McDonough, Sun, 1995); La/Sm: La/Sm ratio, primitive mantle normalized (McDonough, Sun, 1995); Classification: clinopyroxene major element classification of Taylor and Neal (1989); ∑HREE: Tb+Ho+Er+Tm+Yb+Lu. Fe content is reported as FeO total. Major (EPMA) and trace (LA-ICPMS) contents represent an average of three analyses on three touching mineral pairs for each sample.*

Table 3. Major and trace element compositions of garnet for Bellsbank and Bobbejaaan eclogite xenoliths

Sample	DGE-1	DGE-2	DGE-3	DGE-4	DGE-5	DGE-6	DGE-8	DGO-1	DGO-2	DGO-3	DGO-4	DGO-5	DGO-6	DGO-7	DGO-8	DGO-9	DGO-10	DGO-11	DGO-12	DGO-13	DGO-14	DGO-15	DGO-16	DGO-17	DGO-18
Class	A	B	A	B	B	B	B	C	B	B	B	B	B	B	A	B	B	B	B	B	B	B	B	B	B
SiO_2	41.6	40.5	41.6	39.8	39.6	40.0	39.4	39.4	41.1	40.1	39.6	40.6	39.2	40.0	39.7	40.5	41.6	40.4	39.9	40.3	39.5	40.8	40.2	40.9	39.9
TiO_2	0.36	0.14	0.36	0.12	0.17	0.17	0.15	0.14	0.15	0.11	0.17	0.16	0.12	0.16	0.14	0.08	0.08	0.12	0.17	0.09	0.14	0.13	0.14	0.09	0.17
Al_2O_3	22.8	22.8	22.9	22.4	22.4	22.6	22.0	22.4	23.1	23.0	22.7	22.7	22.5	22.6	22.7	22.5	23.3	22.9	22.6	23.0	22.6	22.9	22.6	23.0	22.6
Cr_2O_3	0.08	0.06	0.09	0.05	0.05	0.08	0.04	0.02	0.01	0.02	0.06	0.09	0.02	0.08	0.19	0.06	0.01	0.10	0.08	0.02	0.08	0.07	0.18	0.02	0.08
FeO	13.7	12.4	13.8	15.6	13.7	13.5	18.3	8.5	11.7	9.7	10.6	13.1	14.3	13.2	15.9	13.7	10.0	12.1	13.6	10.0	12.5	10.8	12.3	10.0	13.6
MnO	0.5	0.3	0.5	0.4	0.3	0.3	0.4	0.2	0.2	0.2	0.2	0.2	0.3	0.3	0.4	0.4	0.2	0.2	0.3	0.2	0.2	0.2	0.2	0.2	0.3
MgO	17.8	11.9	17.4	11.3	9.0	12.2	9.0	6.2	12.3	12.7	10.2	12.4	13.3	12.3	15.3	10.1	12.3	13.0	12.4	12.6	12.5	10.3	11.1	12.4	12.4
CaO	3.9	12.2	3.9	10.5	14.7	10.9	10.7	23.0	12.5	13.9	16.0	10.8	9.0	11.1	5.1	13.2	13.4	11.2	10.6	13.5	11.2	15.3	13.5	13.7	10.6
Na_2O	0.10	0.05	0.09	0.05	0.07	0.05	0.05	0.04	0.06	0.04	0.06	0.06	0.04	0.05	0.04	0.03	0.04	0.05	0.05	0.04	0.05	0.05	0.06	0.04	0.05
K_2O	0.01	0.00	0.01	0.01	0.00	0.01	0.01	0.00	0.01	0.01	0.00	0.00	0.01	0.01	0.01	0.00	0.00	0.00	0.01	0.00	0.00	0.00	0.00	0.00	0.01
NiO	0.01	0.01	0	0.02	0.01	0.01	0.00	0.01	0.02	0.02	0.01	0.01	0.02	0.01	0.01	0.01	0.03	0.01	0.01	0.03	0.02	0.01	0.02	0.02	0.01
Total	100.7	100.2	100.7	100.2	100.0	99.8	100.1	99.8	101.0	99.7	99.6	100.2	98.9	99.7	99.4	100.5	100.9	100.0	99.7	99.7	98.8	100.6	100.3	100.3	99.7
Mg#	70	63	69	56	54	62	47	56	65	70	63	63	62	62	63	57	69	66	62	69	64	63	62	69	62
Ca#	10	32	10	27	39	28	28	60	32	35	41	28	23	29	13	34	35	29	27	35	29	40	35	35	27
$Fe^{3+}/\sum Fe$	0.036	0.028	0.039	0.020	0.025	0.026	0.018	0.024	0.011	0.014	0.009	0.012	0.014	0.014	0.034	0.026	-	0.012	0.028	0.012	0.014	0.014	0.014	0.016	0.020
$\delta^{18}O$ (‰)	6.03	-	6.25	3.13	4.41	3.75	3.65	3.64	4.43	4.48	3.95	4.28	4.61	4.02	3.43	3.03	4.11	4.31	3.36	4.41	5.25	4.24	2.74	4.15	4.48
V	180	264	175	329	271	329	249	374	66	63	301	232	138	182	125	355	43	84	294	45	262	195	181	40	177
Ni	53	63	51	67	77	124	25	57	240	236	239	130	88	184	76	62	300	144	47	293	121	98	124	227	112
Sc	92	136	90	113	77	50	118	46	15	22	79	53	48	80	58	129	17	66	155	18	42	51	34	16	71
Rb	0	0	0	0	0	0	0	0	0	0	0	0	0	0	0	0	0	0	0	0	0.40	0	0	0	0
Th	0.001	0.031	0.000	0.021	0.018	0.022	0.014	0.066	0.039	0.033	0.098	0.042	0.025	0.008	0.006	0.045	0.051	0.022	0.057	0.028	0.017	0.041	0.042	0.028	0.028
U	0.011	0.035	0.013	0.038	0.052	0.050	0.049	0.024	0.049	0.017	0.020	0.037	0.027	0.014	0.016	0.026	0.057	0.038	0.060	0.064	0.021	0.020	0.021	0.040	0.029
Nb	0.217	0.099	0.197	0.074	0.289	0.298	0.069	0.148	0.002	0.021	0.071	0.278	0.132	0	0.002	0.130	0.030	0.075	0.205	0.020	0.000	0.519	0.214	0.018	0.179
Ta	0.024	0.019	0.018	0	0.003	0	0	0	0.001	0	0	0.015	0.002	0	0	0.001	0.001	0.002	0	0.002	0.248	0	0	0.001	0.002
La	0.002	0.038	0.014	0.020	0.044	0.006	0.029	0.137	0.041	0.028	0.081	0.049	0.025	0	0.002	0.044	0.066	0.044	0.069	0.066	0.013	0.061	0.055	0.045	0.038
Ce	0.13	0.29	0.13	0.15	0.51	0.34	0.40	0.44	0.24	0.17	0.41	0.31	0.26	0.08	0.08	0.26	0.53	0.27	0.63	0.53	0.21	0.40	0.25	0.39	0.20
Pr	0.05	0.08	0.05	0.03	0.20	0.15	0.14	0.06	0.06	0.04	0.06	0.08	0.08	0.03	0.03	0.06	0.15	0.08	0.20	0.15	0.07	0.09	0.05	0.12	0.03
Pb	0	0.0	0.01	0.01	0.01	0	0	0	0.04	0	0.00	0.04	0.01	0.01	0.06	0.00	0.01	0.00	0.01	0.01	0.41	0.00	0.16	0.00	0.02
Sr	0.24	0.14	0.14	0.00	0.54	0.16	0.33	0.37	0.06	0.16	0.08	0.27	0.00	0.04	0.00	0.13	0.40	0.12	0.29	0.39	0.48	0.24	0.20	0.30	0.11
Nd	0.6	0.4	0.7	0.2	2.0	1.5	1.2	0.2	0.6	0.4	0.4	0.5	0.5	0.3	0.3	0.4	0.9	0.5	1.8	1.0	0.3	0.6	0.4	0.7	0.2
Sm	0.7	0.4	0.7	0.4	1.7	1.1	1.2	0.2	0.8	0.4	0.6	0.5	0.4	0.5	0.3	0.3	0.4	0.4	1.4	0.4	1.7	0.6	0.3	0.4	0.4
Zr	29	3.9	28	3.3	12	13	7.3	0.3	17	5.1	5.5	8.1	6.6	11.1	4.8	2.7	6.1	5.5	4.5	6.1	5	4.1	3.6	4.5	6.7
Hf	0.37	0.11	0.34	0.09	0.26	0.23	0.11	0.03	0.35	0.12	0.26	0.18	0.14	0.19	0.10	0.07	0.15	0.11	0.06	0.15	0.71	0.13	0.12	0.11	0.15
Eu	0.4	0.4	0.4	0.4	0.9	0.9	0.7	0.1	0.6	0.4	0.5	0.6	0.4	0.7	0.4	0.3	0.4	0.4	0.9	0.4	0.3	0.5	0.4	0.3	0.5
Ti	3530	1336	3250	1072	1544	1628	1394	1167	1268	829	1510	1265	957	1559	1346	780	710	1032	956	778	1234	1102	1156	646	1197
Gd	1.8	3.1	1.8	2.6	3.7	2.6	3.9	0.7	1.2	0.7	2.2	1.8	1.8	2.2	2.2	2.4	0.7	1.1	3.7	0.7	1.3	1.3	1.4	0.6	2.1
Tb	0.44	1.04	0.47	0.90	0.85	0.61	1.06	0.15	0.22	0.14	0.63	0.47	0.49	0.60	0.71	0.90	0.13	0.29	1.10	0.14	0.56	0.29	0.29	0.11	0.58
Dy	4.4	12	4.6	9.1	6.9	5.4	10	1.2	1.4	1.1	6.1	3.9	4.2	5.6	7.0	11	0.9	2.3	12	1.0	5.1	2.4	2.1	0.8	5.2
Y	33.0	95.7	34.1	73.6	43.5	33.8	68.9	7.0	7.4	5.7	43.0	27.6	26.8	39.8	47.7	87.3	5.3	15.6	89.6	5.7	36.2	15.8	11.0	4.5	33.7
Ho	1.27	3.56	1.39	2.80	1.75	1.25	2.62	0.26	0.30	0.23	1.71	1.1	1.06	1.53	1.78	3.2	0.21	0.64	3.4	0.24	1.41	0.58	0.43	0.17	1.29
Er	4.7	13.0	4.7	9.8	5.5	3.8	8.8	0.9	0.8	0.6	5.6	3.5	3.5	5.2	5.7	11.8	0.6	2.1	11.7	0.7	4.4	1.8	1.2	0.5	4.3
Tm	0.86	2.16	0.88	1.75	0.89	0.59	1.43	0.15	0.13	0.12	0.99	0.60	0.57	0.87	0.88	2.03	0.11	0.37	1.83	0.11	0.89	0.28	0.16	0.09	0.68
Yb	6.1	16.5	6.2	12.6	6.0	4.5	10.3	0.9	0.9	0.7	7.1	4.1	3.7	6.3	6.2	15.4	0.7	2.5	12.3	0.8	5.1	1.9	1.1	0.6	5.1
Lu	0.96	2.51	1.01	2.17	0.94	0.69	1.55	0.14	0.12	0.12	1.13	0.68	0.59	1.02	0.88	2.42	0.10	0.41	1.94	0.12	0.83	0.29	0.17	0.09	0.82
Eu*	0.9	0.7	1.0	0.9	1.1	1.5	0.9	1.0	2.0	2.5	1.2	1.7	1.3	1.8	0.9	0.8	2.3	2.0	1.1	2.5	0.5	1.7	1.4	2.3	1.3
Lu/Gd	4.4	6.6	4.5	6.6	2.1	2.1	3.2	1.7	0.8	1.4	4.1	3.0	2.7	3.7	3.2	8.2	1.1	3.1	4.3	1.4	5.3	1.8	1.0	1.3	3.2
∑HREE	18.7	50.8	19.2	39.1	22.9	16.8	36.0	3.6	3.9	3.0	23.2	14.4	14.2	21.0	23.1	46.3	2.8	8.6	43.8	3.1	18.3	7.6	5.4	2.3	17.9

Major elements in wt.% oxides; Trace elements in ppm; "-": below detection limit; "": no value; 2σ standard errors reported in Appendix table 5; $Fe^{3+}/\sum Fe$: results from Mössbauer spectroscopy; Mg#: molar $Mg/(Mg + Fe_{TOTAL})*100$; $\delta^{18}O$: oxygen isotopic composition (values are all + $\delta^{18}O$) per-mill (‰) normalized relative to Standard Mean Ocean Water (SMOW); Ca#: molar $Ca/(Ca+Mn+Fe+Mg)*100$; Eu*: $Eu/(0.5*Gd + 0.5*Sm)$, primitive mantle normalized (McDonough and Sun, 1995); Lu/Gd: calculated , primitive mantle normalized (McDonough and Sun, 1995); Classification: garnet major element classification of Taylor and Neal (1989); ∑HREE: Tb+Ho+Er+Tm+Yb+Lu. Fe content is reported as FeO total. Major (EPMA) and trace (LA-ICPMS) contents represent an average of three analyses on three touching mineral pairs for each sample.*

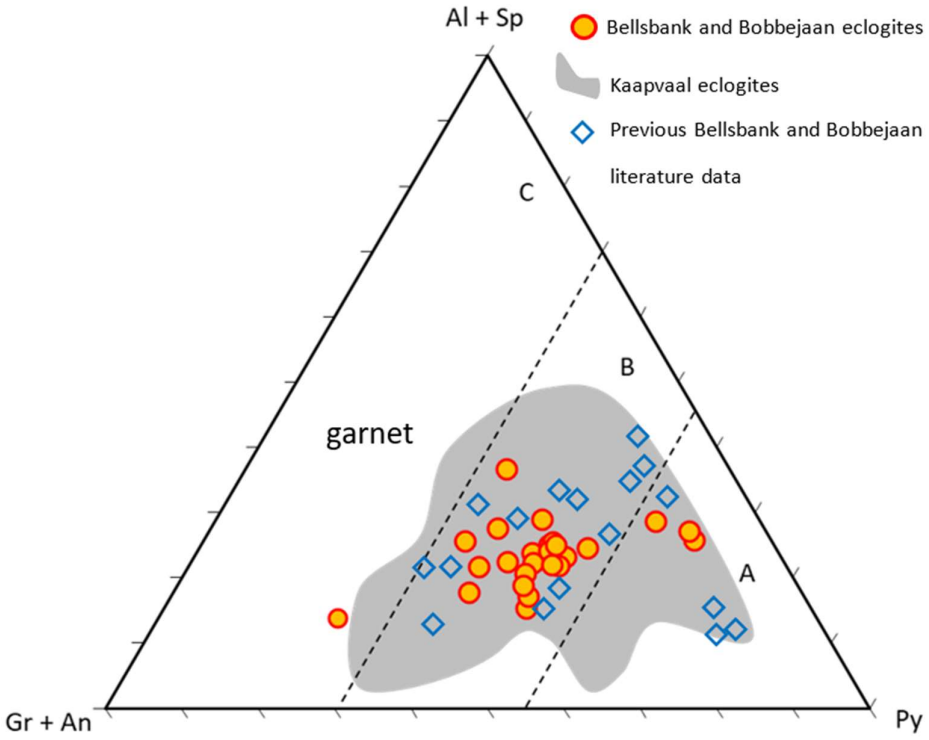

Figure 3. *Ternary plot of garnet major element compositions after the A-B-C classification of Coleman et al. (1965). Al: almandine; Sp: spessartine; Gr: grossular; An: andradite; Py: pyrope. Tick marks shown represent 10% intervals. Previous Bellsbank and Bobbejaan eclogite data from (Caporuscio, 1990; Shervais et al., 1988; Taylor, Neal, 1989; Neal et al., 1990; Shu et al., 2016). Kaapvaal eclogite literature data from (MacGregor and Manton, 1986; Ongley et al., 1987; Caporuscio and Smyth, 1990; Appleyard et al., 2004; Viljoen et al., 2005; Jacob et al., 2009; Gréau et al., 2011; Aulbach and Viljoen, 2015; Riches et al., 2016b; Shu et al., 2016; Aulbach et al., 2016; Huang et al., 2016; Aulbach et al., 2017).*

MgO (5.8 - 16.2 wt.%), FeO (0.9 - 8 wt.%) and Al_2O_3 (2.3 - 17.1 wt.%) contents.

Samples from this study that contain kyanite have clinopyroxene CaO contents which are on average lower than those not containing kyanite (12.9 vs. 14.7 wt.%), which is consistent with findings from previous studies on Bellsbank and Bobbejaan eclogites (11.5 vs. 17.4 wt.%). Group B clinopyroxene have lower Al_2O_3 contents (4.8 – 11 wt.%) than Group C clinopyroxene (12.7 – 18 wt.%), and higher MgO contents (9.5 – 14.2 wt.% vs. 5.7 – 8.6 wt.%).

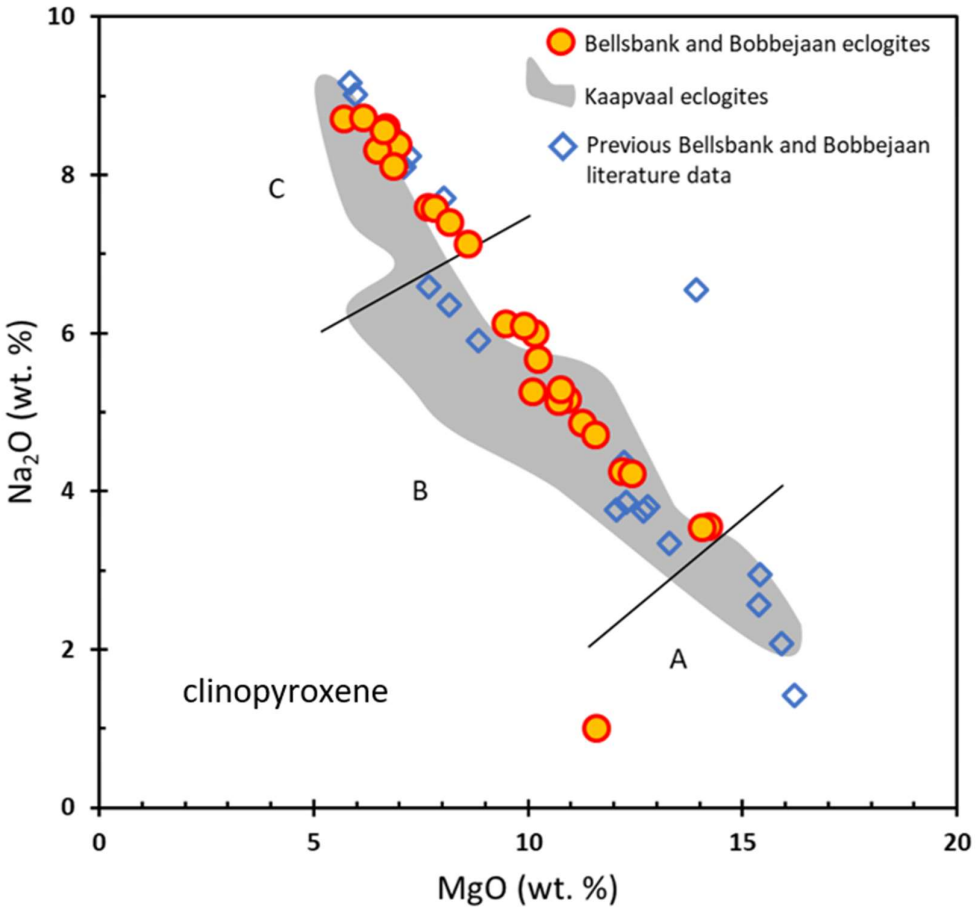

Figure 4. *Clinopyroxene MgO-Na_2O content of the Bellsbank and Bobbejaan eclogites. Shown for comparison are clinopyroxene MgO-Na_2O contents from other Kaapvaal eclogites. A-B-C classification scheme after Taylor and Neal (1989). Previous Bellsbank and Bobbejaan eclogite plotted in blue diamonds (Caporuscio, 1990; Shervais et al., 1988; Taylor, Neal, 1989; Neal et al., 1990; Shu et al., 2016). Kaapvaal eclogite literature data from (Appleyard et al., 2004; Aulbach et al. , 2017b, 2016; Aulbach and Viljoen, 2015; Caporuscio and Smyth, 1990; Gréau et al., 2011, 2011; Huang et al., 2016; Jacob et al., 2009; MacGregor and Manton, 1986; Ongley et al., 1987; Riches et al., 2016b; Shu et al., 2016; Viljoen et al., 2005).*

The garnet A-B-C (Coleman *et al.,* 1965) and clinopyroxene A-B-C (Neal *et al.,* 1990) classification schemes discussed above do not coincide. Eclogite samples DGE-1, DGE-3, and DGO-8, plot within Group A based on garnet compositions, but the clinopyroxene compositions plot within Group B and C. Eclogite samples DGE-5, DGO-2, DGO-3, DGO-4, DGO-8, DGO-10, DGO-13, DGO-14, DGO-15, DGO-15, DGO-16 and DGO-17 plot within group B based on garnet compositions, however plot as Group C based on clinopyroxene composition. For the duration of the manuscript, the garnet

based major element classification of Coleman *et al*., (1965) will be employed.

3.2 Trace element mineral compositions

Trace element data were obtained for garnet and clinopyroxene from the Bellsbank and Bobbejaan eclogites and are listed in Tables 2 and 3.

Primitive mantle normalized (McDonough and Sun, 1995) rare earth element (REE) patterns for garnet (Figure 5) reveal flat (Lu/Gd ~ 1) and fractionated (Lu/Gd ~ 8.2) heavy rare earth element (HREE) patterns with a wide range of HREE (Tb + Dy + Ho + Er + Tm + Yb + Lu) contents (∑HREE = 2.3 – 50.8 ppm and Lu_N = 1.2 - 33.9). Most garnet displays Eu anomalies (Eu*= primitive mantle normalized Eu/(0.5*Sm + 0.5*Gd)) of 1.03 – 2.50 (Samples DGE-5, DGE-6, DGBO2, DGO-3, DGO-4, DGO-5, DGO-6, DGO-7, DGO-11, DGO-12, DGO-13, DGO-15, BO-16, DGO-17 and DGO-18), whilst others exhibit negative Eu anomalies of 0.72 – 0.95 (Samples DGE-1, DGE-2, DGE-4, DGE-8, DGO-8, DGO-9 and DGO-14). Samples that have no Eu anomaly (i.e. Eu* from 0.95 – 1.05) are DGE-3 and DGO-1. Garnet from the Bellsbank and Bobbejaan eclogite are in general LREE-depleted (as is typical for mantle derived eclogites, (Aulbach and Jacob, 2016) However, garnet from samples DGO-1 and DGO-12 show the largest relative depletions in La (La_N = 0.2 and 0.1 respectively).

Garnet has variable Ni (25 - 300 ppm), V (40 - 374 ppm) and Sc (15 - 155 ppm) contents. Based on the classification scheme of Coleman (1965; Figure 3), the group B Bellsbank and Bobbejaan garnet have higher Ni (25 – 300 ppm), and lower Sc (15 - 155 ppm) contents compared to Group A garnets (51 - 76 ppm Ni and 58 - 92 ppm Sc). Garnet from Group C (DGO-1) has markedly low HREE contents (∑HREE = 3.6 ppm) compared to garnet from Group A and B eclogites (∑HREE = 2.3 to 50.8 ppm), as well as elevated V (374 ppm) compared to group A (125 - 180 ppm). V content

for group B garnet is variable, however samples DGE-4 (329 ppm), DGE-6 (329 ppm), DGO-4 (301 ppm), DGO-9 (355 ppm) and DGO-12 (294 ppm) have elevated samples compared to other Group B samples.

Clinopyroxene from the Bellsbank and Bobbejaan eclogites are in general light rare earth element (LREE) enriched, having negative sloped chondrite-normalized rare earth element (REE) patterns (as is expected for mantle derived clinopyroxene, Jacob, 2004; Figure 5). Clinopyroxene (except for DGE-1, DGE-3 and DGO-2) shows variably LREE-enriched (La/Sm ~ 1.05 - 9.51) and HREE-depleted (∑HREE = 0.01 – 3.36 ppm) patterns. Several clinopyroxenes display positive Eu anomalies of 1.05 – 3.6 (samples DGE-4, DGE-5, DGE-6, DGO-2, DGO-5, DGO-6, DGO-7, DGO-8, DGO-11, DGO-13, DGO-14, DGO-16, DGO-17 and BO18), while other clinopyroxene have slight negative Eu anomalies of 0.88 – 0.95 (samples DGE-2, DGO-3, DGO-4, DGO-9, DGO-12 and DGO-15). Samples DGE-1, DGE-3, and DGE-8 do not show any Eu anomaly (i.e. Eu* = 0.95 – 1.05). Sample DGO-10 has Eu values below the detection limit.

The Bellsbank and Bobbejaan eclogite clinopyroxene contain variable Sr (9 - 192 ppm) and Sc (2 - 43 ppm) contents, and while Rb is mostly below the detection limit, sample DGO-12 contains 0.38 ppm. Clinopyroxene plotting as Group C (Figure 4) have higher Ni (790 – 3395 ppm vs. 374 - 1619 ppm) and lower Ti (1094 – 2280 ppm vs. 917 - 3929 ppm) contents compared to Group B samples, but Group B clinopyroxene have higher V (319 – 1047 ppm vs. 164 -919 ppm) and Sc contents (10 - 43 ppm vs. 1.8 – 13.8 ppm) than Group C samples. Sr content in clinopyroxene is higher (20 – 192 ppm) in group B eclogites than in Group C eclogites (9 – 57 ppm).

Eclogite xenoliths BE-3, BO-3, BO-4, BO-6, BO-10, BO-11, BO-13, BO-15 and BO-16 have HREE abundances close to the detection limit (Figure 5), and therefore have elevated 2-sigma errors (Appendix table 5), thus the reported HREE contents need to be treated with caution.

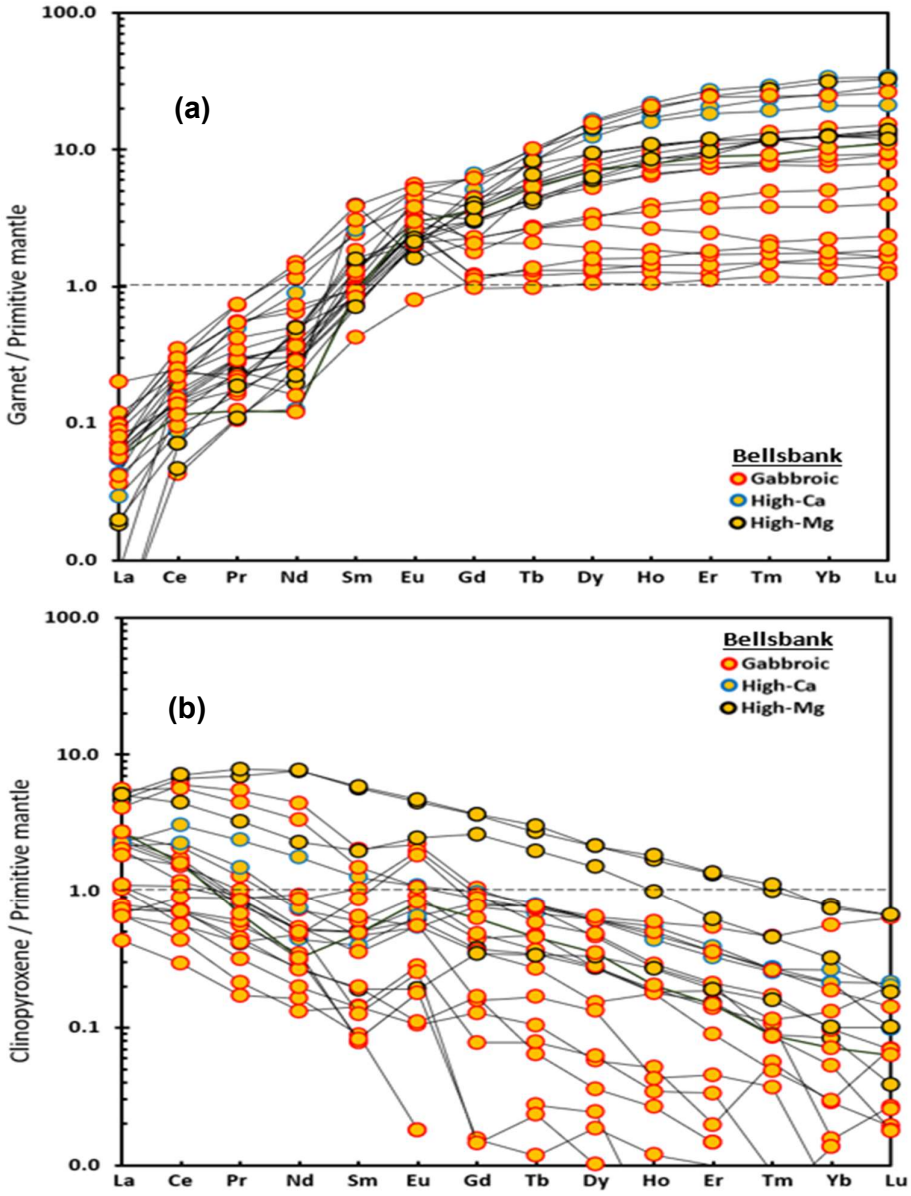

Figure 5. *Primitive mantle normalized REE compositions of Bellsbank and Bobbejaan* ***(a)*** *garnet and* ***(b)*** *clinopyroxene. Normalizing values from McDonough and Sun, (1995).*

3.3 Garnet oxygen isotope compositions

Garnet from Bellsbank and Bobbejaan eclogites have a range of $\delta^{18}O$ values between +2.74 and +6.25 ± 0.12 ‰ (Table 3). Previously reported oxygen isotope compositions for Bellsbank and Bobbejaan eclogitic garnets

range from +2.5 to +7.2 ‰ (Shervais *et al.,* 1988; Caporuscio and Smyth, 1990; Neal *et al.,* 1990; Shu *et al*., 2016). Garnet from eclogite sample DGO-14 has a $\delta^{18}O$ value (+5.25 ± 0.12 ‰) falling within the mantle range of +5.5 ± 0.4 ‰ (Mattey *et al*., 1994), while the remainder of the eclogite xenoliths have values outside of the mantle range (Figure 7, 10). Group A garnets have $\delta^{18}O$ values between +3.43 and +6.25 ‰, whereas Group B garnets have $\delta^{18}O$ values between +4.04 and +5.25 ‰, and a lower mean (n = 20) of +4.04 ‰.

3.4 Reconstructed whole-rock eclogite compositions

The effect of secondary processes such as host kimberlite infiltration and alteration (e.g. secondary phlogopite along grain boundaries) on calculated versus measured whole-rock compositions can be evaluated based on the addition of ~5 wt.% kimberlite liquid (Schmidberger and Francis, 2001). It has been found that intensely altered constituent mineral phases such as carbonate, zircon and rutile - which are included in the measured whole-rock composition - significantly affect trace element content to reflect the chemistry of the host kimberlite (Figure 14). While the approach of a calculated whole-rock vs. measured whole-rock composition results in a quantitative limitation, it allows for qualitative paragenetic analysis (Schmidberger and Francis, 2001). Therefore, a reconstructed whole-rock based on modal proportions of alteration free constituent minerals is done to obtain a more robust representative whole-rock eclogite composition.

There is inherent difficulty in accurately determining the modal abundance of garnet and clinopyroxene in eclogite xenoliths due to their small size, coarse texture, and the fact they sample a limited volume of their source rock (Aulbach and Jacob, 2016). The trace element distribution between garnet and clinopyroxene, however, is relatively insensitive to changes in their modal abundance (Aulbach and Jacob, 2016; Aulbach *et al.,* 2017). Small changes to the modal proportions of garnet to clinopyroxene in

calculated whole-rock compositions results in minimal changes to the overall trace element abundance pattern (Jerde *et al.,* 1993; Jacob and Foley, 1999). However, the major element composition of the eclogite xenoliths can change significantly due to modal variation. Thus, for the major element bulk rock calculation, modal abundances of primary phases, estimated both visually on hand samples as well as petrographically using full-section scans (Table 1, 4 and Figure 2) were used.

A 45% garnet to 55% clinopyroxene split was applied to major element calculations for samples without visible amounts of kyanite, rutile and corundum. The same 45% garnet and 55 % clinopyroxene abundance was used for all trace element calculations. The addition of up to 10% modal kyanite and corundum resulted in increased whole-rock Al_2O_3 and SiO_2 content, as per mineral modes in Table 4. The addition of rutile will increase the TiO_2 and high field strength elements (HFSE) such as Zr, Hf, Ti and Nb. A Ti mass-balance calculation has been applied to remove negative Ti anomalies (Aulbach and Viljoen, 2015; Aulbach and Jacob, 2016), by including trace amounts (< 0.002 wt.%) of eclogitic rutile into the major and trace element calculation (Table 4, Appendix Table 6).

Aulbach and Jacob (2016), outlined the following eclogite classification scheme based on bulk rock Eu anomalies and garnet composition: “Gabbroic” eclogites have N-MORB normalized (values from Gale *et al.,* 2013) Eu* > 1.05 and “non-gabbroic” eclogites have Eu* < 1.05. Additionally, non-gabbroic eclogites are ‘High-Ca’ if their garnet Ca-number (Ca#) is above 0.2. If the garnet Ca# is less than 0.2, the non-gabbroic eclogites are either ‘High-Mg’ (garnet Mg# ≥ 0.6) or ‘Low-Mg’ (garnet Mg# < 0.6). Based on these criteria, the majority of the Bobbejaan and Bellsbank samples (n = 16) are Gabbroic, with several High-Ca (e.g. DGE-2, DGE-4, DGE-8, DGO-9, DGO-14), some High-Mg (e.g.. DGE-1, DGE-3, DGO-8) and no ‘Low-Mg’ occurrences (Figure 6, Table 4). The whole-rock eclogite major element compositions are broadly basaltic and picritic (Le Bas, 2000) and have variable MgO (5.3 - 15.8 wt.%), Al_2O_3 (12.9 - 24.6 wt.%), CaO

(10.1 - 14.7 wt.%), SiO_2 (46.2 - 49.2 wt.%), Na_2O (1.8 - 4.8 wt.%) and TiO_2 (0.1 - 0.4 wt.%) contents.

3.4.1. Gabbroic eclogites

While all of the Bellsbank and Bobbejaan eclogites show negative correlations between Al_2O_3 and Na_2O vs. MgO (Figure 6), Gabbroic samples extend to higher Al_2O_3 and Na_2O contents (maximum 24 and 4.8 wt.%) compared to the High-Mg (maximum 15.9 and 2.3 wt.%) and High-Ca samples (maximum 24.6 and 4.4 wt.%). The CaO content of Gabbroic samples extends to marginally higher values (maximum 14.7 wt.%) compared to the High-Mg and High-Ca samples (maximum 11.9 and 14.5 wt.% respectively).

The Gabbroic eclogites generally plot within the Kaapvaal eclogite and modern gabbro fields in terms of FeO vs. MgO (Figure 6), however 3 samples have higher Al_2O_3 and lower SiO_2 when compared to Kaapvaal eclogites and modern gabbro literature data. Gabbroic samples mostly fall outside of the field of MORB data, except for a few samples which lie within the MORB field in FeO vs. MgO and SiO_2 vs. MgO space. Four gabbroic samples that plot outside these fields contain kyanite (DGO-3, DGO-10, DGO-13), have higher Al_2O_3 contents (< 22 wt.%) and trend to lower SiO_2 (Figure 6).

Gabbroic eclogites have distinctly positive N-MORB-normalized Eu anomalies (Eu* = 1.10 - 2.59), and flat to mildly fractionated HREE patterns (Lu/Gd = 1.0 - 4.7) (Table 4, Figure 7). Gabbroic eclogite samples have markedly lower overall HREE contents than non-gabbroic samples (∑HREE mean = 6.1 ppm vs. 15.3 ppm).

Table 4. Calculated eclogite whole-rock compositions for the Bellsbank and Bobbejaaan eclogite xenoliths

Sample	DGE-1	DGE-2	DGE-3	DGE-4	DGE-5	DGE-6	DGE-8	DGO-1	DGO-2	DGO-3	DGO-4	DGO-5	DGO-6	DGO-7	DGO-8	DGO-9	DGO-10	DGO-11	DGO-12	DGO-13	DGO-14	DGO-15	DGO-16	DGO-17	DGO-18
Trace classification	High-Mg	High-Ca	High-Mg	High-Ca	Gabbroic	Gabbroic	High-Ca	High-Ca	Gabbroic	Gabbroic	Gabbroic	Gabbroic	Gabbroic	Gabbroic	High-Mg	High-Ca	Gabbroic	Gabbroic	Gabbroic	Gabbroic	High-Ca	Gabbroic	Gabbroic	Gabbroic	Gabbroic
Major classification	A	B	A	B	B	B	B	C	B	B	B	B	B	B	A	B	B	B	B	B	B	B	B	B	B
Modal abundance																									
Garnet	0.45	0.45	0.45	0.45	0.45	0.45	0.45	0.40	0.45	0.40	0.45	0.45	0.45	0.45	0.45	0.45	0.45	0.45	0.45	0.40	0.45	0.45	0.45	0.45	0.45
Clinopyroxene	0.55	0.55	0.55	0.55	0.55	0.55	0.55	0.50	0.55	0.55	0.55	0.55	0.55	0.50	0.55	0.55	0.50	0.50	0.55	0.50	0.55	0.55	0.54	0.55	0.54
Kyanite	-	-	-	-	-	-	-	0.09	-	0.04	-	-	-	0.05	-	-	0.04	0.05	-	0.09	-	-	-	-	-
Corundum	-	-	-	-	-	-	-	0.01	-	0.01	-	-	-	-	-	-	0.01	-	-	0.01	-	-	0.01	-	0.01
Rutile	-	Trace	-	Trace	Trace	Trace	Trace	-	-	-	-	-	-	-	Trace	-	-	-	Trace	-	-	-	-	-	Trace
SiO_2	49.0	48.3	48.0	47.9	47.9	47.9	47.8	46.2	49.1	47.6	47.8	48.5	47.2	47.0	47.3	48.8	48.6	47.4	47.8	46.9	47.7	49.1	48.1	49.2	47.4
TiO_2	0.4	0.3	0.4	0.2	0.4	0.4	0.4	0.1	0.2	0.1	0.2	0.2	0.2	0.2	0.3	0.1	0.1	0.1	0.3	0.1	0.2	0.2	0.2	0.1	0.3
Al_2O_3	12.9	14.8	15.9	14.6	17.7	13.6	15.0	24.6	18.5	21.6	19.8	15.9	15.7	17.2	13.4	16.1	22.3	18.9	14.8	24.0	17.2	19.0	18.6	19.3	16.0
Cr_2O_3	0.08	0.10	0.09	0.05	0.06	0.20	0.05	0.01	0.01	0.02	0.07	0.10	0.03	0.05	0.21	0.06	0.02	0.11	0.04	0.02	0.09	0.08	0.21	0.02	0.06
FeO	8.9	7.5	8.7	8.8	7.6	8.3	10.3	4.0	6.2	4.5	5.4	7.2	7.9	7.5	9.7	7.8	5.1	6.5	8.2	4.6	6.7	5.8	6.5	5.2	7.8
MnO	0.3	0.1	0.3	0.2	0.1	0.2	0.2	0.1	0.1	0.1	0.1	0.1	0.1	0.1	0.2	0.2	0.1	0.1	0.2	0.1	0.1	0.1	0.1	0.1	0.2
MgO	15.8	11.3	14.9	11.3	8.2	12.2	9.6	5.3	9.8	8.9	8.0	11.2	11.6	11.3	13.7	9.8	8.8	10.8	11.4	8.4	10.3	8.4	9.4	9.2	11.4
CaO	10.9	14.5	10.1	14.1	13.5	14.7	13.6	14.4	12.5	11.8	13.1	13.5	12.4	13.5	11.9	14.2	11.4	12.6	13.8	10.8	12.4	13.2	13.1	12.1	13.5
Na_2O	2.0	2.9	1.8	2.7	4.2	2.4	2.9	4.4	4.2	4.6	4.8	3.1	3.3	2.4	2.3	3.4	4.2	3.1	2.8	4.3	4.0	4.5	4.0	4.7	2.9
K_2O	0.022	0.003	0.021	0.008	0.011	0.008	0.018	0.067	0.010	0.009	0.007	0.006	0.010	0.007	0.010	0.004	0.005	0.005	0.008	0.007	0.008	0.004	0.005	0.006	0.010
NiO	0.024	0.044	0.017	0.055	0.042	0.065	0.018	0.028	0.107	0.104	0.085	0.088	0.053	0.074	0.051	0.050	0.112	0.082	0.038	0.116	0.107	0.055	0.067	0.117	0.057
Total	100.3	99.9	100.1	99.9	99.7	99.8	99.8	99.2	100.7	99.3	99.3	100.0	98.6	99.3	99.1	100.3	100.6	99.7	99.4	99.3	98.7	100.3	100.2	100.1	99.4
V	359	517	336	654	517	632	524	-	139	153	522	591	389	392	354	727	113	213	708	111	624	444	445	177	427
Ni	256	404	244	572	469	747	217	-	981	1122	970	949	648	869	516	457	1368	927	388	1284	1069	554	767	1970	675
Sc	61.2	76	60.5	68.8	42.3	28.4	74.3	-	9.9	11.3	38.8	31.1	26.9	43.9	37.5	71.1	8.6	36.2	93.5	9.1	23.4	25.8	18.0	8.9	39.3
Rb	0	0	0	0.008	0	0.078	0.042	-	0.037	0.038	0.024	0	0	0	0	0	0	0.012	0.209	0	0.19	0	0	0	0
Th	0.03	0.11	0.03	0.12	0.02	0.16	0.05	-	0.05	0.04	0.08	0.11	0.11	0.11	0.18	0.06	0.04	0.03	0.15	0.04	0.07	0.05	0.05	0.04	0.11
U	0.01	0.03	0.02	0.03	0.03	0.05	0.04	-	0.04	0.01	0.01	0.02	0.02	0.01	0.02	0.01	0.03	0.02	0.04	0.03	0.02	0.01	0.01	0.02	0.02
Nb	0.64	0.20	0.66	0.24	0.42	0.70	0.19	-	0.12	0.02	0.09	0.67	0.25	0.00	0.04	0.17	0.04	0.14	0.48	0.02	0.00	0.74	0.28	0.03	0.36
Ta	0.093	0.050	0.100	0.034	0.080	0.085	0.073	-	0.007	0.001	0.002	0.027	0.013	0.0	0.034	0.004	0.004	0.003	0.085	0.003	0.112	0.013	0.006	0.007	0.050
La	1.77	0.82	1.92	0.89	0.28	1.56	0.87	-	0.26	0.18	0.28	1.02	0.91	0.76	1.91	0.43	0.31	0.71	2.12	0.33	0.84	0.30	0.41	0.44	1.04
Ce	6.56	2.34	6.98	1.62	1.10	6.00	3.15	-	0.65	0.36	0.61	2.18	1.79	1.18	4.39	0.81	0.92	1.62	5.81	0.93	1.59	0.87	0.66	1.23	1.66
Pr	1.08	0.26	1.21	0.14	0.23	0.90	0.42	-	0.09	0.05	0.06	0.23	0.17	0.15	0.51	0.09	0.15	0.19	0.77	0.16	0.15	0.11	0.07	0.18	0.12
Pb	0.14	0.32	0.17	0.08	0.02	0.23	0.04	-	0.06	0.01	0.03	0.08	0.10	0.18	0.24	0.05	0.02	0.15	0.60	0.02	0.29	0.01	0.08	0.04	0.12
Sr	105.73	20.65	103.26	21.18	31.34	45.09	50.76	-	15.68	8.94	5.20	26.31	12.76	42.11	36.08	11.16	19.07	24.47	64.74	19.72	17.87	14.02	13.61	29.68	14.57
Nd	5.93	0.74	6.01	0.40	1.60	3.99	1.86	-	0.63	0.32	0.28	0.75	0.62	0.80	1.84	0.38	0.65	0.63	3.30	0.67	0.51	0.48	0.32	0.68	0.31
Sm	1.69	0.29	1.74	0.27	0.93	0.98	0.83	-	0.58	0.20	0.31	0.36	0.32	0.50	0.62	0.20	0.22	0.26	0.97	0.21	0.91	0.31	0.18	0.20	0.31
Zr	35.60	3.57	35.35	4.78	10.59	14.84	12.81	-	13.63	2.84	2.88	8.05	6.38	11.53	10.09	2.16	3.37	4.62	4.96	3.41	5.90	2.30	2.37	2.93	7.71
Hf	1.04	0.23	1.10	0.70	1.27	1.50	1.32	-	0.43	0.12	0.17	0.38	0.34	0.44	0.94	0.15	0.15	0.22	0.21	0.13	0.68	0.12	0.16	0.15	0.78
Eu	0.57	0.21	0.60	0.24	0.47	0.59	0.41	-	0.46	0.20	0.23	0.35	0.27	0.52	0.39	0.17	0.19	0.25	0.49	0.21	0.18	0.24	0.18	0.18	0.30
Ti	3749	2431	3549	2205	3837	3684	3623	-	1577	1064	1778	2008	1370	1727	2992	855	921	1408	3042	969	1809	1337	1446	1299	2400
Gd	1.99	1.63	2.01	1.45	1.76	1.52	2.09	-	0.81	0.32	1.03	0.98	0.95	1.32	1.87	1.19	0.32	0.53	1.93	0.32	0.70	0.65	0.63	0.26	1.15
Tb	2.85	0.51	0.39	0.45	0.40	0.32	0.53	-	0.15	0.06	0.29	0.23	0.25	0.30	0.43	0.42	0.06	0.14	0.54	0.06	0.27	0.14	0.13	0.05	0.29
Dy	2.85	5.66	2.93	4.36	3.16	2.61	4.86	-	0.90	0.48	2.75	1.86	2.00	2.70	3.75	4.89	0.43	1.11	5.49	0.45	2.41	1.12	0.97	0.35	2.46
Y	18.4	44	19.1	34.1	19.8	15.8	31.9	-	4.7	2.6	19.5	12.8	12.4	18.5	23.5	39.9	2.4	7.2	41.4	2.6	16.7	7.2	5	2.1	15.6
Ho	0.72	1.64	0.79	1.31	0.80	0.59	1.22	-	0.19	0.10	0.77	0.51	0.50	0.72	0.89	1.47	0.09	0.29	1.57	0.11	0.65	0.26	0.20	0.08	0.60
Er	2.45	5.94	2.46	4.49	2.52	1.78	4.04	-	0.51	0.28	2.55	1.63	1.61	2.38	2.73	5.37	0.27	0.95	5.34	0.31	2.01	0.81	0.54	0.24	1.96
Tm	0.43	0.98	0.44	0.80	0.40	0.27	0.65	-	0.08	0.05	0.45	0.27	0.26	0.40	0.41	0.92	0.05	0.17	0.83	0.05	0.40	0.13	0.07	0.04	0.31
Yb	2.96	7.50	3.00	5.74	2.73	2.02	4.71	-	0.54	0.33	3.19	1.88	1.69	2.84	2.86	6.94	0.32	1.12	5.56	0.35	2.30	0.85	0.49	0.26	2.31
Lu	0.46	1.14	0.48	0.99	0.42	0.31	0.70	-	0.08	0.06	0.51	0.32	0.27	0.46	0.40	1.09	0.04	0.18	0.88	0.06	0.38	0.13	0.08	0.04	0.37
Eu*	0.99	0.77	1.01	0.95	1.14	1.53	0.94	-	2.12	2.47	1.17	1.71	1.41	1.90	1.05	0.84	2.24	2.07	1.10	2.59	0.68	1.65	1.53	2.45	1.40
Sr*	1.5	1.6	1.4	3.0	1.9	0.9	2.0	-	2.3	2.6	1.4	2.2	1.4	4.3	1.3	2.1	2.1	2.5	1.5	2.1	2.3	2.2	3.3	3.0	2.5
Lu/Gd	2.2	6.6	2.3	6.4	2.3	2.0	3.2	-	1.0	1.7	4.7	3.0	2.7	3.3	2.0	8.7	1.3	3.3	4.3	1.6	5.1	1.9	1.2	1.5	3.1
∑HREE	12.7	23.4	10.5	18.1	10.4	7.9	16.7	-	2.4	1.4	10.5	6.7	6.6	9.8	11.5	21.1	1.3	4.0	20.2	1.4	8.4	3.4	2.5	1.1	8.3

Major elements in wt.% oxides; trace elements in ppm; "-": below detection limit; "": no value; Mg#: molar Mg/(Mg+Fe_{TOTAL})*100; Ca#: molar Ca/(Ca+Mn+Fe+Mg); Eu*: Eu/(0.5*Gd + 0.5*Sm), using N-MORB normalized values (Gale et al. 2013); Sr*: Sr/(0.5*Pr + 0.5*Nd), using N-MORB normalized values (Gale et al. 2013); Major classification: garnet major element classification of Coleman (1965); Trace classification: trace element classification scheme of Aulbach and Jacob (2016)(see Section 3.4); ∑HREE: Tb+Ho+Er+Tm+Yb+Lu. Fe content is reported as FeO total.*

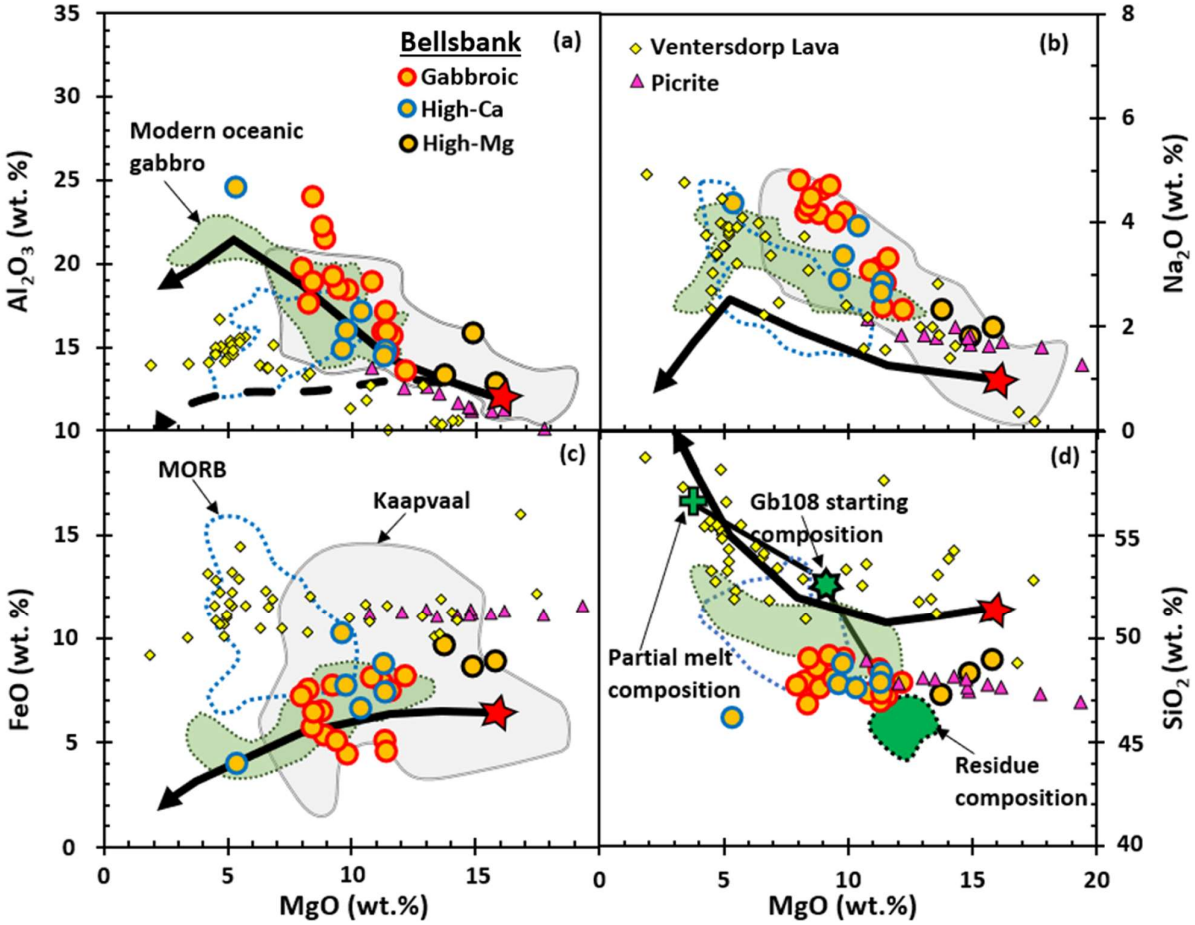

Figure 6. *Calculated whole rock multi-element variation diagrams depicting compositions (wt. %) of Bellsbank and Bobbejaan eclogites. Global MORB data shown by the blue stippled line from Jenner & O'Neill (2012). Altered and fresh modern oceanic gabbro compositions shown by the green field from Bach et al. (2001). Ventersdorp mafic volcanics (yellow squares) from Crow and Condie. (1988), Marsh et al. (1992). Picrite from Eggins (1993).* ***(a)*** *Comparative Al_2O_3 vs. MgO plot showing Bellsbank and Bobbejaan eclogites broadly plotting close to oceanic gabbro and MORB fields, although many gabbroic eclogites have elevated Al_2O_3 contents. High-Mg samples plot close to picrite compositions and fall outside of the field for oceanic gabbro and MORB.* ***(b)*** *Na_2O vs. MgO reveals a close association of the gabbroic and high-Ca eclogite samples with modern oceanic gabbro and MORB fields. High-Mg samples plot closer to picrite compositions.* ***(c)*** *FeO vs. MgO plot showing gabbroic and high-Ca eclogites plotting close to samples from modern oceanic gabbro and MORB.* ***(d)*** *SiO_2 vs. MgO plot showing Gabbroic, High-Mg and High-Ca samples plot outside of the fields for modern oceanic gabbro and MORB. Trend lines depict fractionation trends modelled at 1 GPa (black line) and 3 GPa (black stippled line) using pMelts software (Ghiorso et al. (2002) from starting composition (red star). Data from partial melting experiments of Yaxley and Sobolev. (2007) show in (d). Kaapvaal eclogite compositions calculated from* (MacGregor and Manton, 1986; Ongley *et al*., 1987; Caporuscio and Smyth, 1990; Appleyard *et al*., 2004; Viljoen *et al*., 2005; Jacob *et al*., 2009; Gréau *et al.,* 2011; Aulbach and Viljoen, 2015; Riches *et al.,* 2016b; Shu *et al*., 2016; Aulbach *et al*., 2016; Huang *et al.,* 2016; Aulbach *et al.,* 2017). *Eclogites have been classified into Gabbroic, High-Mg and High-Ca groups after Aulbach and Jacob (2016). See section 3.4 for further classification details. Further details on partial melt modelling (d) and pMelts forward modelling (a - c) can be found in section 4.2.2.*

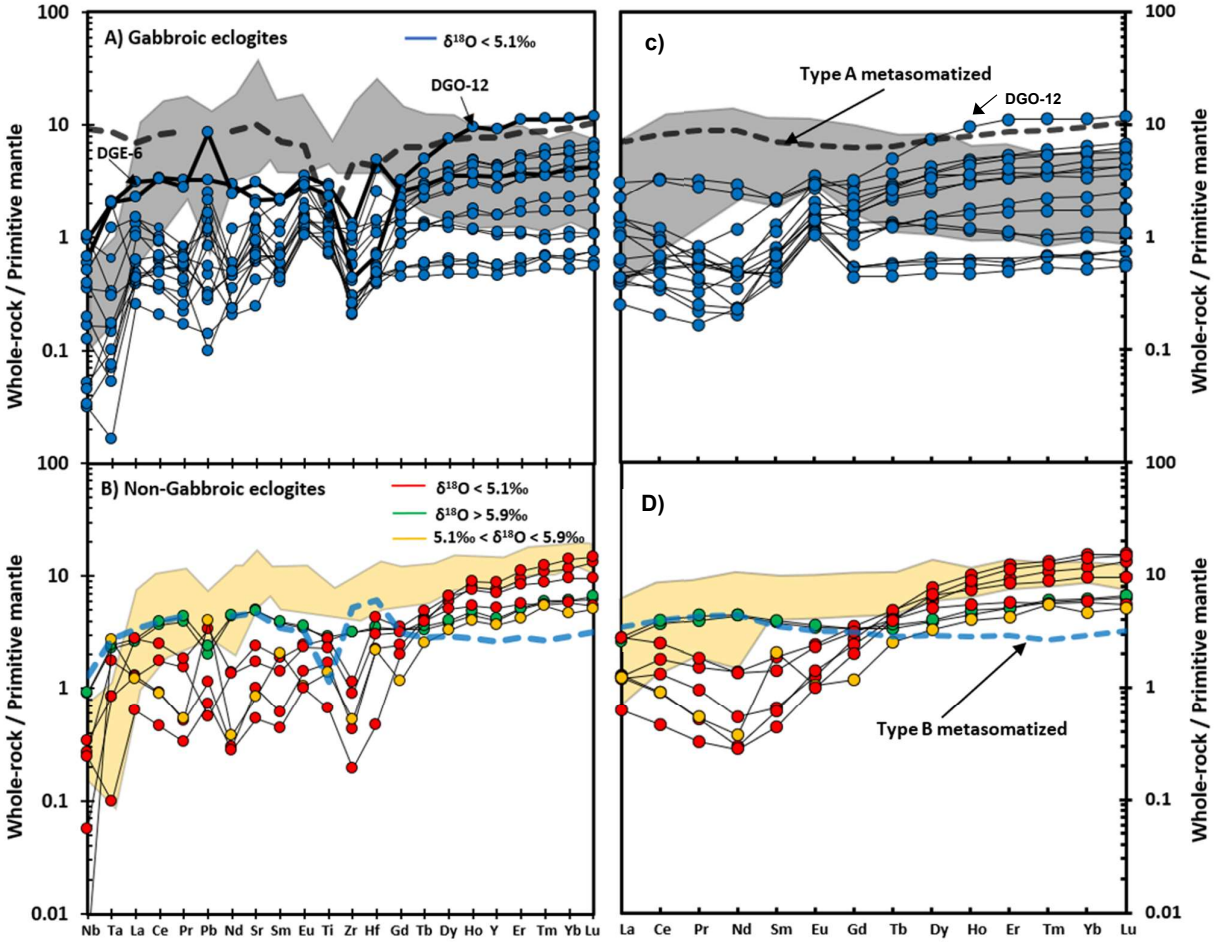

Figure 7. *Calculated bulk eclogite multi-element diagram normalized to primitive mantle (values from McDonough and Sun, 1995). Gabbroic eclogites plotted in* ***(a)*** *and non-gabbroic (see section 3.4 for classification details) eclogites plotted in* ***(b)****. REE primitive mantle normalized plots of gabbroic eclogites plotted in* ***(c)*** *and non-gabbroic eclogites in* ***(d)****. The eclogites have been further grouped according to their oxygen isotope composition (Table 2) in comparison to the known* $\delta^{18}O$ *value of the mantle (+5.5 ± 0.4‰; Mattey et al., 1994). Blue solid circles: gabbroic eclogites with* $\delta^{18}O$ *values < +5.1 ‰; yellow solid circles: non-gabbroic eclogites with* $\delta^{18}O$ *values within the mantle range (+5.1 to +5.9 ‰); red solid circles: non-gabbroic eclogites with* $\delta^{18}O$ *values < +5.1 ‰; green lines non-gabbroic eclogites with* $\delta^{18}O$ *values >+5.9 ‰. Grey field in a) and c) shows metasomatized eclogites from Robert Victor kimberlite Radu et al. (2019). Yellow field in b) and d) shows non-metasomatized eclogites from Robert Victor kimberlite Radu et al. (2019). Black stippled line (Type A) and blue stippled line (Type B) represent metasomatized eclogite average whole rock compositions from Jacob et al. (2009).*

3.4.2. High-Mg and High-Ca eclogites

No obvious correlation between FeO vs. MgO is evident (Figure 6) for the Bellsbank and Bobbejaan non-gabbroic whole-rock compositions. High-Mg

eclogite xenoliths have the highest MgO contents (13.7 - 15.8 wt.%), as well as amongst the lowest Al_2O_3 (12.9 - 15.9 wt.%) and Na_2O (1.8 - 2.3 wt.%) contents of all the Bellsbank and Bobbejaan eclogites. The High-Mg samples show a slightly wider range in SiO_2 content (43.7 - 49 wt.%) compared to Gabbroic samples (46.9 - 49.2 wt.%).

High-Mg eclogites have less fractionated N-MORB normalized Lu/Gd (2.0 - 2.3 vs. 3.2 - 8.7) compared to High-Ca eclogites (values for N-MORB from Gale et al., 2013) (Figure 7). The High-Mg eclogites have Eu* values between 0.99 and 1.05 whereas the High-Ca eclogites have lower Eu* values between 0.68 and 0.95 (Table 4). Sample DGO-8 has an Eu* value of 1.045 which is close to being considered as a positive anomaly which would change its classification to gabbroic. High-Ca samples have a larger range of Sr anomalies (Sr* = N-MORB normalized Sr/(Pr*0.5 + Nd*0.5)) compared to the High-Mg samples (1.6 - 3.0 vs.1.3 - 1.5), although are lower than Gabbroic samples (Sr* = 0.9 - 4.3).

3.4.3. Bulk eclogite trace element signatures and garnet oxygen isotope compositions

Most Bellsbank and Bobbejaan eclogites that have garnet $\delta^{18}O$ values below (2.74 - 4.61 ‰) the mantle range (5.5 ± 0.4 ‰) of Mattey *et al*. (1994) are Gabbroic, excluding the High-MgO eclogite DGO-8, and the High-Ca eclogite xenoliths DGE-4, DGE-8, andDGO-14. All eclogite xenoliths with garnet $\delta^{18}O$ values above the mantle range are non-gabbroic (Figure 7; Table 4).

Gabbroic eclogites with garnet $\delta^{18}O$ values below 5.1 ‰ have markedly lower bulk HREE contents (∑HREE mean = 6.1 ppm, n = 16) compared to non-gabbroic eclogites with garnet $\delta^{18}O$ values below 5.1‰ (∑HREE mean = 16.9 ppm, n = 4). The non-gabbroic High-Ca eclogite with a garnet $\delta^{18}O$ value within the mantle range (DGO-14) has the lowest bulk HREE content

(∑HREE = 8.4 ppm) compared to all other High-Mg and High-Ca eclogites (∑HREE mean = 16.3, n = 7; Table 4; Figure 7).

3.5 Thermobarometry and oxybarometry

The equilibration pressures and temperatures for Bellsbank and Bobbejaan eclogite xenoliths were calculated using three methods (Table 5). None of these methods take into consideration the effect of Fe^{3+} content on the exchange geothermometer, but this has been found to be negligible when considering the experimental error of the thermometer itself (Purwin *et al.*, 2013).

The Fe-Mg exchange garnet-clinopyroxene geothermometer of Krogh Ravna (2000), T_{KR00}, was first solved iteratively with the geobarometer of Beyer *et al*. (2015), P_{B15}, starting at an initial pressure of 5 GPa. The pressure calculated using the Beyer *et al*. (2015) geobarometer is dependent on number of Si cations (< 1.985) in the clinopyroxene formula, which can lead to an uncertainty of ~0.5 GPa with 100 °C temperature uncertainty. The experimental uncertainty with T_{KR00} is approximately ± 30 °C. The geobarometer P_{B15} was experimentally calibrated for bi-mineralic eclogite xenolith mineral equilibration at pressures of 3 - 7 GPa and temperatures between 1200 - 1550 °C, with an experimental error of ± 0.4 GPa (Beyer *et al*., 2015). The experimental error, however, increases with pressure, which can result in larger underestimations (Beyer *et al*., 2015). The T_{KR00} - P_{B15} calibration yields temperatures between 849 and 1218 °C, and pressures between 3.0 and 6.7 GPa for the Bellsbank and Bobbejaan eclogite xenoliths. The majority (19 out of 26) of Bellsbank and Bobbejaan eclogites plot within diamond stable pressure and temperature conditions when considering the T_{KR00} - P_{B15} thermometer-barometer combination (Figure 8).

The second method involved calculating pressure and temperature iteratively through a combination of T_{KR00} projected onto an assumed local conductive model geotherm $P_{40mWm^{-2}}$ (surface heat-flow of 40 mWm^{-2}; Griffin *et al*., 2003; Hasterok and Chapman, 2011). The T_{KR00} - P_{40mW} calibration yields temperatures between 822 and 1203 °C, and pressures between 3.2 and 5.3 GPa for the Bellsbank and Bobbejaan eclogite xenoliths.

The third method involved iteratively solving the combination of T_{KR00} projected onto a peridotite derived geotherm, P_{FPG}, using published peridotite xenolith data from the Finsch kimberlite (Skinner, 1989; Gibson et al., 2008; Lazarov et al., 2009). The T_{KR00} - P_{FPG} calibration yields temperatures between 823 and 1259 °C, and pressures between 3.2 and 6.0 GPa for the Bellsbank and Bobbejaan eclogite xenoliths. Fewer samples (7 out of 26) from the Bellsbank and Bobbejaan eclogites plot within diamond stable pressure and temperature conditions when considering the results of the T_{KR00} - P_{FPG} combination. These results trend between the 42 mW/m^2 and 40 mW/m^2 model cratonic conductive geotherms of Hasterok and Chapman, (2011), which is close to the assumed local conductive model geotherm $P_{40mWm^{-2}}$ (surface heat-flow of 40 mW/m^2; Griffin *et al.,* 2003; Hasterok and Chapman, 2011).

Eclogites and garnet pyroxenites from the Bellsbank kimberlite have been found to have a range of equilibrium temperatures (842 to 1173 °C) and pressures (3.7 GPa to 6.3 GPa), as well as Sm-Nd two point isochron ages corresponding to a paleo-geothermal gradient between 46 mW/m^2 to 38 mW/m^2 at 120 Ma (Shu *et al.,* 2014). Studies on peridotite xenoliths from the Group II Finsch kimberlite (ca. 118 Ma) reveal a paleo-geothermal gradient between 40 mW/m^2 and 41 mW/m^2 down to ~200 km depth, which makes it reasonable to assume a similar geothermal gradient for the nearby Bellsbank kimberlite (Lazarov *et al*., 2009) (Figure 8).

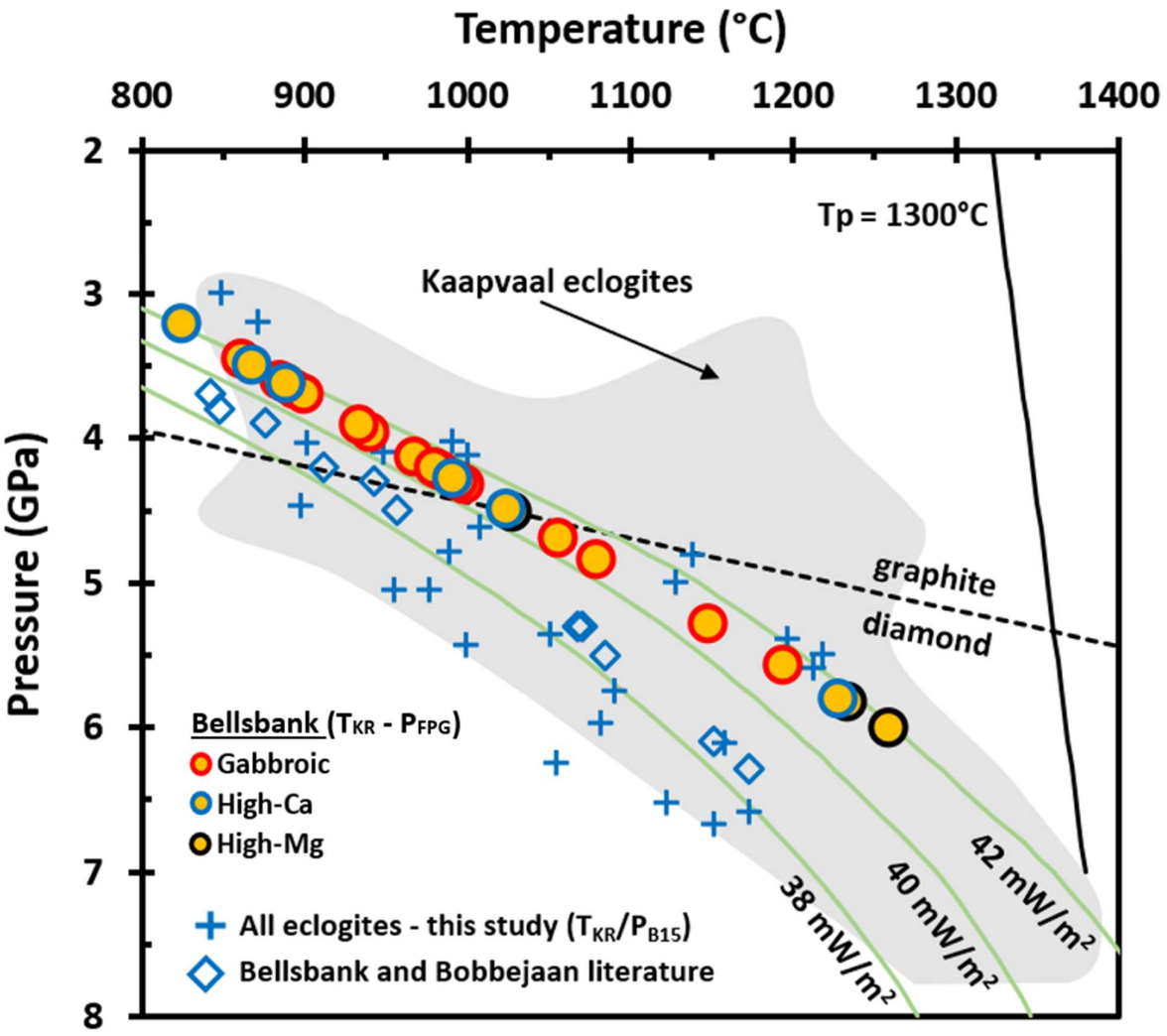

Figure 8. *Equilibration pressures and temperatures for the Bellsbank and Bobbejaan eclogite xenoliths based on the Fe-Mg exchange thermometer of Krogh Ravna (2000) (T_{KR}) iteratively with the Finsch peridotite derived geotherm (P_{FPG}) using data from Lazarov et* al. *(2009) and Skinner, (1989). Blue plus symbols: equilibration pressures and temperatures for the Bellsbank and Bobbejaan eclogite xenoliths based on the Fe-Mg exchange thermometer of Krogh Ravna (2000) (T_{KR}) solved iteratively with the barometer of Beyer et al. (2015) (P_{B15}) starting at an assumed pressure of 5 GPa. Blue diamonds: pressure and temperature results for Bellsbank and Bobbejaan eclogites from Shu et al. (2014). Grey region: published eclogite compositions from the Kaapvaal craton* (MacGregor and Manton, 1986; Ongley et al., 1987; Caporuscio and Smyth, 1990; Appleyard et al., 2004; Viljoen et al., 2005; Jacob *et al*., 2009; Gréau *et al*., 2011; Aulbach and Viljoen, 2015; Riches *et al.,* 2016b; Shu *et al*., 2016; Aulbach *et al*., 2016; Huang *et al.,* 2016; Aulbach *et al*., 2017) *recalculated using the formulation of Krogh Ravna (2000) and Beyer et al. (2015). Black stippled line: diamond/graphite stability fields after Kennedy, (1976). Black solid line: mantle potential temperature curve from Kimura and Kawabata (2012). Model cratonic geotherms of 38, 40 and 42 mW/m^2 from Hasterock and Chapman (2011).*

Table 5. Calculated equilibrium pressures, temperatures and oxygen fugacities of the Bellsbank eclogite xenoliths

Sample	Class	T_{KR00}[1] (°C)	P_{B15} (GPa)	T_{KR00}[2] (°C)	$P_{40mw/m2}$ (GPa)	T_{KR00}[3] (°C)	P_{FPG} (GPa)	logfO_2 (ΔFMQ)	σ + (ΔFMQ)	σ - (ΔFMQ)	Gt $Fe^{3+}/\sum Fe$	Gt $Fe^{3+}/\sum Fe$
DGE-1	High-Mg	1218	5.5	1203	5.3	1259	6.0	-4.2	-4.2	-4.2	0.036	±0.01
DGE-2	High-Ca	1213	5.6	1189	5.3	1227	5.8	-2.4	-2.4	-2.5	0.028	±0.01
DGE-3	High-Mg	1196	5.4	1181	5.2	1232	5.8	-3.8	-3.8	-3.9	0.039	±0.01
DGE-4	High-Ca	902	4.0	864	3.4	868	3.5	-2.4	-1.9	-2.1	0.020	±0.01
DGE-5	Gabbroic	1173	6.6	1037	4.4	1055	4.7	-1.8	-1.7	-1.9	0.025	±0.01
DGE-6	Gabbroic	1128	5.0	1117	4.8	1147	5.3	-2.6	-2.6	-2.7	0.026	±0.01
DGE-8	High-Ca	897	4.5	823	3.2	823	3.2	-2.5	-2.4	-2.6	0.018	±0.01
DGO-1	High-Ca	1050	5.4	980	4.1	991	4.3	-1.4	-1.3	-1.4	0.024	±0.01
DGO-2	Gabbroic	949	4.1	930	3.8	940	4.0	-3.1	-2.9	-3.2	0.011	±0.01
DGO-3	Gabbroic	999	5.4	888	3.6	894	3.7	-2.2	-2.0	-2.3	0.014	±0.01
DGO-4	Gabbroic	871	3.2	894	3.6	900	3.7	-2.8	-2.6	-3.0	0.009	±0.01
DGO-5	Gabbroic	849	3.0	882	3.5	888	3.6	-3.2	-3.1	-3.4	0.012	±0.01
DGO-6	Gabbroic	1055	6.2	879	3.5	884	3.6	-3.2	-3.0	-3.3	0.014	±0.01
DGO-7	Gabbroic	1151	6.7	983	4.1	998	4.3	-3.1	-3.0	-3.3	0.014	±0.01
DGO-8	High-Mg	990	4.0	1005	4.2	1028	4.5	-3.1	-3.0	-3.1	0.034	±0.01
DGO-9	High-Ca	1000	4.1	1006	4.2	1023	4.5	-2.0	-2.0	-2.1	0.026	±0.01
DGO-10	Gabbroic	1007	4.6	970	4.0	983	4.2	-	-	-	-	-
DGO-11	Gabbroic	988	4.8	923	3.8	933	3.9	-3.2	-3.1	-3.4	0.012	±0.01
DGO-12	Gabbroic	1139	4.8	1158	5.1	1194	5.6	-2.1	-2.1	-2.2	0.028	±0.01
DGO-13	Gabbroic	1082	6.0	956	3.9	967	4.1	-2.6	-2.4	-2.7	0.012	±0.01
DGO-14	High-Ca	977	5.1	882	3.5	888	3.6	-2.7	-2.6	-2.8	0.014	±0.01
DGO-15	Gabbroic	1158	6.1	1058	4.5	1079	4.8	-2.2	-2.1	-2.4	0.014	±0.01
DGO-16	Gabbroic	954	5.1	857	3.4	860	3.4	-2.4	-2.3	-2.5	0.014	±0.01
DGO-17	Gabbroic	1123	6.5	966	4.0	979	4.2	-2.0	-1.9	-2.2	0.016	±0.01
DGO-18	Gabbroic	1090	5.8	979	4.1	994	4.3	-2.5	-2.4	-2.6	0.020	±0.01

[1] formulation of Krogh, Ravna (2000), (T_{KR}) , solved iteratively with Beyer (2015), (P_{B15}), starting at an assumed pressure of 5 GPa ; [2]: formulation of T_{KR} projected onto a 40mW/m^2 conductive Geotherm of Hasterock and Chapman (2011) and solved iteratively ; [3]: formulation of T_{KR} , projected onto a straight line approximating the geotherm of published Finsch peridotite data (P_{FPG}) (Data from Lazarov et al. (2009), Skinner, (1989)), and solved iteratively. Oxygen fugacity (relative to ΔFMQ) calculated after the oxybarometry methods of Stagno et al. (2015), using the T_{KR}-P_{FPG} combination. Propagated errors in the fO_2 calculated using garnet $Fe^{3+}/\Sigma Fe$ absolute uncertainties of ±0.01. Class: trace element classification scheme of Aulbach and Jacob (2016)(see Section 3.4).

The latter two calibrations are more consistent, yielding temperature results within 0.7 to 56 °C and pressure results within 0.01 to 0.67 GPa of each other, which is significantly lower when compared to the first calibration of T_{KR00} - P_{B15} (-170 to 55 °C and -2.6 to 0.8 GPa). The results of the T_{KR00} - P_{B15} and T_{KR00} - P_{FPG} thermobarometry calculations are shown in Figure 8, highlighting the tendency of the T_{KR00} - P_{B15} combination to over-estimate pressure conditions. The T_{KR00} - P_{FPG} combination will therefore be presented in the oxybarometry and discussion chapters that follow.

The Gabbroic Bellsbank and Bobbejaan eclogite xenoliths exhibit a slightly smaller range in equilibration temperatures (860 - 1194 °C vs. 823 - 1259 °C) and pressures (3.4 - 5.6 GPa vs. 3.2 - 6.0 GPa) compared to non-gabbroic eclogites, although considering the uncertainties on the pressure and temperature calculations there may not be a significant difference.

High-Mg samples show a range of equilibration temperatures between 1028 and 1259 °C, whereas High-Ca samples have a range of 823 to 1023 °C. High-Mg samples have a range of equilibration pressures of 4.5 to 6.0 GPa, whereas the High-Ca samples have a range of 3.2 to 4.5 GPa.

The redox states of the Bellsbank and Bobbejaan eclogites were calculated using the oxybarometer of Stagno *et al.* (2015) with the equilibration temperature and pressure results from the T_{KR00} - P_{FPG} calibration (Table 5; Figure 9). This oxybarometer employs the following end-member equilibrium equation; $5CaFeSi_2O_6 + 1/3Ca_3Al_2Si_3O_{12} + O_2 = 2Ca_3Fe_2Si_3O_{12} + 1/3Fe_3Al_2Si_3O_{12} + 4SiO_2$.

The main uncertainty of the Stagno *et al*. (2015) oxybarometer is from garnet Fe^{3+} measurements whereby uncertainties in fO_2 estimates are associated with decreasing ferric iron content. This can result in uncertainties > 0.5 log units when $Fe^{3+}/\Sigma Fe$ ratios are < 0.05. Propagated errors using an absolute garnet $Fe^{3+}/\Sigma Fe$ uncertainty of ± 0.01 are ± 0.2 log units (Table 5). The uncertainties associated with temperature inputs (T_{KR00}

- P_{FPG}) correspond to pressure changes along the conductive model geotherm, which is turn is reflected by uncertainties of calculated fO_2.

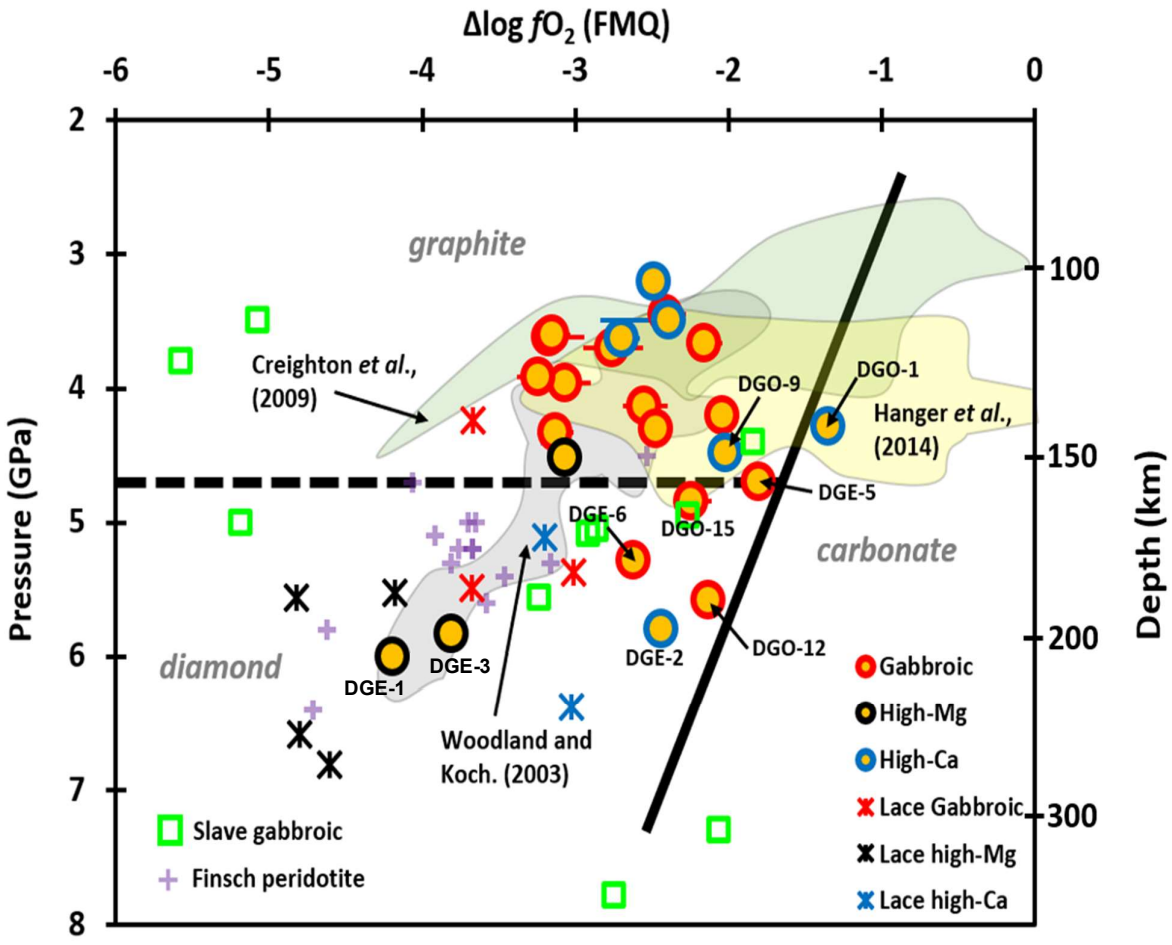

Figure 9. *Results of oxybarometry showing oxygen fugacity (normalized to the FMQ buffer) vs. equilibration pressure for the Bellsbank and Bobbejaan Gabbroic (red circle), High-Mg (black circle) and High-Ca (blue circle) eclogites using the formulation of Stagno et al. (2015), with pressures calculated using the T_{KR}-P_{FPG} combination. Finsch peridotite data (purple symbols) from Lazarov et al. (2009). Gabbroic (red star), High-Mg (black star) and High-Ca (blue star) eclogite xenoliths of Lace kimberlite from Aulbach et al. (2017). Bultfontein Group I kimberlite-derived peridotite xenolith data (green field) from Creighton et al. (2009). Various Kaapvaal craton kimberlite derived lherzolitic and harzburgitic xenolith data (grey field) from Woodland and Koch. (2003). Wesselton kimberlite derived peridotite data (yellow field) from Hanger et al. (2014). Eclogite xenolith data from the Slave craton (green squares) from Smart et al. (2017). Diamond, graphite and carbonate stability fields from Stagno et al. (2015). Error bars shown are propagated errors in the fO_2 calculation using garnet $Fe^{3+}/\sum Fe$ absolute uncertainties of ±0.01 (Table 5).*

The fO_2 values of the Bellsbank and Bobbejaan eclogites range between -1.4 to -4.2 log units below the Fayalite-Magnetite-Quartz (FMQ) buffer. Gabbroic samples show the largest range in fO_2 values (Δlog fO_2 from -3.2 to -1.8) compared to High-Ca (Δlog fO_2 from -2.7 to -1.4) and High-Mg (Δlog fO_2 from -4.2 to -3.1).

The eclogites have a range of relatively oxidized and reduced redox states at different pressures. For the deepest eclogites with equilibration pressures of > 5 GPa, the High-Mg eclogites have the lowest fO_2 values (Δlog fO_2 from -4.2 to -3.8) and mostly fall within the diamond stability field (Table 5; Figure 8; Figure 9). In comparison, the High-Ca and Gabbroic eclogites at these depths have some of the highest fO_2 values (Δlog fO_2 from -2.4 to -2.1).

At lower pressures of ~ 3 - 4 GPa, Gabbroic, High-Mg and High-Mg eclogites have a narrow range of fO_2 values (Δlog fO_2 from -3.2 to -2.2), where most eclogites fall within the graphite stability field. The Bellsbank eclogite xenoliths overlap well with Kaapvaal peridotites in terms of pressure vs. fO_2 space until pressure increases above ~ 4.5 GPa (Figure 9).

CHAPTER FOUR - DISCUSSION

4.1 The effects of mantle metasomatism and contamination by the host kimberlite magma

Bellsbank and Bobbejaan eclogitic xenoliths are likely to have been affected by metasomatism during their extended residence (since ~3.2 Ga; Shu *et al.,* 2016) within the cratonic mantle (Jacob *et al*., 2003; Schmidberger *et al.,* 2005; Lazarov *et al*., 2009; Gréau *et al*., 2011; Shu *et al*., 2016), which needs to be resolved before the petrogenesis can be understood. While the samples in this study were carefully selected to avoid extensively infiltrated and altered samples, an assessment of the degree of metasomatism is

crucial in understanding potential secondary overprinting. Significantly, incompatible trace element concentrations of constituent minerals are likely to have been altered due to interactions with metasomatic agents (e.g. kimberlitic melts, COH fluids and other volatiles) which contain an abundance of incompatible and mobile elements (Ireland *et al*., 1994; Barth *et al.,* 2001, 2002; Canil, 2004; Gréau *et al*., 2011).

Obvious metasomatism observed as kimberlite infiltration products, in-filled cracks and veins of phlogopite, as well as secondary mineral phases (e.g. diamond, graphite, corundum, rutile etc; Dawson, 1984) was avoided during in-situ laser ablation techniques on fresh mineral cores. This metasomatism can obscure primary protolith chemical signatures (e.g. Jacob, 2004; Gonzaga *et al.,* 2010; Smart *et al.,* 2012). However, despite efforts to avoid modal metasomatism, cryptic metasomatism (i.e. changes in trace element composition without new mineral growth; O'Reilly and Griffin (2013)) may still be present in the Bellsbank and Bobbejaan eclogite suite.

The products of metasomatism, however, aid in constructing petrogenetic models to explain the formation of mantle eclogites found in various cratons (e.g. Barth *et al.,* 2002; Jacob *et al*., 2009; Smart *et al.,* 2009). Metasomatism within the cratonic mantle driven by kimberlitic melts prior to entrainment is said to have less influence on whole rock calculated Ti, HREE and compatible elements such as Ni, Co, Zn, thereby allowing for robust constraints of precursor rocks (Jacob, 2004). Metasomatic effects on petrogenesis such as enrichments of La, Ce and Pr in the Bellsbank and Bobbejaan eclogite xenoliths is explored further in section 4.2.

4.1.1 Gabbroic eclogites

Gabbroic eclogite xenoliths from the Bellsbank and Bobbejaan kimberlite typically display little textural (e.g. coarse phlogopite, rutile and other mineral phases) evidence of modal metasomatism. Samples DGO-4, DGO-6, DGO-10, DGO-12 and DGO-16 have visible but trace amounts of phlogopite and carbonate mineral growth around garnet and clinopyroxene.

Garnet from the Gabbroic samples has fractionated HREE (primitive mantle values from McDonough and Sun, 1995) values (Lu_N = 1.2 - 26.2), with sample DGO-12 having the largest Lu_N (26.2) and the greatest ∑HREE content (43.8 ppm). Clinopyroxene from Gabbroic samples show variable LREE enrichment with Ce_N values between 0.29 and 6. Samples DGE-6 and DGO-12 have the highest Ce_N (values 6 and 5.7 respectively). This is reflected in the calculated whole rock trace element pattern whereby samples DGE-6 and DGO-12 have elevated Ce_N values (3.4 and 3.3) and the most enriched LREE and HREE patterns of all Gabbroic samples, displaying enrichments characteristic of metasomatized eclogites (Figure 7A, grey shaded region and stippled line). Enrichments of LREE's such as Ce in these two samples are likely from the interaction of primary clinopyroxene with a metasomatic agent prior to entrainment in the kimberlite (Jacob *et al*. 2003).

Gabbroic samples (excluding DGE-6 and DGO-12) from the Bellsbank kimberlite show similar incompatible element enrichments to samples from the Jericho kimberlite (Figure 11), and therefore do not show significant evidence of cryptic metasomatism by a LREE enriched fluid or melt (Smart *et al.,* 2014a), such as that observed in the phlogopite eclogites from the Kaapvaal (Jacob *et al*., 2009). Using diagnostic features (clinopyroxene Nb > 0.5 ppm) described by Aulbach and Jacob (2016), the Gabbroic eclogites do not show evidence for kimberlite contamination, except for samples DGE-6, DGO-12 and DGO-15 which have clinopyroxene Nb values above 0.5 ppm (0.92, 0.60 and 0.92 ppm respectively).

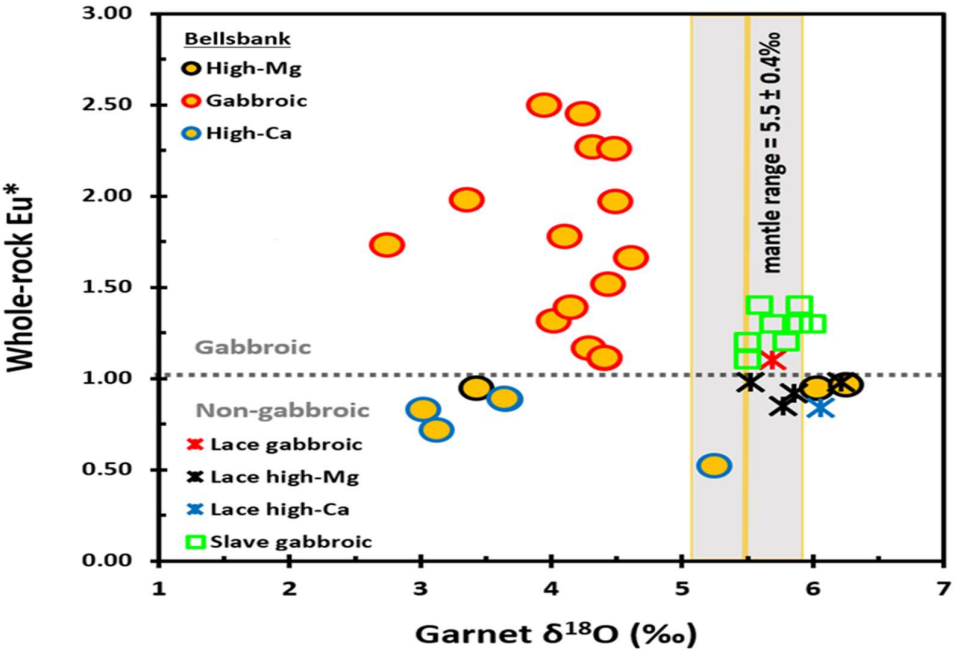

Figure 10. *Whole-rock europium anomaly (Eu*) vs. Garnet $\delta^{18}O$ for the Bellsbank and Bobbejaan Gabbroic (red circle), High-Mg (black circle) and High-Ca (blue circle) eclogites. Shown for comparison is Gabbroic (red star), High-Mg (black star) and High-Ca (blue star) eclogite xenoliths of Lace kimberlite from Aulbach et al. (2017). Slave gabbroic eclogite (green squares) data from the Slave craton from Smart et al. (2017). $\delta^{18}O$ value of the mantle +5.5 ± 0.4‰ from Mattey et al. (1994).*

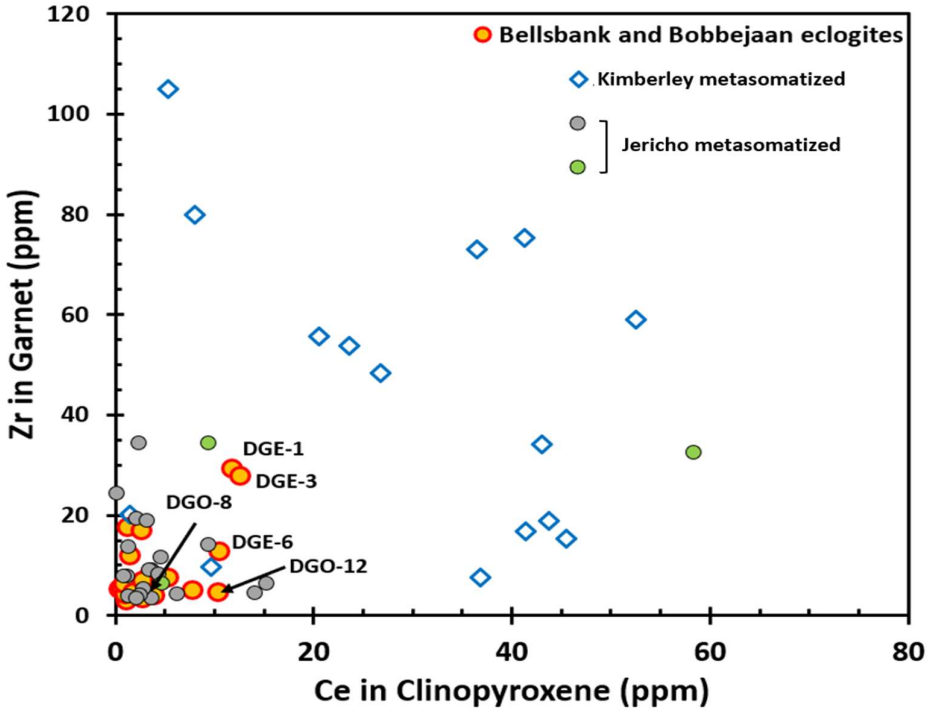

Figure 11. *Trace element contents (ppm) of Zr in garnet vs. Ce in clinopyroxene for the Bellsbank and Bobbejaan eclogites (orange/red circles). Metasomatized eclogite samples from the Kaapvaal (Jacob et al., 2009) and Slave* (Smart *et al.,* 2009, 2014b) *cratons shown for comparison.*

4.1.2 High-Mg and High-Ca eclogites

Non-gabbroic xenoliths from the Bellsbank and Bobbejaan kimberlite show minimal modal metasomatism, such as spongy rims around clinopyroxene and fine crystalline phlogopite. Sample DGE-1 contains visible phlogopite as well as large fine crystalline rims surrounding clinopyroxene, however the cores of these crystals appear fresh and un-altered.

Clinopyroxene from High-Mg samples (e.g. DGE-1, DGE-3, DGO-8) show the greatest enrichments of Ce_N (normalised to primitive mantle using values from McDonough and Sun 1989) values between 12.9 and 20.8. Samples DGE-1 and DGE-3 (Figure 13) show the largest concentrations of Ce in clinopyroxene vs. Zr in garnet, plotting near the High-Mg eclogite xenolith from the Jericho kimberlite which is interpreted as having crystallised or equilibrated with a LREE fluid or melt (cryptic metasomatism) within the Slave lithospheric mantle (Smart *et al.,* 2009).

Clinopyroxene from the High-Ca samples (DGE-2, DGE-4, DGE-8, DGO-1, DGO-9, DGO-14) have lower Ce_N values (2.1 to 8.8) than the High-Mg samples, however, have greater enrichments in garnet Lu_N values (29.4 to 98.7 vs. 34.7 to 39.9). This is translated onto calculated whole rock trace element patterns whereby High-Mg samples DGE-1, DGE-3 and DGO-8 show elevated Ce_N (3.7, 3.9 and 2.5 respectively) compared to High-Ca, and lie in the upper region (Figure 7B) of metasomatized eclogite xenoliths in terms of LREE enrichment.

The non-gabbroic eclogites do not show evidence for kimberlite contamination, except for High-Mg eclogites DGE-1 and DGE-3 which have slightly elevated Nb. The concentration of Nb in clinopyroxene is marginally above the limit (0.5 ppm), however garnet Sr and Nb concentrations are within the range given by Aulbach and Jacob, (2016). These samples are free from kimberlite contamination, however, show evidence of cryptic metasomatism.

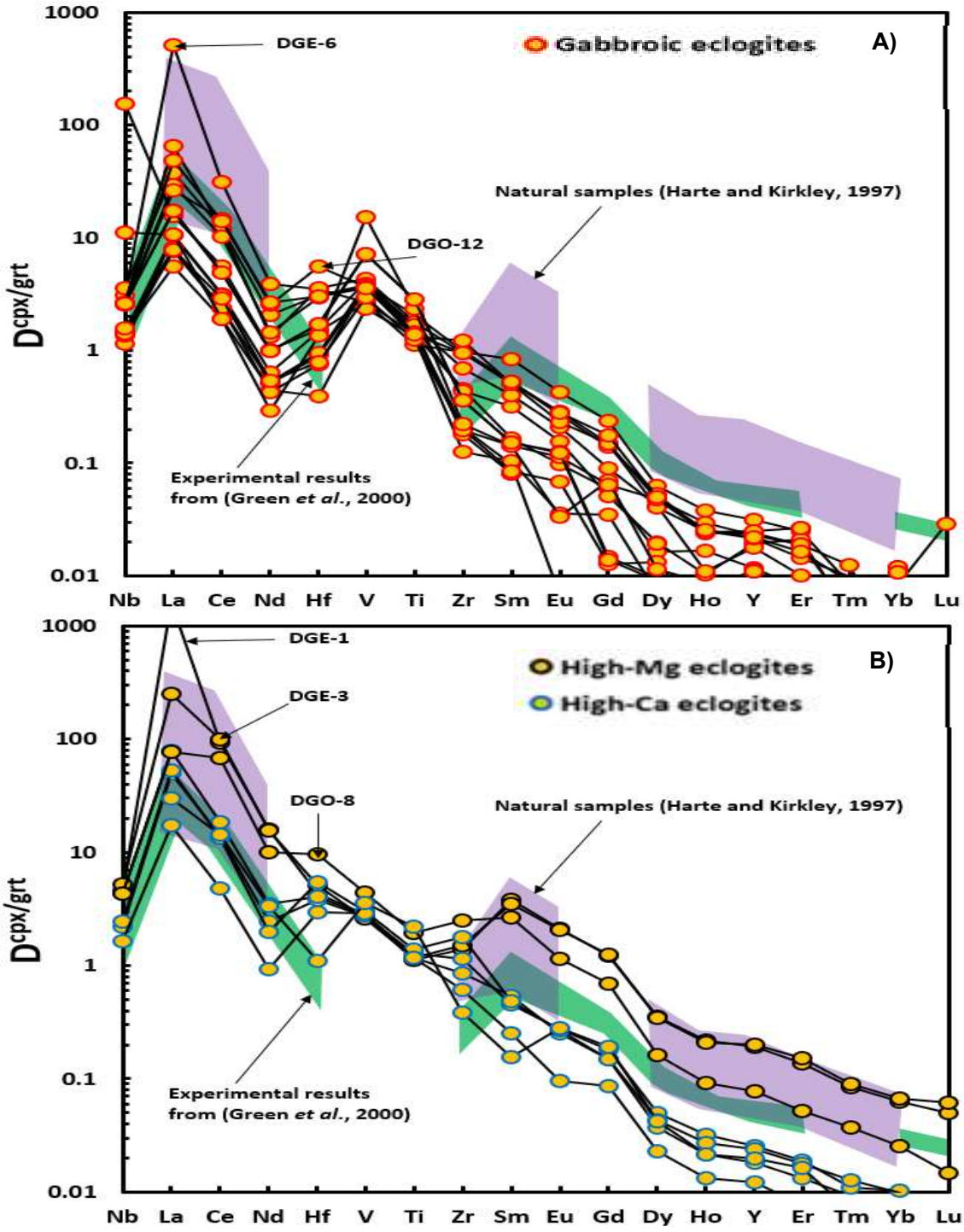

Figure 12. *Mineral equilibrium values* $D^{cpx/grt}$ *for the Bellsbank and Bobbejaan* ***(a)*** *Gabbroic and* ***(b)*** *High-Mg and High-Ca eclogite xenoliths compared to natural (purple field) and experimental (green field) determinations* (Harte and Kirkley, 1997; Green *et al.,* 2000).

High-Mg eclogite xenolith DGO-8 from the Bellsbank kimberlite plots near to those known to be free from apparent metasomatic overprinting (Smart *et al.,* 2014; Figure 11). High-Mg samples DGE-1 and DGE-3, however, show evidence for cryptic metasomatism (Figure 11). This is likely attributed to interaction with a LREE enriched fluid in the Kaapvaal SCLM prior to kimberlite entrainment.

4.1.3 Garnet / clinopyroxene trace element distributions as proxy for equilibrium

While the majority of Bellsbank and Bobbejaan eclogite xenoliths do not show abundant evidence for metasomatism, cryptic metasomatism is more difficult to elucidate. The presence of cryptic metasomatism can be evaluated by comparison of the trace element partitioning between garnet and clinopyroxene with both experimental results and natural samples.

Trace element partitioning between clinopyroxene and garnet ($D^{cpx/grt}$) for the Bellsbank and Bobbejaan eclogites agrees with natural and experimentally obtained partition coefficients (Figure 12), which is indicative of trace element equilibrium. It is evident that LREE's are concentrated in clinopyroxene and HREE's in garnet. This occurs in comparable ratios to those found in experiments and natural samples (Harte and Kirkley, 1997; Green *et al.,* 2000). More specifically, most Gabbroic eclogite xenoliths show lower ratios than those obtained experimentally, and more closely follow the trend seen for natural samples (Harte and Kirkley, 1997; Figure 12a). Given that the comparison is to experimental results for a high-pressure basalt (non-cumulate), it is expected that Gabbroic samples will have incorporated fewer incompatible elements during crystallisation. Non-gabbroic samples mostly (e.g. DGE-3 and DGO-8) fall within the experimental region of (Green *et al.,* 2000; Figure 12b, green shaded region) with exception to High-Mg sample DGE-1 which shows extremely elevated $D^{cpx/grt}$ values for La.

These differences, while still taken to indicate mineral equilibrium, are most likely attributable to differences in solidus temperatures and pressures associated with equilibrium (Green *et al.,* 2000; Blundy and Wood, 2003), as well as the absence of Rutile in the experimental system.

Overall, garnet and clinopyroxene from most Bellsbank and Bobbejaan eclogite xenoliths are in trace element equilibrium.

4.1.4 Fe^{3+} correlation with Ce and Sr as proxy for metasomatism

Garnet $Fe^{3+}/\sum Fe$ for Gabbroic samples correlates moderately with calculated whole rock Ce and Sr (R^2 = 0.57 and 0.53 respectively) values (Figure 16). High-Mg samples also show a correlation between Garnet $Fe^{3+}/\sum Fe$ and whole rock Ce and Sr (R^2 = 0.71 and 0.54 respectively). High-Ca samples do not show obvious correlation (Figure 16). Samples identified as displaying metasomatism (e.g. DGE-1, DGE-3, DGE-6, DGO-8 and DGO-12) have the highest Ce and Sr values, with the highest corresponding $Fe^{3+}/\sum Fe$ values. This level of LREE enrichment, which is a proxy for metasomatism, appears to increase with increasing garnet $Fe^{3+}/\sum Fe$. While garnet $Fe^{3+}/\sum Fe$ increases with depth, elevated whole rock Ce and Sr coupled with high garnet $Fe^{3+}/\sum Fe$ translates to decreased $\Delta \log fO_2$ (FMQ) values and can therefore be taken as evidence for an oxidative metasomatic signature.

The metasomatic agent responsible could therefore be enriched in Ce, La and have an increased Fe^{3+}content.

4.2 Petrogenesis of the mantle eclogite xenoliths from Bellsbank

The petrogenetic history of mantle derived eclogite xenoliths has been widely debated. There is an abundance of evidence supporting a low

pressure oceanic subduction related protolith, which formed at low pressures as pieces of subducted oceanic crust into the mantle (MacGregor and Manton, 1986; Taylor *et al.,* 1990; Jacob *et al.,* 1994; Beard *et al.,* 1996; Viljoen *et al*., 1996; Jacob *et al*., 2003; Smart *et al*., 2014a; Aulbach and Viljoen, 2015). There is also evidence to support a model where mantle eclogites form as a high pressure mantle cumulates (Caporuscio and Smyth, 1990; Griffin and O'Reilly, 2007).

Below, evidence from the Bellsbank and Bobbejaan eclogites geochemistry and stable isotope composition is used to argue in favour for an oceanic crustal protolith.

4.2.1 Major element similarities to mafic oceanic crust

Calculated whole-rock major element compositions of eclogites that superficially resemble modern oceanic gabbros (Figure 6) supports an origin from a gabbroic protolith. In terms of Al_2O_3 vs. MgO composition, the majority of the Bellsbank and Bobbejaan Gabbroic eclogites (except for DGO-3, DGO-10 and DGO-13) plot within or near to the field of modern oceanic gabbros, and along the Archean picrite 1 GPa fractional crystallization trend (Figure 6). The trend illustrated in Figure 6 is calculated using the 'pMelts' software of Ghiorso *et al.* (2002), using a starting composition of Archean picrite (Falloon *et al.,* 1999) undergoing equilibrium fractional crystallisation at 1 GPa. The starting composition, evolved liquid composition, and oxygen fugacity is presented in Appendix Table 7.

A compositional overlap with oceanic gabbros is less clear with Na_2O vs. MgO as most Gabbroic eclogites samples have higher Na_2O values, however, the eclogite xenoliths follow the liquid composition trend (black line) for an Archean picrite fractionally crystallising at 1 GPa. The chosen pressure of 1 GPa relates to the fact that oceanic crust in the Archean is considered to be up to a maximum of 40km thick (Mckenzie and Bickle,

1988). The Gabbroic eclogites overlap with the ocean gabbro field in terms of FeO composition, and trend along the 1 GPa fractional crystallization model line. Gabbroic eclogites show depletions of SiO_2 relative to oceanic gabbro, and therefore the majority do not overlap (Figure 6). This is attributed to partial melt loss from a gabbroic rock undergoing subduction related melting at high pressures (~ 4.5 GPa), resulting in an eclogite residue with increased MgO and decreased SiO_2 relative to the starting material (Yaxley and Sobolev, 2007).

High-Ca samples have compositional similarities close to modern MORB and follow the liquid composition trends of an Archean picritic melt differentiating at 1 GPa. Lower SiO_2 values compared to MORB and oceanic gabbro can be explained by the loss of a partial melt component, whereby High-Ca samples plot near an eclogitic residue (green field; Figure 6). While High-Mg samples do not coincide with the MORB and ocean gabbro fields (Figure 6), they plot close to the liquid composition trends of Archean picrite differentiating at 1 GPa. This provides evidence to suggest a common protolith, which experienced subsequent metasomatism or partial melting. High-Mg samples tend to have compositions similar to Archean mafic volcanics from the Ventersdorp, as well as picritic arc magmas that are basaltic in composition (Crow and Condie, 1988; Eggins, 1993).

From the 3 GPa (representing garnet stable conditions) liquid composition trends modelled with pMelts (using the same parameters mentioned above; Appendix Table 7), it is unlikely that the eclogite xenoliths crystallized as cumulates from basaltic-picritic melts at mantle pressures. To elucidate whether this is the case, based only on major element data, is difficult given the relatively simple bi-mineralic mineralogy of mantle eclogites (Schmickler *et al*., 2004). The presence of kyanite in High-Mg eclogite sample DGE-3 provides evidence against a high pressure mantle cumulate origin (Jacob and Foley, 1999; Jacob *et al*., 2009; Shu *et al*., 2016).

4.2.2 Trace element evidence for partial melting of oceanic crustal protoliths and overprinting by kimberlite melt

Trace element patterns of Gabbroic eclogite xenoliths overlap with modern oceanic gabbro fields (Bach *et al.*, 2001) (Figure 6, 7). This connection to an oceanic gabbro protolith is bolstered by the presence of positive Eu (Eu* = 1.1 – 2.59) and Sr (Sr* = 0.9 – 4.3) anomalies and flat to slightly fractionated HREE patterns. This provides evidence for the involvement of plagioclase and pyroxene crystallization during the formation of the protolith to these eclogite xenoliths. The Gabbroic samples show variable depletions in LREE, potentially due to the fractionation of incompatible elements during low pressure cumulate processes (Benoit *et al*.,1996).

During subduction of the oceanic gabbro rock, partial melt extraction causes depletion of incompatible elements in the residue (Barth *et al.*, 2001; Yaxely and Sobolev, 2007; Tappe *et al.*, 2011). Modelling of such partial melting, facilitated by high pressure experimental data (Figure 13), can provide insight into the depletion of incompatible elements. Using the gabbroic staring composition of GB108 glass from Yaxley and Sobolev (2007), partial melt extraction of 1%, 5%, 10% and 20% at high pressure (~ 4.5 GPa) and temperature (~ 1500 °C) conditions (see run C-1910; Yaxley and Sobolev, 2007) is presented (Figure 13). These models explain the depletion of LREE (i.e., La/Sm) in the whole-rock calculated residue, however, depletions of La, Ce, and Pr are too extreme to match the representative Gabbroic eclogite composition from the Bellsbank and Bobbejaan eclogites. Metasomatism of the eclogitic residue after partial melt extraction by a LREE-rich agent possibly explains the re-enrichment of La, Ce and Pr because the addition of 0.05 wt.% Group II kimberlite (grey line; Figure 14a; from Becker and le Roex, 2006) results in a close approximation to the representative Gabbroic eclogite composition (Figure 14a). Thus, an oceanic gabbro protolith with secondary minor kimberlite cryptic metasomatism is likely for the Bellsbank and Bobbejaan Gabbroic eclogite xenoliths.

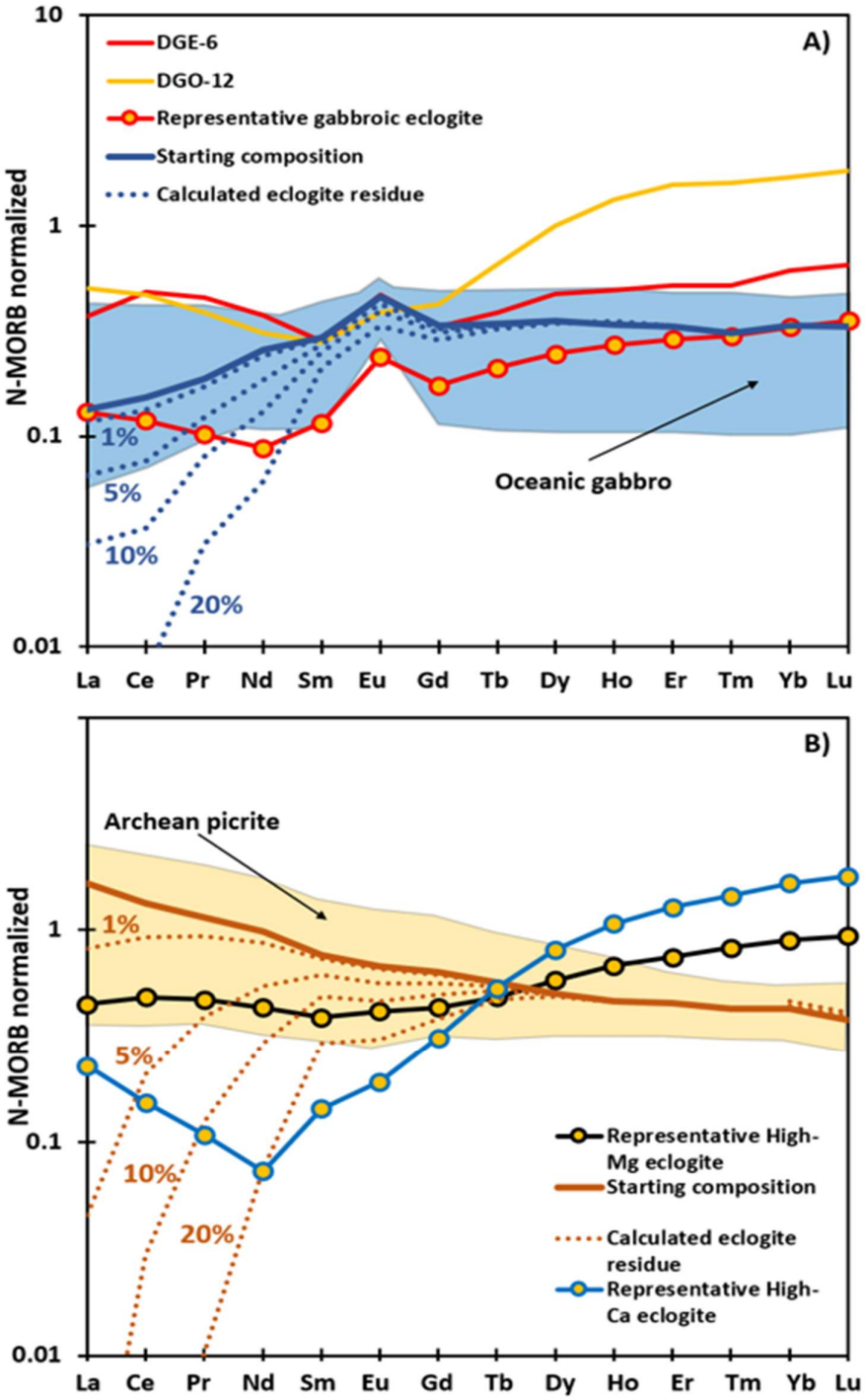

Figure 13. *NMORB-normalized REE modelling of partial melt extraction from potential eclogite protoliths.* ***(a)*** *Representative whole-rock Bellsbank and Bobbejaan Gabbroic eclogite (red line) compared to modern oceanic gabbros (blue field; Bach et al., 2001) and eclogite residues of between 1 to 20% batch partial melt extraction from a gabbroic precursor. Starting gabbro (GB108 glass) and partition coefficients from Yaxley and Sobolev, (2007),* ***(b)*** *Representative Bellsbank and Bobbejaan High-Mg (black line) and High-Ca (blue line) eclogites compared to Archean picrite (compiled from GEOROC; http://georoc.mpch-mainz.gwdg.de/georoc/). Shown for comparison eclogite residues of between 1 to 20% batch melt extraction from an average Archean picrite, using partition coefficients from Tuff and Gibson, (2007). Further details on partial melt modelling can be found in Section 4.2.1. Normalization values are from Gale et al. (2013).*

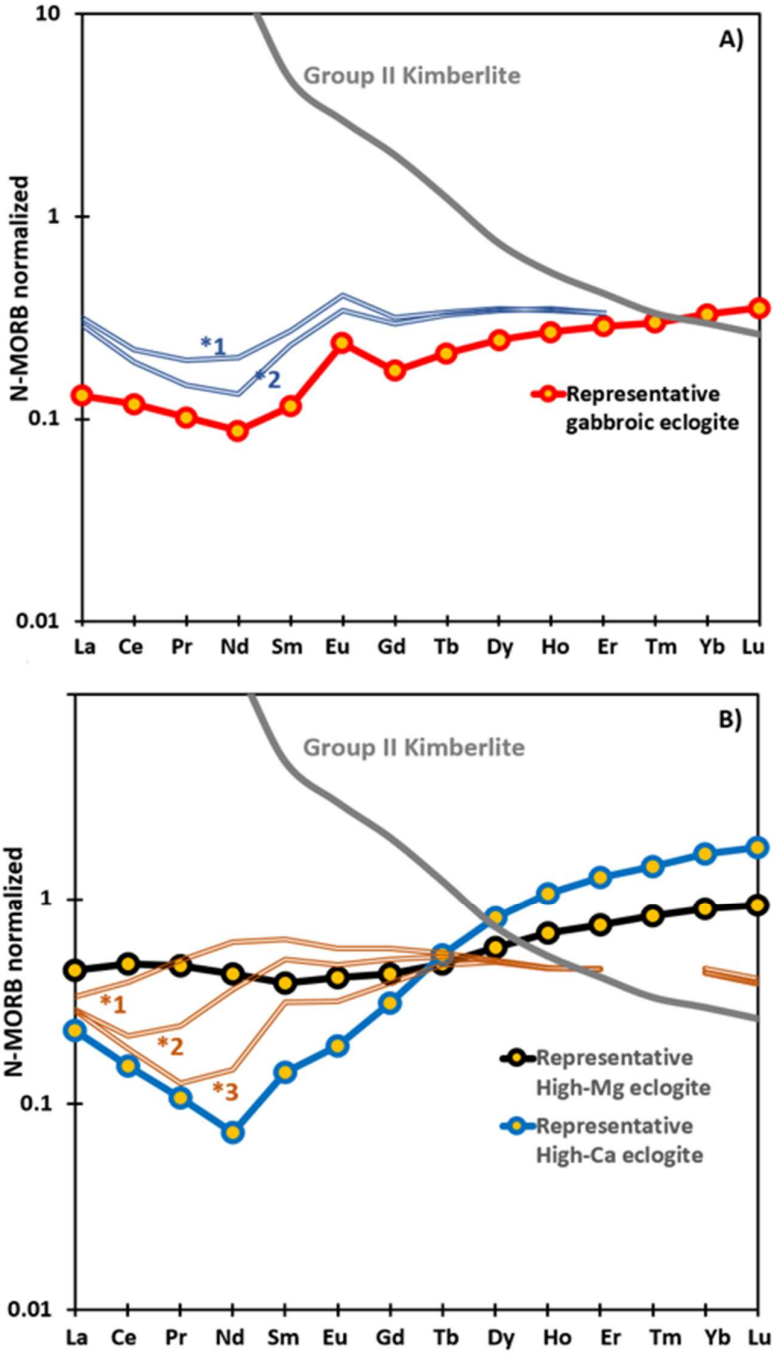

Figure 14. *NMORB-normalized REE modelling of partial melt extraction from potential eclogite protoliths and subsequent kimberlite addition.* ***(a)*** *Representative whole-rock Bellsbank and Bobbejaan Gabbroic eclogite (red line), with kimberlite infiltrated (0.05 wt. %) protolith derived from the 10 % partial melt (*1 blue line) and 20 % partial melt (*2 blue line) extraction from the starting gabbro (GB108 glass) composition and partition coefficients from Yaxley and Sobolev (2007).* ***(b)*** *Representative whole-rock Bellsbank and Bobbejaan High-Mg (black line) and High-Ca (blue line) with kimberlite infiltrated (0.05 wt. %) protolith derived from the 5 % partial melt (*1 brown line), 10% partial melt (*2 brown line), and 20% partial melt (*3 brown line) extraction from a starting Archean picrite (compiled from GEOROC; http://georoc.mpch-mainz.gwdg.de/georoc/; see figure 13 caption) composition, using partition coefficients from Tuff and Gibson (2007). Further details on partial melt modelling can be found in 4.2.1. Group II kimberlite (grey line) data from Becker & le Roex (2006). Normalization values are from Gale et al. (2013).*

High-Mg eclogite xenoliths display trace element patterns which mostly overlap with Archean picrite fields, suggesting derivation from a protolith that is picritic in composition (Figure 7). High-Mg samples have Tb/Sm ratios that correspond to an eclogitic residue after ~ 5 - 10% partial melt extraction at high pressure (> 3 GPa) from an average Archean picrite composition (brown line; Figure 13b) using partition coefficients from Tuff and Gibson, (2007). The modelled La, Ce and Pr contents of this residue, however, do not match those of the representative High-Mg eclogite. The addition of 0.05 wt.% group II kimberlite (grey line; Figure 14b; from Becker and le Roex, 2006) to the modelled residues (as a proxy for a LREE-rich metasomatic agent) can account for the LREE enrichment necessary to match a representative High-Mg Bellsbank eclogite xenolith (see *1 brown line Figure 14b). The protolith of the High-Mg eclogites from the Bellsbank and Bobbejaan kimberlite as Archean basaltic-picritic oceanic crust with subsequent kimberlite metasomatism therefore seems likely.

While High-Ca whole-rock trace element patterns do not superficially resemble an Archean picrite protolith. Higher degrees of partial melt extraction (~ 20 %) from an average Archean picrite (brown line; Figure 13b), followed by metasomatism from a group II kimberlite (grey line; Figure 14b; from Becker and le Roex, 2006) results in a pattern matching the representative High-Ca eclogite. An Archean basaltic-picritic ocean protolith subjected to secondary kimberlite metasomatism seems likely for the Bellsbank High-Ca eclogite xenoliths. This is supported by distinct LREE re-enrichments, relatively more enriched HREE patterns, weakly positive Eu anomalies and the lack of modal kyanite.

The Bellsbank and Bobbejaan suite exhibits a similar HREE vs. Eu* trend as other Kaapvaal eclogite xenoliths (Figure 15). Gabbroic samples have lower overall HREE content, and a wider range of Eu* (1 – 2.5), compared to non-gabbroic samples. This serves as evidence for cumulate plagioclase fractionation with olivine and clinopyroxene during the formation of the protolith. Although non-gabbroic samples have less variation in Eu* (< 1), they exhibit systematically higher HREE contents compared to Gabbroic

samples, which is interpreted as evidence for late stage basalt having extruded and rapidly cooled on the ocean floor, thereby 'freezing' all remaining incompatible heavy elements into the basalt (Coogan *et al.*, 2001; Coogan and Dosso, 2016; Leuthold *et al.*, 2018).

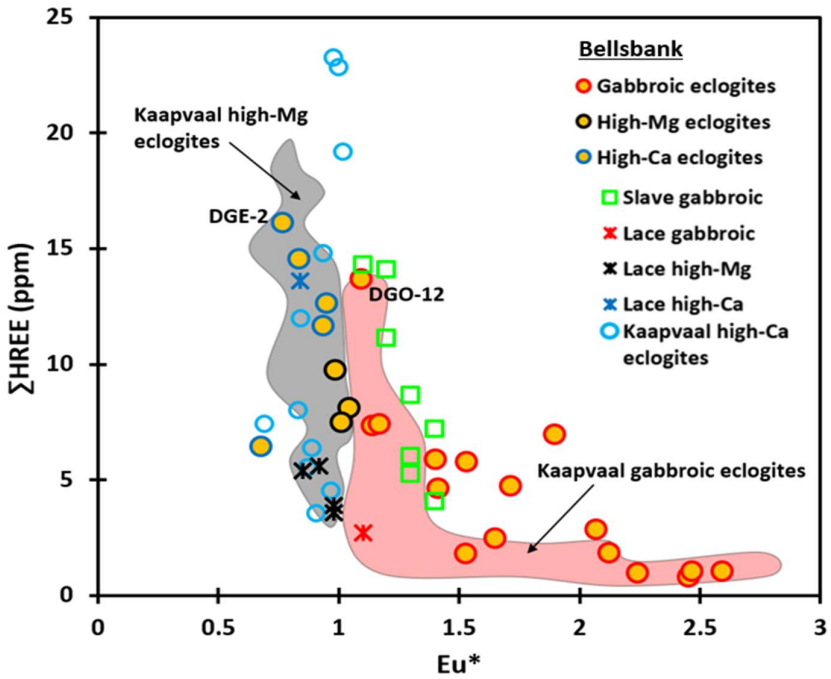

Figure 15. *Whole rock trace element ∑HREE (Tb + Dy + Ho + Er + Tm + Yb + Lu) vs. Eu* (N-MORB normalized Eu/(0.5*Gd + 0.5*Sm); Table 4) for the Bellsbank and Bobbejaan Gabbroic (red circle), High-Mg (black circle) and High-Ca (blue circle) eclogites. Shown for comparison is Gabbroic (red star), High-Mg (black star) and High-Ca (blue star) eclogite xenoliths of Lace kimberlite from Aulbach et al. (2017). Slave gabbroic eclogite (green squares) data from the Slave craton from Smart et al. (2017).*

4.2.3 Oxygen isotope fingerprint

Bellsbank and Bobbejaan garnet $\delta^{18}O$ values are used as a proxy for the whole rock eclogite $\delta^{18}O$ values. Earlier work highlights a small isotopic difference between garnet and clinopyroxene (± 0.6 ‰) due to small degrees of fractionation in the mantle (Caporuscio and Smyth, 1990). The $\delta^{18}O$ value of clinopyroxene, while not measured, is assumed to be in equilibrium with garnet at mantle temperatures as is shown for Kaapvaal eclogites (Radu *et al.*, 2019). Oxygen isotopic compositions of the Bellsbank and Bobbejaan eclogite xenoliths reveal a wide range of $\delta^{18}O$

values mostly outside of the expected mantle range of +5.5 ± 0.4 ‰ (Mattey *et al.*, 1994), which, when combined with evidence from trace element modelling, supports a low-pressure sea water hydrothermally altered gabbroic/picritic protolith (Alt *et al.*, 1986; Barth *et al.*, 2001; Jacob, 2004).

There is an abundance of investigations on eclogite $\delta^{18}O$ values which have been linked to the subduction of ocean crust (compilation in Aulbach and Jacob, 2016). The oxygen isotopic composition of MORB is not particularly sensitive to small degrees of partial melting (< 15 %) and metasomatic effects at mantle temperature and pressures, whereas low-temperature ocean water alteration can have a much greater fractionation effect on the $\delta^{18}O$ values (Alt *et al.*,1986; Bindeman *et al.*, 2012; Riches *et al.*, 2016a). Recent work on oxygen isotopic composition of mantle eclogites reiterates that $\delta^{18}O$ values as a proxy for their protolith must be used in conjunction with other geochemical and petrological evidence, as the criterion of $\delta^{18}O$ alone is not unambiguous (Korolev *et al.*, 2018).

High-Ca sample DGO-14 has a $\delta^{18}O$ value (+5.25 ± 0.12 ‰) typical of the mantle (Figure 10). Sample DGO-14 has the lowest whole-rock Eu anomaly of the Bellsbank and Bobbejaan eclogite xenolith suite, which excludes the low-pressure crystallisation of plagioclase as being a process during the formation of its protolith and points toward a high-pressure igneous cumulate protolith. Alternatively, it might represent either a fragment of un-altered oceanic crust, or a fragment derived from depths within the ocean crust which correspond to temperatures outside of significant $\delta^{18}O$ fractionation conditions.

Gabbroic samples have lighter isotopic compositions than non-gabbroic samples which is consistent with temperature-dependant fractionation trends that result in heavier isotope compositions under low temperature alteration of basalt, and lighter isotope values under high temperature alteration of gabbro (Jacob and Foley, 1999; Barth *et al.*, 2001; Smart *et al.*, 2017). However, this cannot be taken as an absolute stratigraphic indicator within the inferred ocean crust protolith (Jacob *et al.*, 2003).

In summary, the Bellsbank and Bobbejaan Gabbroic eclogites are derived from the low-pressure fractional crystallisation of a mid-oceanic ridge type gabbro/basalt protolith (~1 GPa), followed by partial melting and subsequent subduction related processes. Proto-kimberlitic fluids caused cryptic metasomatism which likely occurred prior to entrainment. This is supported by major and trace element forward modelling, combined with $\delta^{18}O$ values dissimilar to that of the earth's mantle.

High-Mg and High-Ca samples have elevated HREE patterns more like that of an Archean picrite protolith, and a lack of distinct Eu anomalies combined with variable $\delta^{18}O$ values. Forward modelling of an Archean picrite differentiating at 1 GPa followed by kimberlite metasomatism provides evidence for a picritic protolith.

4.3 The redox state of the Bellsbank eclogites within the Kaapvaal craton mantle lithosphere

Mantle eclogites are a significant host for diamonds and an economically important diamond source rock (Stachel and Harris, 2008). While the links between mantle eclogite and diamond formation are intriguing yet partially-resolved, the oxygen fugacity of potential diamond host rocks and subsequent secondary processes affecting the CLM such as metasomatism are both important factors in diamond formation and preservation. (Creighton *et al.*, 2009; Smart *et al.*, 2012; Stachel and Luth, 2015; Stagno *et al.*, 2015). Oxygen fugacity can indicate both the carbon species involved in the formation of diamond and the suitability of eclogite as diamond host (Stagno *et al.*, 2015). The strong association between diamonds and mantle eclogite surrounds the transition from carbonate to diamond stable conditions at the correct redox conditions, specifically at around 1 log unit above the EMOD buffer curve (Stachel and Luth, 2015).

The Bellsbank and Bobbejaan eclogitic xenoliths equilibrated at pressures that correspond to depths between 102 and 188 km in the Kaapvaal SCLM, which is within the region of other Kaapvaal peridotites and eclogites (Table 5; Figure 8, 9). The distribution of eclogites in the Kaapvaal craton straddles both sides of the diamond-graphite stability line (Aulbach and Jacob, 2016). An eclogite composition vs. depth relation is evident as Gabbroic samples tend to have a marginally narrower range of equilibrium pressures compared to the non-gabbroic samples (3.4 to 5.6 GPa vs. 3.2 to 6.0 GPa). Moreover, High-Mg eclogites are derived from higher pressures than High-Ca samples (4.5 to 6.0 GPa vs. 3.2 to 4.5 GPa).

While most Bellsbank and Bobbejaan eclogite xenoliths fall along the pressure vs. fO_2 trend defined by Kaapvaal peridotites, horizonal variations in fO_2 related to changes in oxygen fugacity control whether samples fall under diamond/graphite or carbonate stability fields (Figure 9). The decreasing oxygen fugacity with increasing depth systematics shown here for the Bellsbank and Bobbejaan eclogite suite coincides with the only other published data for mantle eclogite xenoliths on the Kaapvaal craton from the Lace kimberlite (Aulbach *et al.*, 2017). However, lateral (Figure 9) variations to this trend suggest that the redox state within the Kaapvaal SCLM is not simply vertically and homogeneously stratified (Aulbach *et al.*, 2017).

4.3.1 Possible controls of oxygen fugacity heterogeneities on the diamond potential of cratonic mantle lithosphere

While Gabbroic eclogites from the Bellsbank and Bobbejaan kimberlite exhibit a wide range in depth of formation, they are concentrated (with exception to DGE-6 and DGO-12) between 3.6 to 4.8 GPa where they have a narrow range of fO_2 values (Δlog fO_2 from -3.2 to -1.8). Oxidising conditions at these depths are therefore higher than at greater depths (> 5 GPa). High-Mg eclogites occurring at pressures > 5 GPa however, have

the lowest fO_2 values (Δlog fO_2 from -4.2 to -3.8) of the entire suite. While most Gabbroic samples plot close to or within the depth vs. fO_2 fields shown for Kaapvaal craton peridotites, others (i.e., DGE-5, DGE-6, DGO-12 and DGO-15) do not. These samples have fO_2 values that are higher than Finsch peridotites at the same depth, which may result from metasomatism related oxidation. This oxidative metasomatism drives the eclogites out of the Finsch peridotite trend, out of diamond stable conditions, and toward the carbonate stability field (Figure 9).

High-Mg eclogites with the lowest fO_2 values (DGE-1, DGE-3) plot in diamond stable conditions (Table 5; Figure 8, 9), close to High-Mg eclogite samples from Lace kimberlite, and are in agreement with known oxygen fugacity depth trends observed in cratonic peridotites from Group I and Group II kimberlites (Woodland and Koch, 2003; Lazarov *et al*., 2009). Sample DGO-8 does not plot under diamond stable conditions as it equilibrated at depths greater than 150 km, however it does follow the fO_2 vs. depth trend evident for Kaapvaal peridotites, suggesting that it was not affected by oxidative metasomatism.

High-Ca eclogite DGE-2 derives from depths ~ 200 km, has one of the highest fO_2 values (Δlog fO_2 -2.4) and plots within the diamond stability field (Stagno *et al.*, 2015). This sample has a similar redox state to sample DGO-12 and DGE-6, which together are apart from the pressure vs. fO_2 systematics seen for the Kaapvaal CLM (Figure 9). Sample DGO-1 is the only Bellsbank and Bobbejaan eclogite xenolith that has pressure vs. fO_2 values that fall in carbonate stable conditions.

Metasomatism might be responsible for changes in the redox state of the Bellsbank and Bobbejaan mantle eclogites, as illustrated by the correlations between garnet $Fe^{3+}/\sum Fe$ and whole rock calculated Ce (ppm) content (Figure 16). While an increase in garnet $Fe^{3+}/\sum Fe$ with pressure is expected (Frost and McCammon, 2008), a correlation to indices of metasomatism is intriguing.

Whole-rock Sr (ppm) content for Bellsbank and Bobbejaan eclogites also shows a similar correlation to garnet $Fe^{3+}/\sum Fe$ (Figure 16). Samples with the highest Ce and Sr content have the highest garnet $Fe^{3+}/\sum Fe$ ratios, which is true for eclogite xenoliths from the Lace kimberlite (Kaapvaal craton). The same is true, to a lesser degree, for some Gabbroic eclogites from Voyager kimberlite (Slave craton).

Eclogite samples DGE-1, DGE-3, DGE-6, DGO-8 and DGO-12 (Figure 16) display characteristics of metasomatism (see section 4.1), which provides evidence for why Gabbroic samples DGE-6 and DGO-12 are distinct from the rest of the Gabbroic samples (Figure 9). Despite having more oxidised fO_2 values compared to the High-Mg samples at similar pressures (> 5 GPa), samples DGE-6 and DGO-12 have comparable Ce (ppm) as well as elevated garnet $Fe^{3+}/\sum Fe$ ratios. This highlights two possibilities, either that indices of cryptic metasomatic processes (i.e., containing elevated Ce, Sr) have a large effect on garnet $Fe^{3+}/\sum Fe$ ratios, or that similar processes at increased depths (> 200km) affect both garnet $Fe^{3+}/\sum Fe$ ratios and whole-rock LREE concentrations in a similar manner. Nevertheless, it is evident that metasomatism is more pronounced at pressures corresponding to depths ~200km within the Kaapvaal CLM.

The connection to changes in oxygen fugacity within the CLM becomes clearer when considering that samples DGE-6 and DGO-12 have fO_2 values ($\Delta\log fO_2$ = -2.6 and -2.1 respectively) that are significantly higher than those of Gabbroic eclogites ($\Delta\log fO_2$ from -4.2 to -3.8) equilibrated at similar depths. Gabbroic sample 362B from Voyager kimberlite (Slave craton) is similar in terms of pressure and $Fe^{3+}/\sum Fe$ content vs. Ce (ppm), however, is ~2 log units ($\Delta\log fO_2$) more reduced than the Bellsbank and Bobbejaan Gabbroic samples (Figure 16 A, E). While sample 362B showed no evidence for alteration (i.e., modal metasomatism), elevated LREE and Pb isotopic enrichments point toward cryptic and selective metasomatism (Smart *et al.*, 2017). It is important to note that the Voyageur eclogites demonstrate great heterogeneity in redox states without a clear trend in relation to equilibration pressure, which is owed to the variable redox

buffering capacity of recycled mafic components in the Slave cratonic mantle lithosphere (Smart *et al.*, 2017). Additionally, calculated fO_2 values are inherently dependant on P-T conditions and so given that the Voyageur eclogites originate from different depths to the Bellsbank suite, they are likely to have varying $Fe^{3+}/\sum Fe$ content.

High-Ca samples, showing no extensive evidence of metasomatism, equilibrate at low pressures (except DGE-2) between 3.2 and 4.5 GPa, and at more oxidised (Δlog fO_2 from -2.7 – -1.4) conditions. Sample DGE-2, however, has a fO_2 value (Δlog fO_2 = -2.4) higher than the Kaapvaal peridotite pressure vs. fO_2 array, but still falls within the diamond stability field. Sample DGE-2 does not show large enrichments in Ce and Sr relative to other High-Ca samples, however it does have the greatest ∑HREE content (16.09 ppm) of all High-Ca samples on the Kaapvaal craton for which values have been determined (Figure 15). Sample DGE-2 has similar fO_2 (Δlog fO_2 = -2.4 vs. -2.0) and REE patterns (Figure 7) to sample DGO-9, however, DGO-9 does not plot under diamond stable conditions (Figure 9). Therefore, the diamond potential of eclogite xenoliths - while being an important function of the redox state of the CLM they derive from - is still directly determined by the pressures at which they equilibrated.

High-Mg samples (DGE-1, DGE-3) plotting within the diamond stability field, despite having Ce values ~ 3 times greater than most Gabbroic samples, have the most reduced fO_2 values of the Bellsbank suite. Sample DGO-8 has elevated garnet $Fe^{3+}/\sum Fe$ ratios comparable to DGE-1 and DGE-3 (Figure 16) which correlates to whole-rock Ce content, however, has Sr values that are significantly lower (36.08 vs. 105.73 and 103.25 ppm respectively). At increased pressures (5 – 6 GPa) and associated garnet $Fe^{3+}/\sum Fe$ ratios, eclogites have increased Ce and Sr content, which has been shown to relate to metasomatism. It is unclear how this LREE enriched metasomatism relates to fO_2 because Gabbroic samples (DGE-6, DGO-12) appear more susceptible than High-Mg samples, which provides evidence for a protolith effect.

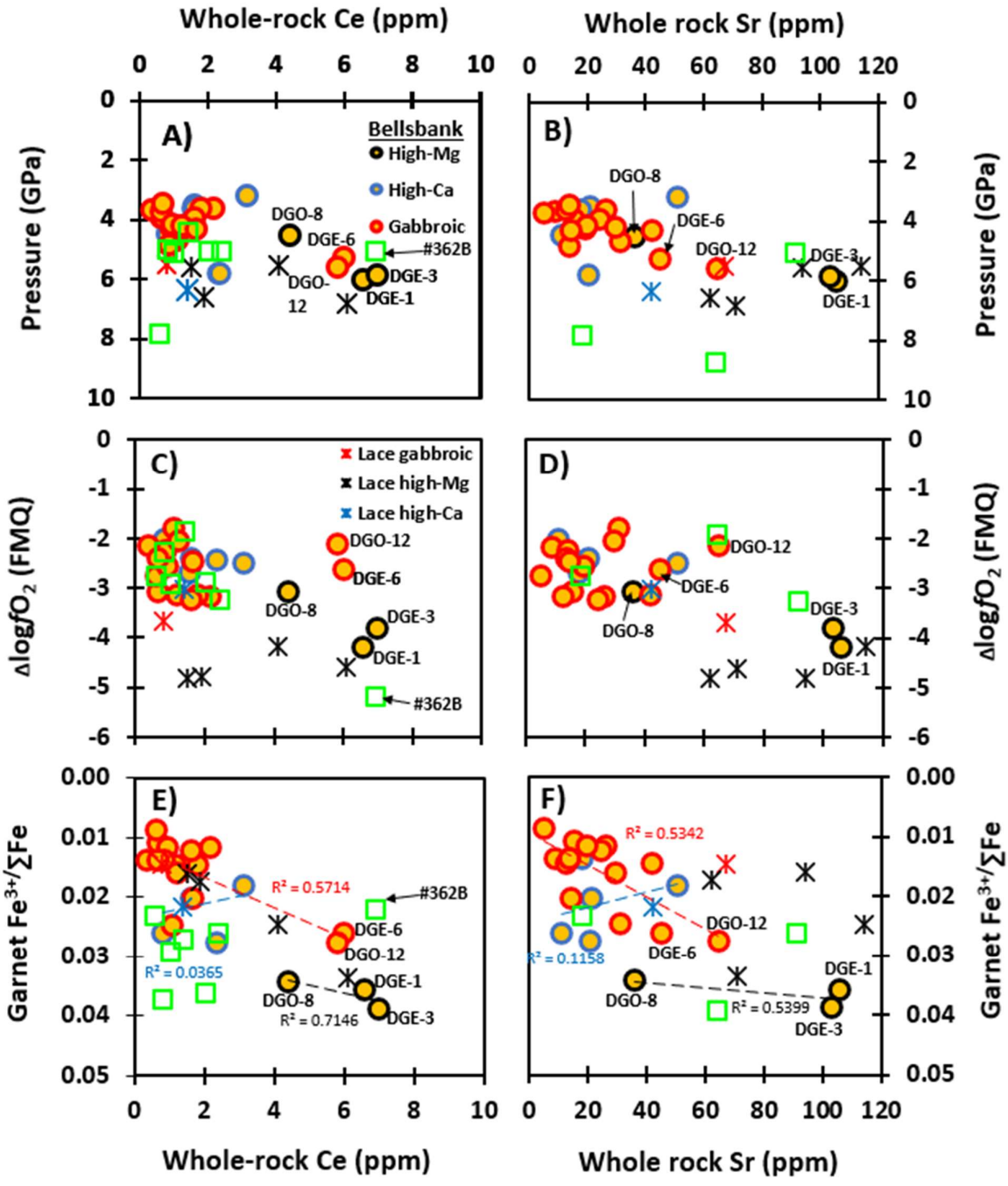

Figure 16. *Whole-rock Ce (ppm) and Sr (ppm) vs.* ***(a-b)*** *pressure,* ***(c-d)*** *logfO₂ and* ***(e-f)*** *Garnet $Fe^{3+}/\sum Fe$ for the Bellsbank and Bobbejaan Gabbroic (red circle), High-Mg (black circle) and High-Ca (blue circle) eclogites. Shown for comparison is Gabbroic (red star), High-Mg (black star) and High-Ca (blue star) eclogite xenoliths of Lace kimberlite from Aulbach et al. (2017). Slave gabbroic eclogite (green squares) data from the Slave craton from Smart et al. (2017).*

Eclogite xenoliths from Lace kimberlite in comparison (Figure 16) show minor change of fO_2 with respect to Ce and Sr content. There is a lack of available data on Gabbroic eclogites from Lace kimberlite to elucidate further. From Figure 7, samples DGE-6 and DGO-12 have the greatest LREE enrichments of all Gabbroic eclogites, and DGO-12 has HREE enrichments (relative to primitive mantle) ~4 times greater than the second most enriched sample DGO-7. Also evident is that DGO-12 is the only Gabbroic sample without a significant Eu anomaly (Eu* = 1.09) and contains the greatest amount of HREE's (Figure 15). Eclogite xenolith DGO-12 might represent a mischaracterised Gabbroic eclogite, or one which underwent less partial melt extraction than the rest of the Gabbroic samples during subduction subsequently becoming more enriched in LREE and oxidised by a metasomatic agent.

Studies on sub-calcic garnets from the Finsch kimberlite reveal a multi-stage depletion of the mantle, the first being around 3.6 Ga and the second around 2.5 Ga, which was succeeded by at least two metasomatic events (Lazarov *et al*., 2009). Crustal generation of the Kaapvaal craton occurred from ~ 3.6 Ga to 3.1 Ga, following which a period of craton assembly, including which was the amalgamation of the Western terrain with the eastern at 2.5 Ga (De Wit *et al.*, 1992; Griffin *et al.*, 2003). Metasomatism in the CLM of this part of the Kaapvaal at different depths is said to be related to different fluids or melts involved either at Karoo time volcanism (~ 180 Ma) or younger (< 95 Ma) plume related activity (Griffin *et al.*, 2003; references therein).

Increased melt related metasomatism in the lower part of the Kaapvaal mantle section results from the thinning of a depleted lherzolite layer from 150 to 200 km in depth (Griffin *et al.*, 2003). Kaapvaal peridotites derived from Group I kimberlites show garnet TiO_2 (wt.%) increases with depth (Figure 17), however, the same depth trend for Group II Finsch peridotites is less evident. Garnet TiO_2 content of these peridotites is largely variable around 200 km in depth. The lithosphere-asthenosphere boundary (LAB) on the western Kaapvaal craton where the Bellsbank and Bobbejaan

kimberlite is located, is 200 km deep. Most eclogite xenoliths are concentrated below the LAB in spatial association to a strongly melt-metasomatized zone (O'Reilly and Griffin, 2006). Indeed, garnet peridotites from the Kaapvaal have been found to have decreasing fO_2 values (Δlog fO_2 from -2 to -4.2) as depths increase from 120 to 210 km (Woodland and Koch, 2003).

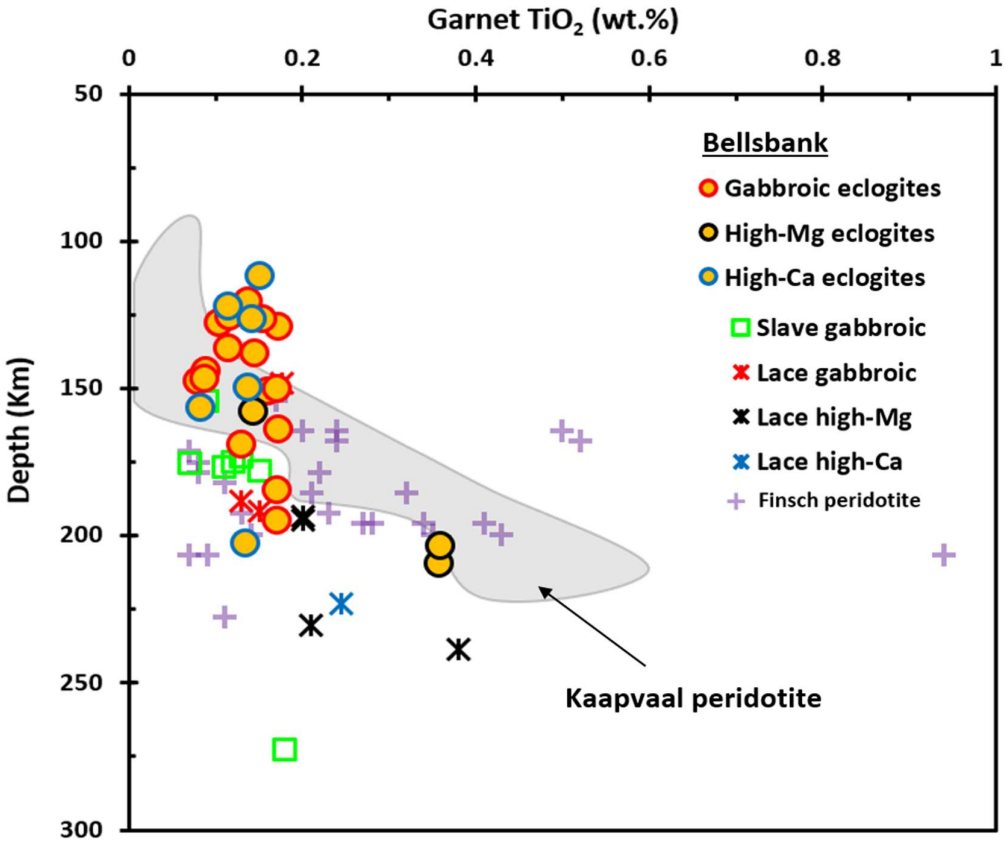

Figure 17. *Depth of formation vs. garnet TiO_2 (wt. %) for the Bellsbank and Bobbejaan Gabbroic (red circle), High-Mg (black circle) and High-Ca (blue circle) eclogites. Finsch peridotite data (purple symbols) from Lazarov et al. (2009). Various peridotite xenolith data compiled from Creighton et al., (2009), Woodland and Koch. (2003), and Hanger et al. (2014). Shown for comparison is gabbroic (red star), high-Mg (black star) and high-Ca (blue star) eclogite xenoliths of Lace kimberlite from Aulbach et al. (2017). Slave gabbroic eclogite (green squares) data from Smart et al. (2017).*

Oxygen fugacity data on Group I kimberlite derived peridotite xenoliths from the Kaapvaal (e.g. Creighton *et al.*, 2009; Hanger *et al.*, 2015) reveal a broad range in fO_2 values at a relatively small pressure interval (Figure 9) when compared to Group II Finsch peridotites. Thereby illustrating the heterogenous nature of the CLM. Oxidative metasomatic fluids related to

subduction-recycled volatiles at the base of the Kaapvaal cratonic LAB boundary, which are proposed to allow kimberlite melt migration through vein networks, is a possible agent by which the deeper eclogites from Bellsbank Group II kimberlite became oxidized closer to carbonate stable conditions (Tappe *et al.*, 2017; Yaxley *et al.*, 2017). This would be potentially destructive to any diamonds which may have crystallized with eclogite under diamond stable conditions (Shirey *et al.*, 2004; Stagno *et al.*, 2015)

Although depth compositional stratification within the Bellsbank eclogite suite exists, the effects of metasomatism on their oxygen fugacity and therefore diamond potential points towards deeper parts (~ 200 km) of the CLM near the LAB being more prone to highly oxidative proto-kimberlitic melt infiltration and migration than the shallower parts (3 – 4 GPa). The fact that High-Mg samples show LREE enrichment, come from the deepest part of the CLM, and have the most reduced redox state seemingly un-affected by oxidative metasomatism might relate to a sampling bias (n = 3). Given that High-Mg samples from Lace kimberlite are derived from similar depth vs. oxygen fugacity conditions (Figure 9), it is unlikely to be due to a sampling bias. Nevertheless, further research into the redox state of eclogite xenoliths from the Kaapvaal craton is necessary to further delineate known trends and better understand the diamond potential of the CLM.

CHAPTER FIVE – CONCLUSION

5. Conclusion

1. The Bellsbank and Bobbejaan mantle eclogites are classified as both Type I and II on a textural basis, and form a geochemically diverse suite of xenoliths spanning the A-B-C clinopyroxene and garnet classification schemes (Coleman *et al.*, 1965; Taylor *et al.*, 1990).

2. Eclogite xenoliths from the Bellsbank and Bobbejaan Group II kimberlite represent a suite of mantle xenoliths derived from temperatures (823 to 1259 °C) and pressures (3.2 to 6.0 GPa) corresponding to depths of ~ 100 to 200 km within the western Kaapvaal CLM.
3. Major and trace element analysis reveals that the Bellsbank eclogites consist of Gabbroic, High-Mg and High-Ca samples, each with unique isotopic signatures and residence within the Kaapvaal CLM. Gabbroic eclogites likely originate from an ocean gabbro undergoing partial melt extraction during subduction, followed by minor kimberlite cryptic metasomatism. High-Mg and High-Ca eclogites likely originate from basaltic-picritic ocean crust which was partially melted and subsequently cryptically metasomatized by kimberlite related fluids.
4. Gabbroic samples show the largest range in fO_2 values ($\Delta\log fO_2$ from -3.2 to -1.8) compared to High-Ca ($\Delta\log fO_2$ from -2.7 to -1.4) and High-Mg ($\Delta\log fO_2$ from -4.2 to -3.1) eclogites.
5. A total of 6 out of 24 eclogite xenoliths from the Bellsbank and Bobbejaan kimberlite plot under diamond stable conditions.
6. While the majority of the Bellsbank and Bobbejaan eclogite xenoliths plot along the known decreasing oxygen fugacity with depth trend seen for Kaapvaal peridotites, oxidative metasomatism at depths around 200 km cause eclogites to plot under carbonate stable conditions, which is potentially diamond destructive.

REFERENCES

Alt, J. C., Muehlenbachs, K. and Honnorez, J. (1986) 'An oxygen isotopic profile through the upper kilometer of the oceanic crust, DSDP Hole 504B', *Earth and Planetary Science Letters*, 80(3–4), pp. 217–229. doi: 10.1016/0012-821X(86)90106-8.

Anhaeusser, C. R. (2006) 'A reevaluation of Archean intracratonic terrane boundaries on the Kaapvaal Craton, South Africa: Collisional suture zones?', *Special Paper of the Geological Society of America*, 405(January 2006), pp. 193–210. doi: 10.1130/2006.2405(11).

Appleyard, C. M., Viljoen, K. S. and Dobbe, R. (2004) 'A study of eclogitic diamonds and their inclusions from the Finsch kimberlite pipe, South Africa', *Lithos*, 77(1-4 SPEC. ISS.), pp. 317–332. doi: 10.1016/j.lithos.2004.04.023.

Aulbach, S., Stachel, T., Creaser, R., Heaman, L., Shirey, S., Muehlenbachs, K., Eichenberg, D. and Harris. (2009) 'Sulphide survival and diamond genesis during formation and evolution of Archaean subcontinental lithosphere: A comparison between the Slave and Kaapvaal cratons', *Lithos*. Elsevier B.V., 112, pp. 747–757. doi: 10.1016/j.lithos.2009.03.048.

Aulbach, S., Jacob, D., Cartigny, P., Stern, R., Simonetti, S., Wörner, G. and Viljoen, K. (2017) 'Eclogite xenoliths from Orapa: Ocean crust recycling, mantle metasomatism and carbon cycling at the western Zimbabwe craton margin', *Geochimica et Cosmochimica Acta*, 213, pp. 574–592. doi: 10.1016/j.gca.2017.06.038.

Aulbach, S., Woodland, A., Vasilyev, P., Galvez, M. and Viljoen, K. (2017) 'Effects of low-pressure igneous processes and subduction on Fe3+/ΣFe and redox state of mantle eclogites from Lace (Kaapvaal craton)', *Earth and Planetary Science Letters*. Elsevier B.V., 474, pp. 283–295. doi: 10.1016/j.epsl.2017.06.030.

Aulbach, S., Gerdes, A. and Viljoen, K. S. (2016) 'Formation of

diamondiferous kyanite-eclogite in a subduction mélange', *Geochimica et Cosmochimica Acta*. Elsevier Ltd, 179, pp. 156–176. doi: 10.1016/j.gca.2016.01.038.

Aulbach, S. and Jacob, D. E. (2016) 'Major- and trace-elements in cratonic mantle eclogites and pyroxenites reveal heterogeneous sources and metamorphic processing of low-pressure protoliths', *Lithos*. Elsevier B.V., 262(14), pp. 586–605. doi: 10.1016/j.lithos.2016.07.026.

Aulbach, S. and Viljoen, K. S. (2015) 'Eclogite xenoliths from the Lace kimberlite, Kaapvaal craton: From convecting mantle source to palaeo-ocean floor and back', *Earth and Planetary Science Letters*. Elsevier B.V., 431, pp. 274–286. doi: 10.1016/j.epsl.2015.08.039.

Bach, W., Alt, J., Niu, Y., Humphris, S., Erzinger, J. and Dick, H. (2001) 'The geochemical consequences of late-stage low-grade alteration of lower ocean crust at the SW Indian Ridge: results from ODP Hole 735B (Leg 176)', *Geochimica et Cosmochimica Acta*. Pergamon, 65(19), pp. 3267–3287. doi: 10.1016/S0016-7037(01)00677-9.

Barth, M., Rudnick, R., Horn, I., McDonough, W., Spicuzza, M., Valley, J. and Haggerty, S. (2001) 'Geochemistry of xenolithic eclogites from West Africa, part I: A link between low MgO eclogites and archean crust formation', *Geochimica et Cosmochimica Acta*, 65(9), pp. 1499–1527. doi: 10.1016/S0016-7037(00)00626-8.

Barth, M., Rudnick, R., Horn, I., McDonough, W., Spicuzza, M., Valley, J. and Haggerty, S. (2002) 'Geochemistry of xenolithic eclogites from West Africa, part 2: Origins of the high MgO eclogites', *Geochimica et Cosmochimica Acta*, 66(24), pp. 4325–4345. doi: 10.1016/S0016-7037(02)01004-9.

Le Bas, M. J. (2000) 'IUGS reclassification of the high-Mg and picritic volcanic rocks', *Journal of Petrology*, 41(10), pp. 1467–1470. doi: 10.1093/petrology/41.10.1467.

Beard, B., Fraracci, K., Clayton, R., Mayeda, T., Snyder, G., Sobolev, N.

and Taylor, L.. (1996) ‘Petrography and geochemistry of eclogites from the Mir kimberlite, Yakutia, Russia’, *Contributions to Mineralogy and Petrology*, 125(4), pp. 293–310. doi: 10.1007/s004100050223.

Becker, M. and le Roex, A. P. (2006) ‘Geochemistry of South African on- and off-craton, group I and group II kimberlites: Petrogenesis and source region evolution’, *Journal of Petrology*, 47(4), pp. 673–703. doi: 10.1093/petrology/egi089.

Benoit, M., Polvé, M. and Ceuleneer, G. (1996) ‘Trace element and isotopic characterization of mafic cumulates in a fossil mantle diapir (Oman ophiolite)’, *Chemical Geology*, 134(1–3), pp. 199–214. doi: 10.1016/S0009-2541(96)00087-3.

Beyer, C., Frost, D. J. and Miyajima, N. (2015) ‘Experimental calibration of a garnet–clinopyroxene geobarometer for mantle eclogites’, *Contributions to Mineralogy and Petrology*, 169(2). doi: 10.1007/s00410-015-1113-z.

Bindeman, I., Kamenetsky, V., Palandri, J. and Vennemann, T. (2012) ‘Hydrogen and oxygen isotope behaviors during variable degrees of upper mantle melting: Example from the basaltic glasses from Macquarie Island’, *Chemical Geology*, 310–311, pp. 126–136. doi: https://doi.org/10.1016/j.chemgeo.2012.03.031.

Blundy, J. and Wood, B. (2003) ‘Partitioning of trace elements between crystals and melts’, *Earth and Planetary Science Letters*, 210(3–4), pp. 383–397. doi: 10.1016/S0012-821X(03)00129-8.

Boctor, N. Z. and Boyd, F. R. (1982) ‘Petrology of kimberlite from the DeBruyn and Martin mine, Bellsbank, South Africa.’, *American Mineralogist*, 67(9–10), pp. 917–925.

Bosch, J. (1971) ‘The petrology of some kimberlite occurences in the Barkly West District’, *Trans. Geol. Soc. S. Afr.*, 74, pp. 75–101.

Boyd, F. R. and Mertzman, S. (1987) ‘Composition and structure of the Kaapvaal lithosphere, southern Africa.’, *Magmatic Processes:*

Physicochemical Principles, pp. 13–24.

Canil, D. (2004) 'Mildly incompatible elements in peridotites and the origins of mantle lithosphere', *Lithos*, 77(1-4 SPEC. ISS.), pp. 375–393. doi: 10.1016/j.lithos.2004.04.014.

Caporuscio, F. A. and Smyth, J. R. (1990) 'Trace element crystal chemistry of mantle eclogites', *Contributions to Mineralogy and Petrology*, 105(5), pp. 550–561. doi: 10.1007/BF00302494.

Coleman, R., Lee, D., Beatty, L. and Brannock, W. (1965) 'Eclogites and eclogites: Their differences and similarities', *Bulletin of the Geological Society of America*, 76(5), pp. 483–508. doi: 10.1130/0016-7606(1965)76[483:EAETDA]2.0.CO;2.

Coogan, L., MacLeod, C., Dick, H., Edwards, S., Kvassnes, A., Natland, J., Robinson, P., Thompson, G. and O'Hara, M. (2001) 'Whole-rock geochemistry of gabbros from the Southwest Indian Ridge: Constraints on geochemical fractionations between the upper and lower oceanic crust and magma chamber processes at (very) slow-spreading ridges', *Chemical Geology*, 178(1–4), pp. 1–22. doi: 10.1016/S0009-2541(00)00424-1.

Coogan, L. A. and Dosso, S. E. (2016) 'Quantifying parental MORB trace element compositions from the eruptive products of realistic magma chambers: Parental EPR MORB are depleted', *Journal of Petrology*, 57(11–12), pp. 2105–2126. doi: 10.1093/petrology/egw059.

Cornell, D. H. (2017) 'The Namaqua-Natal Province', (March).

Creighton, S., Stachel, T., Matveev, S., Höfer, H., McCammon, C. and Luth, R. (2009) 'Oxidation of the Kaapvaal lithospheric mantle driven by metasomatism', *Contributions to Mineralogy and Petrology*, 157(4), pp. 491–504. doi: 10.1007/s00410-008-0348-3.

Crow, C. and Condie, K. C. (1988) 'Geochemistry and origin of late Archean volcanics from the ventersdorp supergroup, South Africa', *Precambrian Research*, 42(1–2), pp. 19–37. doi: 10.1016/0301-9268(88)90008-3.

Dawson, J. . B. (1984) ‘Contrasting types of upper-mantle metasomatism?’, *Kornprobst, J. (Ed.)*, Kimberlite(iii), pp. 282–331. doi: 10.1016/B978-0-444-42274-3.50030-5.

Eggins, S. M. (1993) ‘Origin and differentiation of picritic arc magmas, Ambae (Aoba), Vanuatu’, *Contributions to Mineralogy and Petrology*, 114(1), pp. 79–100. doi: 10.1007/BF00307867.

Eglington, B. M. and Armstrong, R. A. (2004) ‘The Kaapvaal Craton and adjacent orogens, southern Africa: A geochronological database and overview of the geological development of the craton’, *South African Journal of Geology*, 107(1–2), pp. 13–32. doi: 10.2113/107.1-2.13.

England, G., Rasmussen, B., McNaughton, N., Fletcher, I., Groves, D. and Krapez, B.. (2001) ‘SHRIMP U-Pb ages of diagenetic and hydrothermal xenotime from the Archaean Witwatersrand Supergroup of South Africa’, *Terra Nova*, 13(5), pp. 360–367. doi: 10.1046/j.1365-3121.2001.00363.x.

Eriksson, P., Altermann, W., Catunean, W., van der Merwe, R., Bumby, A.. (2001) ‘Major influences on the evolution of the 2.67-2.1 Ga Transvaal basin, Kaapvaal craton’, *Sedimentary Geology*, 141–142, pp. 205–231. doi: 10.1016/S0037-0738(01)00075-6.

Eriksson, P., Rigby, M., Bandopadhyay, P. and Steenkamp, N. (2011) ‘The Kaapvaal Craton, South Africa: No evidence for a supercontinental affinity prior to 2.0 Ga?’, *International Geology Review*, 53(11–12), pp. 1312–1330. doi: 10.1080/00206814.2010.527638.

Falloon, T., Green, D., Danyushevsky, L. and Faul, U. (1999) ‘Peridotite melting at 1·0 and 1·5 GPa: An experimental evaluation of techniques using diamond aggregates and mineral mixes for determination of near-solidus melts’, *Journal of Petrology*, 40(9), pp. 1343–1375. doi: 10.1093/petroj/40.9.1343.

Foley, S. F. (2011) ‘A reappraisal of redox melting in the earth’s mantle as a function of tectonic setting and time’, *Journal of Petrology*, 52(7–8), pp. 1363–1391. doi: 10.1093/petrology/egq061.

Frost, D. J. and McCammon, C. A. (2008) 'The Redox State of Earth's Mantle', *Annual Review of Earth and Planetary Sciences*, 36(1), pp. 389–420. doi: 10.1146/annurev.earth.36.031207.124322.

Gale, A., Dalton, C., Langmuir, C., Su, Y. and Schilling, J. (2013) 'The mean composition of ocean ridge basalts', *Geochemistry, Geophysics, Geosystems*, 14(3), pp. 489–518. doi: 10.1029/2012GC004334.

Ghiorso, M., Hirschmann, M., Reiners, P. and Kress, V. (2002) 'The pMELTS: A revision of MELTS for improved calculation of phase relations and major element partitioning related to partial melting of the mantle to 3 GPa', *Geochemistry, Geophysics, Geosystems*, 3(5), pp. 1–35. doi: 10.1029/2001gc000217.

Gibson, S. A., Malarkey, J. and Day, J. A. (2008) 'Melt depletion and enrichment beneath the Western Kaapvaal craton: Evidence from Finsch peridotite xenoliths', *Journal of Petrology*, 49(10), pp. 1817–1852. doi: 10.1093/petrology/egn048.

Gonzaga, R., Lowry, D., Jacob, D., LeRoex, A., Schulze, D. and Menzies, M. (2010) 'Eclogites and garnet pyroxenites: Similarities and differences', *Journal of Volcanology and Geothermal Research*. Elsevier B.V., 190(1–2), pp. 235–247. doi: 10.1016/j.jvolgeores.2009.08.022.

Gréau, Y., Huang, J., Griffin, W., Renac, C., Alard, O. and O'Reilly, S. (2011) 'Type I eclogites from Roberts Victor kimberlites: Products of extensive mantle metasomatism', *Geochimica et Cosmochimica Acta*, 75(22), pp. 6927–6954. doi: 10.1016/j.gca.2011.08.035.

Green, D. H. and Ringwood, A. E. (1967) 'The genesis of basaltic magmas', *Contributions to Mineralogy and Petrology*, 15(2), pp. 103–190. doi: 10.1007/BF00372052.

Green, T., Blundy, J., Adam, J. and Yaxley, G. (2000) 'SIMS determination of trace element partition coefficients between garnet, clinopyroxene and hydrous basaltic liquids at 2-7.5 GPa and 1080-1200°C', *Lithos*, 53(3–4), pp. 165–187. doi: 10.1016/S0024-4937(00)00023-2.

Griffin, W. (2003) ‘The evolution of lithospheric mantle beneath the Kalahari Craton and its margins’, *Lithos*, 71(2–4), pp. 215–241. doi: 10.1016/j.lithos.2003.07.006.

Griffin, W., O’Reilly, S., Abe, N., Aulbach, S., Davies, R., Pearson, N., Doyle, B. and Kivi, K. (2003) ‘The origin and evolution of Archean lithospheric mantle’, *Precambrian Research*, 127(1–3), pp. 19–41. doi: 10.1016/S0301-9268(03)00180-3.

Griffin, W. L. and O’Reilly, S. Y. (2006) ‘Cratonic lithospheric mantle : Is anything subducted ?’, *Episodes*, 30(1), pp. 43–53. doi: 10.18814/epiiugs/2007/v30i1/006.

Griffin, W. L. and O’Reilly, S. Y. (2007) ‘Cratonic lithospheric mantle: Is anything subducted?’, *Episodes*, 30(1), pp. 43–53. doi: 10.18814/epiiugs/2007/v30i1/006.

Gurney, J. and Kirkley, M. B. (1996) ‘Kimberlite dyke mining in South Africa’, *Africa Geoscience Review*, 3, pp. 191–201.

Hanger, B., Yaxley, G., Berry, A. and Kamenetsky, V. (2015) ‘Relationships between oxygen fugacity and metasomatism in the Kaapvaal subcratonic mantle, represented by garnet peridotite xenoliths in the Wesselton kimberlite, South Africa’, *Lithos*. Elsevier B.V., 212–215, pp. 443–452. doi: 10.1016/j.lithos.2014.09.030.

Harris, C. and Vogeli, J. (2010) ‘Oxygen isotope composition of garnet in the Peninsula Granite, Cape Granite Suite, South Africa: Constraints on melting and emplacement mechanisms’, *South African Journal of Geology*, 113(4), pp. 401–412. doi: 10.2113/gssajg.113.4.401.

Harte, B. and Kirkley, M. B. (1997) ‘Partitioning of trace elements between clinopyroxene and garnet: data from mantle eclogites’, *Chemical Geology*, 136(1–2), pp. 1–24. doi: 10.1016/S0009-2541(96)00127-1.

Hasterok, D. and Chapman, D. S. (2011) ‘Heat production and geotherms for the continental lithosphere’, *Earth and Planetary Science Letters*.

Elsevier B.V., 307(1–2), pp. 59–70. doi: 10.1016/j.epsl.2011.04.034.

Helmstaedt, H. and Doig, R. (1975) 'Eclogite nodules from kimberlite pipes of the Colorado plateau-samples of subducted Franciscan-type oceanic lithosphere', *Physics and Chemistry of the Earth*, 9(C), pp. 95–111. doi: 10.1016/0079-1946(75)90010-5.

Huang, J., Xiang, Y., An, Y., Griffin, W., Gréau, Y., Xie, L., Pearson, N., Yu, H. and O'Reilly, S. (2016) 'Magnesium and oxygen isotopes in Roberts Victor eclogites', *Chemical Geology*, 438, pp. 73–83. doi: 10.1016/j.chemgeo.2016.05.030.

Ireland, T. R., Rudnick, R. L. and Spetsius, Z. (1994) 'Trace elements in diamond inclusions from eclogites reveal link to Archean granites', *Earth and Planetary Science Letters*, 128(3–4), pp. 199–213. doi: 10.1016/0012-821X(94)90145-7.

Jacob, D., Jagoutz, E., Lowry, D., Mattey, D. and Kudrjavtseva, G.. (1994) 'Diamondiferous eclogites from Siberia: Remnants of Archean oceanic crust', *Geochimica et Cosmochimica Acta*, 58(23), pp. 5191–5207. doi: 10.1016/0016-7037(94)90304-2.

Jacob, D. E. (2004) 'Nature and origin of eclogite xenoliths from kimberlites', *Lithos*, 77(1-4 SPEC. ISS.), pp. 295–316. doi: 10.1016/j.lithos.2004.03.038.

Jacob, D. E. and Foley, S. F. (1999) 'Evidence for Archean ocean crust with low high field strength element signature from diamondiferous eclogite xenoliths', *Developments in Crop Science*, 24(C), pp. 317–336. doi: 10.1016/S0419-0254(99)80017-2.

Jacob, D. E., Schmickler, B. and Schulze, D. J. (2003) 'Trace element geochemistry of coesite-bearing eclogites from the Roberts Victor kimberlite, Kaapvaal craton', *Lithos*, 71(2–4), pp. 337–351. doi: 10.1016/S0024-4937(03)00120-8.

Jacob, D. E., Viljoen, K. S. and Grassineau, N. V. (2009) 'Eclogite xenoliths from Kimberley, South Africa - A case study of mantle metasomatism in

eclogites', *Lithos*. Elsevier B.V., 112, pp. 1002–1013. doi: 10.1016/j.lithos.2009.03.034.

Jacobs, J. and Thomas, R. J. (1996) 'Pan-African rejuvenation of the c. 1.1 Ga Natal Metamorphic Province(South Africa): K-Ar muscovite and titanite fission track evidence', *Journal of the Geological Society*, 153(6), pp. 971–978. doi: 10.1144/gsjgs.153.6.0971.

Jerde, E., Taylor, L., Crozaz, G. and Sobolev, N. (1993) 'Exsolution of garnet within clinopyroxene of mantle eclogites: major- and trace-element chemistry', *Contributions to Mineralogy and Petrology*, 114(2), pp. 148–159. doi: 10.1007/BF00307752.

Jochum, K., Weis, U., Stoll, B., Kuzmin, D., Yang, Q., Raczek, I., Jacob, D., Stracke, A., Birbaum, K., Frick, D., Günther, D. and Enzweiler, J. (2011) 'Determination of reference values for NIST SRM 610-617 glasses following ISO guidelines', *Geostandards and Geoanalytical Research*, 35(4), pp. 397–429. doi: 10.1111/j.1751-908X.2011.00120.x.

Jochum, K., Weis, U., Schwager, B., Stoll, B., Wilson, S., Haug, G., Andreae, M. and Enzweiler, J. (2016) 'Reference Values Following ISO Guidelines for Frequently Requested Rock Reference Materials', *Geostandards and Geoanalytical Research*, 40(3), pp. 333–350. doi: 10.1111/j.1751-908X.2015.00392.x.

Johnson, M., Van Vuuren, C., Hegenberger, W., Key, R. and Show, U. (1996) 'Stratigraphy of the Karoo Supergroup in southern Africa: an overview', *Journal of African Earth Sciences*, 23(1), pp. 3–15. doi: https://doi.org/10.1016/S0899-5362(96)00048-6.

Korolev, N., Melnik, A., Li, X. and Skublov, S. (2018) 'The oxygen isotope composition of mantle eclogites as a proxy of their origin and evolution: A review', *Earth-Science Reviews*. Elsevier, 185(May), pp. 288–300. doi: 10.1016/j.earscirev.2018.06.007.

Kröner, A., Hegner, E., Wendt, J. and Byerly, G. (1996) 'The oldest part of the Barberton granitoid-greenstone terrain, South Africa: Evidence for crust

formation between 3.5 and 3.7 Ga', *Precambrian Research*, 78(1-3 SPEC. ISS.), pp. 105–124. doi: 10.1016/0301-9268(95)00072-0.

Lazarov, M., Brey, G. P. and Weyer, S. (2009) 'Time steps of depletion and enrichment in the Kaapvaal craton as recorded by subcalcic garnets from Finsch (SA)', *Earth and Planetary Science Letters*. Elsevier B.V., 279(1–2), pp. 1–10. doi: 10.1016/j.epsl.2008.12.015.

Lazarov, M., Brey, G. P. and Weyer, S. (2012) 'Evolution of the South African mantle - A case study of garnet peridotites from the Finsch diamond mine (Kaapvaal craton); part 1: Inter-mineral trace element and isotopic equilibrium', *Lithos*. Elsevier B.V., 154, pp. 193–209. doi: 10.1016/j.lithos.2012.07.007.

Lazarov, M., Woodland, A. B. and Brey, G. P. (2009) 'Thermal state and redox conditions of the Kaapvaal mantle: A study of xenoliths from the Finsch mine, South Africa', *Lithos*. Elsevier B.V., 112, pp. 913–923. doi: 10.1016/j.lithos.2009.03.035.

Lee, C., Luffi, P. and Chin, E. (2011) 'Building and Destroying Continental Mantle', *Annual Review of Earth and Planetary Sciences*. Elsevier B.V., 39(1), pp. 59–90. doi: 10.1146/annurev-earth-040610-133505.

Leuthold, J., Lissenberg, C., O'Driscoll, B., Karakas, O., Falloon, T., Klimentyeva, D. and Ulmer, P.. (2018) 'Partial melting of lower oceanic crust gabbro: Constraints from poikilitic clinopyroxene primocrysts', *Frontiers in Earth Science*, 6(March). doi: 10.3389/feart.2018.00015.

MacGregor, I. D. and Carter, J. L. (1970) 'The chemistry of clinopyroxenes and garnets of eclogite and peridotite xenoliths from the Roberts Victor mine, South Africa', *Physics of the Earth and Planetary Interiors*, 3(C), pp. 391–397. doi: 10.1016/0031-9201(70)90081-6.

MacGregor, I. D. and Manton, W. I. (1986) 'Roberts victor eclogites: Ancient oceanic crust', *Journal of Geophysical Research*, 91(B14), p. 14063. doi: 10.1029/jb091ib14p14063.

Mattey, D., Lowry, D. and Macpherson, C. (1994) 'Oxygen isotope composition of mantle peridotite', *Earth and Planetary Science Letters*, 128(3–4), pp. 231–241. doi: 10.1016/0012-821X(94)90147-3.

McCandless, T. E. and Gurney, J. J. (1989) 'Sodium in garnet and potassium in clinopyroxene: criteria for classifying mantle eclogites', *Kimberlites and Related rocks*, (August), pp. 827–832.

McCourt, S., Armstrong, R., Grantham, G. and Thomas, R. (2006) 'Geology and evolution of the Natal belt, South Africa', *Journal of African Earth Sciences*, 46(1–2), pp. 71–92. doi: 10.1016/j.jafrearsci.2006.01.013.

McDonough, W. F. and Sun, S. (1995) 'Chemical Evolution of the MantleThe composition of the Earth', *Chemical Geology*, 120(3), pp. 223–253. doi: http://dx.doi.org/10.1016/0009-2541(94)00140-4.

McKay, M., Weislogel, A., Fildani, A., Brunt, R., Hodgson, D. and Flint, S. (2015) 'U-PB zircon tuff geochronology from the Karoo Basin, South Africa: implications of zircon recycling on stratigraphic age controls', *International Geology Review*. Taylor & Francis, 57(4), pp. 393–410. doi: 10.1080/00206814.2015.1008592.

Mckenzie, D. and Bickle, M. J. (1988) 'The volume and composition of melt generated by extension of the lithosphere', *Journal of Petrology*, 29(3), pp. 625–679. doi: 10.1093/petrology/29.3.625.

McLean, H., Banas, A., Creighton, S., Whiteford, S., Luth, R. and Stachel, T. (2007) 'Garnet xenocrysts from the Diavik mine, NWT, Canada: Composition, color, and paragenesis', *Canadian Mineralogist*, 45(5), pp. 1131–1145. doi: 10.2113/gscanmin.45.5.1131.

Mitchell, R. (2006) 'Potassic magmas derived from metasomatized lithospheric mantle: Nomenclature and relevance to exploration for diamond-bearing rocks', *Journal of the Geological Society of India*, 67, pp. 317–327.

Mitchell, R. H. (1995) *Kimberlites, Orangeites, and Related Rocks*. 1st edn.

Springer US. doi: 10.1007/978-1-4615-1993-5.

Moen, H. F. G. (1999) 'The Kheis Tectonic Subprovince, southern Africa: A lithostratigraphic perspective', *South African Journal of Geology*, 102(1), pp. 27–42.

O'Hara, M. J., Saunders, M. J. and Mercy, E. L. P. P. (1975) 'Garnet-peridotite, primary ultrabasic magma and eclogite; Interpretation of upper mantle processes in kimberlite', *Physics and Chemistry of the Earth*, 9(C), pp. 571–604. doi: 10.1016/0079-1946(75)90040-3.

O'Reilly, S. Y. and Griffin, W. L. (2006) 'Imaging global chemical and thermal heterogeneity in the subcontinental lithospheric mantle with garnets and xenoliths: Geophysical implications', *Tectonophysics*, 416(1–2), pp. 289–309. doi: 10.1016/j.tecto.2005.11.014.

O'Reilly, S. Y., & Griffin, W. L. (2013). Mantle metasomatism. In D. E. Harlov, & H. Austrheim (Eds.), *Metasomatism and the chemical transformation of rock: the role of fluids in terrestrial and extraterrestrial processes* (pp. 471-533). (Lecture notes in earth system sciences). Heidelberg;London: Springer, Springer Nature. https://doi.org/10.1007/978-3-642-28394-9_12

Ongley, J. S., Basu, A. R. and Kurtis Kyser, T. (1987) 'Oxygen isotopes in coexisting garnets, clinopyroxenes and phlogopites of Roberts Victor eclogites: implications for petrogenesis and mantle metasomatism', *Earth and Planetary Science Letters*, 83(1–4), pp. 80–84. doi: 10.1016/0012-821X(87)90052-5.

Paton, C., Woodhead, J., Hellstrom, J., Hergt, J., Greig, A. and Maas, R. (2010) 'Improved laser ablation U-Pb zircon geochronology through robust downhole fractionation correction', *Geochemistry, Geophysics, Geosystems*, 11(3). doi: 10.1029/2009GC002618.

Paton, C., Hellstrom, J., Paul, B., Woodhead, J. and Hergt, J. (2011) 'Iolite: Freeware for the visualisation and processing of mass spectrometric data', *Journal of Analytical Atomic Spectrometry*, 26(12), pp. 2508–2518. doi:

10.1039/c1ja10172b.

Purwin, H., Lauterbach, S., Brey, G., Woodland, A. and Kleebe, H. (2013) 'An experimental study of the Fe oxidation states in garnet and clinopyroxene as a function of temperature in the system CaO-FeO-Fe2O3-MgO-Al2O3-SiO2: Implications for garnet-clinopyroxene geothermometry', *Contributions to Mineralogy and Petrology*, 165(4), pp. 623–639. doi: 10.1007/s00410-012-0827-4.

Radu, I., Harris, C., Moine, B., Costin, G. and Cottin, J. (2019) 'Subduction relics in the subcontinental lithospheric mantle evidence from variation in the δ 18 O value of eclogite xenoliths from the Kaapvaal craton', *Contributions to Mineralogy and Petrology*. Springer Berlin Heidelberg, 174(3), pp. 1–24. doi: 10.1007/s00410-019-1552-z.

Ravna, E. J. (2000) 'The garnet–clinopyroxene Fe2+–Mg geothermometer: an updated calibration', *J. metamorphic Geol*, (18), pp. 211–219.

Riches, A., Ickert, R., Pearson, D., Stern, R., Jackson, S., Ishikawa, A., Kjarsgaard, B. and Gurney, J. (2016a) 'In situ oxygen-isotope, major-, and trace-element constraints on the metasomatic modification and crustal origin of a diamondiferous eclogite from Roberts Victor, Kaapvaal Craton', *Geochimica et Cosmochimica Acta*. Elsevier Ltd, 174(November 2017), pp. 345–359. doi: 10.1016/j.gca.2015.11.028.

le Roex, A. P. (2003) 'Petrogenesis of Group I Kimberlites from Kimberley, South Africa: Evidence from Bulk-rock Geochemistry', *Journal of Petrology*, 44(12), pp. 2261–2286. doi: 10.1093/petrology/egg077.

Schmickler, B., Jacob, D. E. and Foley, S. F. (2004) 'Eclogite xenoliths from the Kuruman kimberlites, South Africa: Geochemical fingerprinting of deep subduction and cumulate processes', *Lithos*, 75(1–2), pp. 173–207. doi: 10.1016/j.lithos.2003.12.012.

Schmidberger, S., Heaman, L., Simonetti, A., Creaser, R., Cookenboo, H. (2005) 'Formation of Paleoproterozoic eclogitic mantle, Slave Province (Canada): Insights from in-situ Hf and U-Pb isotopic analyses of mantle

zircons', *Earth and Planetary Science Letters*, 240(3–4), pp. 621–633. doi: 10.1016/j.epsl.2005.09.057.

Schmidberger, S. S. and Francis, D. (2001) 'Constraints on the Trace Element Composition of the Archean Mantle Root beneath Somerset Island, Arctic Canada', *Journal of Petrology*, 42(6), pp. 1095–1117. doi: 10.1093/petrology/42.6.1095.

Schmitz, M., Bowring, S., de Wit, M. and Gartz, V. (2004) 'Subduction and terrane collision stabilize the western Kaapvaal craton tectosphere 2.9 billion years ago', *Earth and Planetary Science Letters*, 222(2), pp. 363–376. doi: 10.1016/j.epsl.2004.03.036.

Schulze, D. J. (1989) 'Constraints on the abundance of eclogite in the upper mantle', *Journal of Geophysical Research: Solid Earth*, 94(B4), pp. 4205–4212. doi: 10.1029/JB094iB04p04205.

Shervais, J., Taylor, L., Lugmair, G., Clayton, R., Mayeda, T., Korotev, R. (1988) 'Early Proterozoic oceanic crust and the evolution of subcontinental mantle: Eclogites and related rocks from southern Africa', *Bulletin of the Geological Society of America*, 100(3), pp. 411–423. doi: 10.1130/0016-7606(1988)100<0411:EPOCAT>2.3.CO;2.

Shirey, S. B., Richardson, S. H. and Harris, J. W. (2004) 'Integrated models of diamond formation and craton evolution', *Lithos*, 77(1-4 SPEC. ISS.), pp. 923–944. doi: 10.1016/j.lithos.2004.04.018.

Shu, Q. *et al.* (2014) 'Mantle eclogites and garnet pyroxenites - the meaning of two-point isochrons, Sm-Nd and Lu-Hf closure temperatures and the cooling of the subcratonic mantle', *Earth and Planetary Science Letters*. Elsevier B.V., 389, pp. 143–154. doi: 10.1016/j.epsl.2013.12.028.

Shu, Q., Brey, G., Gerdes, A. and Hoefer, H. (2016) 'Kyanite/corundum eclogites from the Kaapvaal Craton: subducted troctolites and layered gabbros from the Mid- to Early Archean', *Contributions to Mineralogy and Petrology*. Springer Berlin Heidelberg, 171(2), pp. 1–24. doi: 10.1007/s00410-015-1225-5.

Simon, N., Carlson, R., Pearson, D. and Davies, G. (2007) 'The origin and evolution of the Kaapvaal Cratonic Lithospheric Mantle', *Journal of Petrology*, 48(3), pp. 589–625. doi: 10.1093/petrology/egl074.

Skinner, C. P. (1989) 'The petrology of peridotite xenoliths from the Finsch kimberlite, South Africa', *South African Journal of Geology*, 92(3), pp. 197–206.

Smart, K., Heaman, L., Chacko, T., Simonetti, A., Kopylova, M., Mah, D. and Daniels, D. (2009) 'The origin of high-MgO diamond eclogites from the Jericho Kimberlite, Canada', *Earth and Planetary Science Letters*. Elsevier B.V., 284(3–4), pp. 527–537. doi: 10.1016/j.epsl.2009.05.020.

Smart, K., Chacko, T., Stachel, T., Tappe, S., Stern, R., Ickert, R. (2012) 'Eclogite formation beneath the northern Slave craton constrained by diamond inclusions: Oceanic lithosphere origin without a crustal signature', *Earth and Planetary Science Letters*. Elsevier B.V., 319–320, pp. 165–177. doi: 10.1016/j.epsl.2011.12.032.

Smart, K., Chacko, T., Simonetti, A., Sharp, Z. and Heaman, L. (2014) 'A record of paleoproterozoic subduction preserved in the northern slave cratonicmantle: Sr-pb-o isotope and trace-element investigations of eclogite xenoliths from the jericho and muskox kimberlites', *Journal of Petrology*, 55(3), pp. 549–583. doi: 10.1093/petrology/egt077.

Smart, K., Tappe, S., Simonetti, A., Simonetti, S., Woodland, A. and Harris, C. (2017) 'Tectonic significance and redox state of Paleoproterozoic eclogite and pyroxenite components in the Slave cratonic mantle lithosphere, Voyageur kimberlite, Arctic Canada', *Chemical Geology*. Elsevier B.V., 455, pp. 98–119. doi: 10.1016/j.chemgeo.2016.10.014.

Smith, C.B., Allsop, H.L., Kramers, J.D., Hutchinson, G., & Roddick, J.C. (1985) 'Emplacement ages of Jurassic-Cretaceous South African kimberlites by the Rb-Sr method on phlogopite and whole-rock samples.', *Transactions of the Geological Society of South Africa*, 88(2), pp. 249–266.

Smyth, J. R. and Caporuscio, F. A. (1984) 'Petrology of a suite of eclogite

inclusions from the Bobbejaan kimberlite, II. Primary phase compositions and origin.', *The Mantle and Crust-Mantle Relationships*, II(Kimberlites), pp. 121–132.

Stachel, T. and Harris, J. W. (2008) 'The origin of cratonic diamonds - Constraints from mineral inclusions', *Ore Geology Reviews*, 34(1–2), pp. 5–32. doi: 10.1016/j.oregeorev.2007.05.002.

Stachel, T. and Harris, J. W. (2009) 'Formation of diamond in the Earth's mantle', *Journal of Physics Condensed Matter*, 21(36). doi: 10.1088/0953-8984/21/36/364206.

Stachel, T. and Luth, R. W. (2015) 'Diamond formation - Where, when and how?', *Lithos*. Elsevier B.V., 220–223, pp. 200–220. doi: 10.1016/j.lithos.2015.01.028.

Stagno, V., Frost, D., McCammon, C., Mohseni, H. and Fei, Y. (2015) 'The oxygen fugacity at which graphite or diamond forms from carbonate-bearing melts in eclogitic rocks', *Contributions to Mineralogy and Petrology*, 169(2). doi: 10.1007/s00410-015-1111-1.

Tappe, S., Smart, K., Pearson, D., Steenfelt, A. and Simonetti, A. (2011) 'Craton formation in Late Archean subduction zones revealed by first Greenland eclogites', *Geology*, 39(12), pp. 1103–1106. doi: 10.1130/G32348.1.

Tappe, S., Romer, R., Stracke, A., Steenfelt, A., Smart, K., Muehlenbachs, K. and Torsvik, T. (2017) 'Sources and mobility of carbonate melts beneath cratons, with implications for deep carbon cycling, metasomatism and rift initiation', *Earth and Planetary Science Letters*. Elsevier B.V., 466(May), pp. 152–167. doi: 10.1016/j.epsl.2017.03.011.

Tappe, S., Smart, KA., Torsvik, TH., Massuyeau, M., de Wit, MCJ. (2018) Geodynamics of kimberlites on a cooling Earth: Clues to plate tectonic evolution and deep volatile cycles. Earth and Planetary Science Letters 484:1-14. doi: 10.1016/j.epsl.2017.12.013.

Neal, C., Taylor, L., Davidson, J., Holden, P., Halliday, A., Nixon, P., Paces, J., Clayton, R. and Mayeda, T. (1990) 'Eclogites with Oceanic Crustal and Mantle Signatures from the Bellsbank Kimberlite, South Africa, Part II: Sr, Nd, and O isotpe geochemistry', *Journal of Geology*, 99(5), pp. 362–379. doi: 10.1086/629334.

Taylor, L. A. and Neal, C. R. (1993) 'Trace-Element Crystal-Chemistry of Mantle Eclogites - Comment', *Contributions to Mineralogy and Petrology*, pp. 280–284.

Tuff, J. and Gibson, S. A. (2007) 'Trace-element partitioning between garnet, clinopyroxene and Fe-rich picritic melts at 3 to 7 GPa', *Contributions to Mineralogy and Petrology*, 153(4), pp. 369–387. doi: 10.1007/s00410-006-0152-x.

Vasilyev, P. (2016) *The oxidation state of deeply subducted, altered oceanic crust: an experimental study and the evidence from natural samples*. Available at: https://digitalcollections.anu.edu.au/handle/1885/101931%0Ahttps://digitalcollections.anu.edu.au/handle/1885/101931%0Ahttps://drive.google.com/open?id=0B0fTxDBXtHZMZkpiZE0zenY1Wmc.

Viljoen, K. S. (1995) 'Graphite- and diamond-bearing eclogite xenoliths from the Bellsbank kimberlites, Northern Cape, South Africa', *Contributions to Mineralogy and Petrology*, 121(4), pp. 414–423. doi: 10.1007/s004100050106.

Viljoen, K. S., Schulze, D. J. and Quadling, A. G. (2005) 'Contrasting Group I and Group II eclogite xenolith petrogenesis: Petrological, trace element and isotopic evidence from eclogite, garnet-websterite and alkremite xenoliths in the Kaalvallei Kimberlite, South Africa', *Journal of Petrology*, 46(10), pp. 2059–2090. doi: 10.1093/petrology/egi047.

Viljoen, K. S., Smith, C. B. and Sharp, Z. D. (1996) 'Stable and radiogenic isotope study of eclogite xenoliths from the Orapa kimberlite, Botswana',

Chemical Geology, 131(1–4), pp. 235–255. doi: 10.1016/0009-2541(96)00018-6.

Wang, T., Gao, S., Dai, Y., Yang, Q. and Liu, K. (2019) 'Lithospheric Structure and Evolution of Southern Africa: Constraints From Joint Inversion of Rayleigh Wave Dispersion and Receiver Functions', *Geochemistry, Geophysics, Geosystems*. doi: 10.1029/2019GC008259.

de Wit, M., Roering, C., Hart, R., Armstrong, R., de Ronde, C., Cornel, E., Green, R., Tredoux, M., Peberdy, E., Roger, A. (1992) 'Formation of an Archaean continent', *Nature*, 357(6379), pp. 553–562. doi: 10.1038/357553a0.

Woodland, A. B. and Koch, M. (2003) 'Variation in oxygen fugacity with depth in the upper mantle beneath the Kaapvaal craton, Southern Africa', *Earth and Planetary Science Letters*, 214(1–2), pp. 295–310. doi: 10.1016/S0012-821X(03)00379-0.

Yaxley, G., Berry, A., Rosenthal, A., Woodland, A. and Paterson, D. (2017) 'Redox preconditioning deep cratonic lithosphere for kimberlite genesis - Evidence from the central Slave Craton', *Scientific Reports*. Springer US, 7(1), pp. 1–10. doi: 10.1038/s41598-017-00049-3.

Yaxley, G. M. and Sobolev, A. V. (2007) 'High-pressure partial melting of gabbro and its role in the Hawaiian magma source', *Contributions to Mineralogy and Petrology*, 154(4), pp. 371–383. doi: 10.1007/s00410-007-0198-4.

Zeh, A., Ovtcharova, M., Wilson, A. and Schaltegger, U. (2015) 'The Bushveld Complex was emplaced and cooled in less than one million years – results of zirconology, and geotectonic implications', *Earth and Planetary Science Letters*, 418. doi: 10.1016/j.epsl.2015.02.035.

APPENDICES

7.1 Appendix Figures

Appendix Figure 1. *Photograph of hand sample DGE-1*

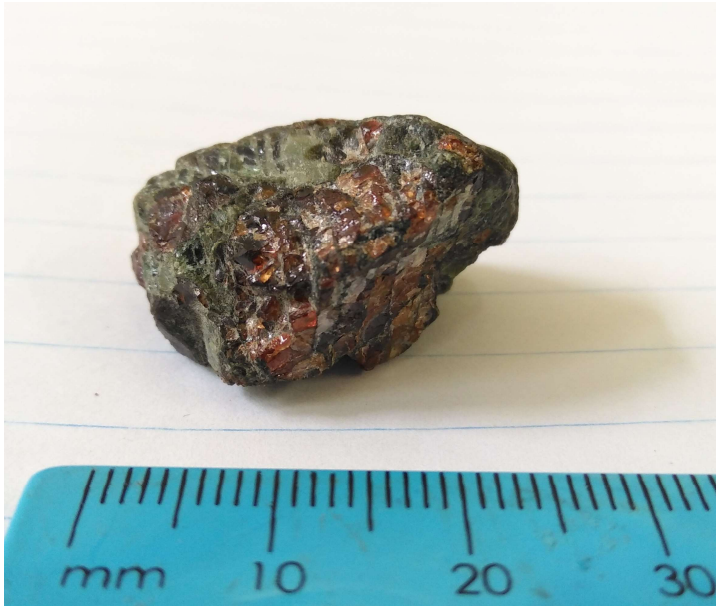

Appendix Figure 2. *Photograph of hand sample DGE-2*

Appendix Figure 3. *Photograph of hand sample DGE-3*

Appendix Figure 4*. Photograph of hand sample DGE-4*

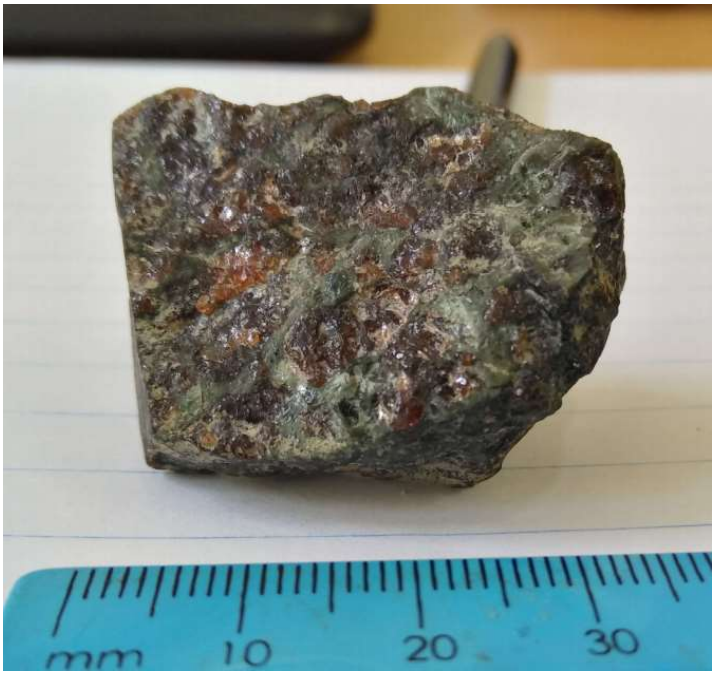

Appendix Figure 5. *Photograph of hand sample DGE-5*

Appendix Figure 6. *Photograph of hand sample DGE-5*

***Appendix Figure 7**. Photograph of hand sample DGE-7*

***Appendix Figure 8**. Photograph of hand sample DGE-8*

Appendix Figure 9. *Photograph of hand sample DGO-1*

Appendix Figure 10. *Photograph of hand sample DGO-2*

***Appendix Figure 11**. Photograph of hand sample DGO-3*

***Appendix Figure 12**. Photograph of hand sample DGO-4*

Appendix Figure 13. *Photograph of hand sample DGO-5*

Appendix Figure 14. *Photograph of hand sample DGO-6*

Appendix Figure 15. *Photograph of hand sample DGO-7*

Appendix Figure 16. *Photograph of hand sample DGO-8*

Appendix Figure 17. *Photograph of hand sample DGO-9*

Appendix Figure 18*. Photograph of hand sample DGO-10*

Appendix Figure 19. *Photograph of hand sample DGO-11*

Appendix Figure 20*. Photograph of hand sample DGO-12*

***Appendix Figure 21**. Photograph of hand sample DGO-13*

***Appendix Figure 22.** Photograph of hand sample DGO-14*

Appendix Figure 23. *Photograph of hand sample DGO-15*

Appendix Figure 24*. Photograph of hand sample DGO-16*

Appendix Figure 25. *Photograph of hand sample DGO-17*

Appendix Figure 26. *Photograph of hand sample DGO-18*

7.2 Appendix Tables

Appendix Table 1. Cation abundances for garnet from Belllsbank and Bobbejaan eclogite xenoliths, calculated on a basis of 12 oxygens per structural unit

	DGE-1	DGE-2	DGE-3	DGE-4	DGE-5	DGE-6	DGE-8	DGO-1	DGO-2	DGO-3	DGO-4	DGO-5	DGO-6	DGO-7	DGO-8	DGO-9	DGO-10	DGO-11	DGO-12	DGO-13	DGO-14	DGO-15	DGO-16	DGO-17	DGO-18
Si	2.984	2.975	2.995	2.951	2.954	2.957	2.972	2.943	2.983	2.932	2.930	2.980	2.916	2.952	2.925	2.993	3.014	2.954	2.951	2.949	2.932	2.994	2.959	2.984	2.951
Ti	0.019	0.007	0.019	0.006	0.010	0.010	0.009	0.008	0.008	0.006	0.010	0.009	0.007	0.009	0.008	0.005	0.004	0.006	0.010	0.005	0.008	0.007	0.008	0.005	0.010
Al	1.927	1.971	1.938	1.960	1.971	1.966	1.959	1.977	1.976	1.983	1.983	1.969	1.970	1.967	1.968	1.965	1.990	1.975	1.966	1.984	1.979	1.979	1.964	1.972	1.966
Cr	0.004	0.004	0.005	0.003	0.003	0.004	0.003	0.001	0.001	0.001	0.004	0.005	0.001	0.005	0.011	0.003	0.001	0.006	0.004	0.001	0.005	0.004	0.011	0.001	0.004
Fe	0.825	0.762	0.830	0.966	0.856	0.831	1.151	0.531	0.710	0.592	0.659	0.806	0.890	0.813	0.979	0.848	0.607	0.740	0.842	0.612	0.779	0.663	0.758	0.610	0.842
Mn	0.029	0.016	0.031	0.023	0.017	0.019	0.026	0.010	0.010	0.010	0.012	0.015	0.018	0.018	0.022	0.023	0.010	0.014	0.019	0.010	0.014	0.013	0.014	0.010	0.019
Mg	1.900	1.300	1.869	1.253	1.001	1.339	1.010	0.686	1.328	1.382	1.124	1.357	1.473	1.350	1.681	1.117	1.331	1.422	1.362	1.372	1.382	1.132	1.217	1.345	1.362
Ca	0.297	0.958	0.298	0.832	1.177	0.865	0.862	1.837	0.974	1.088	1.270	0.851	0.717	0.878	0.400	1.042	1.038	0.876	0.837	1.061	0.893	1.201	1.061	1.068	0.837
Na	0.013	0.007	0.013	0.007	0.011	0.008	0.008	0.006	0.009	0.006	0.009	0.008	0.006	0.008	0.006	0.005	0.005	0.006	0.008	0.006	0.008	0.007	0.008	0.005	0.008
K	0.001	0.000	0.001	0.000	0.000	0.001	0.001	0.000	0.001	0.001	0.000	0.000	0.001	0.000	0.001	0.000	0.000	0.000	0.001	0.000	0.000	0.000	0.000	0.001	0.000
Total	8.000	8.000	8.000	8.000	8.000	8.000	8.000	8.000	8.000	8.000	8.000	8.000	8.000	8.000	8.000	8.000	8.000	8.000	8.000	8.000	8.000	8.000	8.000	8.000	8.000
Mg#	70	63	69	56	54	62	47	56	65	70	63	63	62	62	63	57	69	66	62	69	64	63	62	69	62
Ca#	9.73	31.55	9.82	27.07	38.58	28.32	28.26	59.95	32.21	35.41	41.43	28.08	23.15	28.70	12.97	34.39	34.77	28.71	27.34	34.73	29.12	39.91	34.79	35.20	27.34
Prp	64	44	63	43	34	46	34	23	45	47	39	46	51	46	58	37	45	48	46	47	47	38	41	45	46
Alm	25	23	26	28	25	24	36	14	22	15	17	25	24	24	28	27	20	21	24	17	21	21	22	18	24
Sps	1	1	1	1	1	1	1	0	0	0	0	1	1	1	1	1	0	0	1	0	0	0	0	0	1
Grs	10	31	10	26	38	28	28	59	32	34	40	28	22	28	13	34	35	28	27	34	28	40	34	35	27
Uv	0	0	0	0	0	0	0	0	0	0	0	0	0	0	0	0	0	0	0	0	0	0	0	0	0
And	0	1	0	2	2	2	1	4	1	3	3	1	2	2	1	1	0	2	2	2	2	1	2	1	2

*Mg#: molar (Mg/(Mg+Fe))*100 ; Ca#: molar Ca/(Ca+Mn+Fe+Mg) ; 2σ standard errors are reported in appendix table 5 ; Prp: % pyrope component, Alm: % almandine component, Sps: % spessartine component, Grs: % grossular component, Uv: % uvarovite component, And: % andradite component.*

Appendix Table 2. Cation abundances for clinopyroxene from Bellsbank and Bobbejaan eclogite xenoliths, calculated on a basis of 6 oxygens per structural unit

	DGE-1	DGE-2	DGE-3	DGE-4	DGE-5	DGE-6	DGE-8	DGO-1	DGO-2	DGO-3	DGO-4	DGO-5	DGO-6	DGO-7	DGO-8	DGO-9	DGO-10	DGO-11	DGO-12	DGO-13	DGO-14	DGO-15	DGO-16	DGO-17	DGO-18
Si	1.979	1.963	1.979	1.953	1.942	1.957	1.969	1.919	1.944	1.928	1.916	1.954	1.930	1.957	1.946	1.967	1.977	1.946	1.955	1.933	1.935	1.954	1.952	1.953	1.958
Ti	0.011	0.005	0.012	0.004	0.007	0.006	0.006	0.002	0.006	0.003	0.006	0.008	0.005	0.006	0.008	0.003	0.003	0.005	0.003	0.003	0.007	0.005	0.005	0.004	0.005
Al	0.205	0.354	0.206	0.344	0.576	0.267	0.388	0.748	0.607	0.669	0.718	0.433	0.432	0.332	0.250	0.449	0.678	0.459	0.358	0.677	0.534	0.649	0.566	0.671	0.377
Cr	0.002	0.004	0.002	0.001	0.002	0.008	0.001	0.000	0.000	0.001	0.002	0.003	0.001	0.001	0.006	0.002	0.000	0.003	0.000	0.000	0.003	0.002	0.006	0.001	0.001
Fe	0.150	0.104	0.149	0.099	0.077	0.120	0.115	0.035	0.048	0.031	0.033	0.071	0.080	0.094	0.140	0.087	0.034	0.064	0.112	0.035	0.056	0.048	0.049	0.035	0.091
Mn	0.004	0.001	0.004	0.001	0.000	0.001	0.001	0.000	0.001	0.000	0.000	0.001	0.001	0.001	0.001	0.001	0.000	0.000	0.001	0.000	0.000	0.000	0.000	0.000	0.001
Mg	0.760	0.581	0.754	0.600	0.403	0.652	0.540	0.300	0.406	0.364	0.322	0.541	0.543	0.621	0.671	0.500	0.336	0.523	0.573	0.350	0.456	0.357	0.427	0.345	0.575
Ca	0.640	0.629	0.644	0.657	0.471	0.688	0.614	0.398	0.468	0.427	0.403	0.594	0.587	0.654	0.678	0.568	0.403	0.574	0.637	0.409	0.511	0.430	0.487	0.407	0.621
Na	0.248	0.358	0.248	0.338	0.521	0.296	0.366	0.597	0.513	0.573	0.595	0.391	0.418	0.330	0.298	0.421	0.562	0.420	0.358	0.587	0.493	0.551	0.504	0.580	0.368
Ni	0.001	0.002	0.001	0.002	0.002	0.003	0.001	0.001	0.005	0.005	0.004	0.004	0.002	0.004	0.002	0.002	0.006	0.004	0.002	0.006	0.005	0.003	0.003	0.005	0.003
Total	4.000	4.000	4.000	4.000	4.000	4.000	4.000	4.000	4.000	4.000	4.000	4.000	4.000	4.000	4.000	4.000	4.000	4.000	4.000	4.000	4.000	4.000	4.000	4.000	4.000
Mg#	83	85	83	86	84	84	82	89	89	92	91	88	87	87	83	85	91	89	84	91	89	88	90	91	86
Ca#	41	48	42	48	50	47	48	54	51	52	53	49	48	48	46	49	52	49	48	52	50	51	51	52	48
%En	49	44	49	44	42	45	43	41	44	44	42	45	45	45	45	43	43	45	43	44	45	43	44	44	45
%Wo	41	48	42	48	50	47	48	54	51	52	53	49	48	48	46	49	52	49	48	52	50	51	51	52	48
%Fs	10	8	10	7	8	8	9	5	5	4	4	6	7	7	9	8	4	6	9	4	6	6	5	4	7
xJd	0.22	0.35	0.22	0.33	0.51	0.28	0.35	0.59	0.50	0.57	0.58	0.37	0.41	0.32	0.28	0.41	0.55	0.41	0.35	0.58	0.48	0.54	0.49	0.57	0.36

*Mg#: molar (Mg/(Mg+Fe))*100); xJd (jadeite proportion) calculated as molar (Na – Cr – [2*Ti]) ; 2σ standard errors are reported in Appendix 4 ; Wo: % wollastonite component, En: % enstatite component, Fs: % ferrosilite component*

Appendix Table 3. Reference material and standard results for LA-ICPMS mineral analyses

	NIST614				NIST612				BCR2-G				BHVO-G			
	ppm (n = 33)	1SD (n = 33)	RV[1] (ppm)	% error	ppm (n = 101)	1SD (n = 101)	RV[2] (ppm)	% error	ppm (n = 32)	1SD (n = 32)	RV[3] (ppm)	% error	ppm (n = 33)	1SD (n = 33)	RV[4] (ppm)	% error
V	1.03	0.08	1.010	2.4	38.95	0.52	38.800	0.4	406	24.23	417.600	-2.8	317.9	10.95	313.800	1.3
Ni	1.92	0.78	1.100	74.2	38.62	1.13	38.800	-0.5	12.23	1.30	12.570	-2.7	124.0	3.78	120.000	3.4
Sc	1.15	0.19	0.740	55.6	41.01	0.26	39.900	2.8	33.74	0.65	33.530	0.6	32.57	0.49	31.420	3.7
Rb	0.86	0.09	0.855	0.7	31.42	0.41	31.400	0.1	46.48	0.96	46.020	1.0	9.30	0.19	9.520	-2.3
Th	0.78	0.04	0.748	4.1	37.81	0.42	37.790	0.1	5.72	0.12	5.828	-1.9	1.17	0.05	1.225	-4.6
U	0.87	0.04	0.823	5.2	37.38	0.45	37.380	0.0	1.71	0.06	1.683	1.4	0.43	0.03	0.418	1.8
Nb	0.86	0.04	0.824	4.2	40.00	0.35	38.900	2.8	11.97	0.25	12.440	-3.8	17.80	0.51	18.530	-3.9
Ta	0.84	0.03	0.808	4.3	40.00	0.29	37.600	6.4	0.77	0.04	0.785	-2.3	1.12	0.06	1.174	-4.7
La	0.73	0.03	0.720	1.1	35.80	0.13	36.000	-0.6	23.99	0.47	25.080	-4.3	14.82	0.39	15.440	-4.0
Ce	0.81	0.04	0.813	-0.4	38.67	0.41	38.400	0.7	50.77	1.15	53.120	-4.4	36.77	0.71	38.080	-3.4
Pr	0.78	0.03	0.768	2.0	37.20	0.44	37.900	-1.8	6.42	0.16	6.827	-6.0	5.02	0.16	5.419	-7.3
Pb	2.38	0.09	2.320	2.7	38.60	0.64	38.750	-0.4	10.91	0.41	10.590	3.0	1.81	0.06	2.037	-11.4
Sr	47.38	0.98	45.80	3.5	78.47	0.61	78.400	0.1	304	29.76	337.400	-9.9	354	37.31	399.200	-11.3
Nd	0.80	0.08	0.752	6.8	35.90	0.54	35.500	1.1	27.15	0.75	28.260	-3.9	23.51	0.65	24.780	-5.1
Sm	0.84	0.08	0.754	10.8	38.14	0.50	37.700	1.2	6.38	0.26	6.547	-2.5	5.89	0.23	6.165	-4.5
Zr	0.82	0.07	0.848	-2.7	38.05	0.61	37.900	0.4	167.3	5.13	186.500	-10.3	155.36	3.68	174.600	-11.0
Hf	0.72	0.06	0.711	1.4	35.04	0.45	36.700	-4.5	4.47	0.15	4.972	-10.0	3.97	0.13	4.440	-10.5
Eu	0.77	0.04	0.770	-0.6	34.97	0.46	35.600	-1.8	1.84	0.07	1.989	-7.6	1.97	0.06	2.053	-4.3
Ti	3.37	1.08	3.610	-6.5	44.12	1.61	44.000	0.3	13193	131	14100	-6.4	15954	185	-	-
Gd	0.80	0.06	0.763	4.8	36.76	0.67	37.300	-1.4	6.11	0.21	6.811	-10.3	5.54	0.17	6.285	-11.8
Tb	0.75	0.04	0.739	1.0	36.01	0.43	37.600	-4.2	0.95	0.04	1.077	-11.4	0.83	0.04	0.946	-12.3
Dy	0.79	0.07	0.746	5.8	36.02	0.31	35.500	1.5	6.14	0.20	6.424	-4.5	5.11	0.19	5.272	-3.1
Y	0.79	0.05	0.790	0.3	38.05	0.45	38.300	-0.7	31.85	0.69	36.070	-11.7	23.28	0.56	26.230	-11.2
Ho	0.77	0.03	0.749	3.4	38.01	0.45	38.300	-0.8	1.25	0.06	1.313	-5.1	0.95	0.05	0.984	-3.8
Er	0.77	0.05	0.740	3.6	38.01	0.55	38.000	0.0	3.45	0.12	3.670	-6.0	2.42	0.10	2.501	-3.4
Tm	0.79	0.04	0.732	7.4	37.97	0.53	36.800	3.2	0.51	0.03	0.534	-4.4	0.32	0.02	0.329	-2.1
Yb	0.77	0.08	0.777	-0.8	39.21	0.14	39.200	0.0	3.27	0.14	3.392	-3.5	1.93	0.13	1.987	-2.7
Lu	0.76	0.03	0.732	3.5	36.92	0.49	37.000	-0.2	0.49	0.03	0.505	-3.1	0.27	0.02	0.278	-3.7

*Mg#: molar (Mg/(Mg+Fe))*100), Ca#: molar (Ca/(Ca+Mn+Fe+Mg)*100). 1SD= 1 Standard deviation; RV[1]= Reference value; RV[2]= RV[3]= Reference values from Jochum et al., (2016); % error = relative percentage error expressed as (measured ppm – RV)/(RV*100).*

Appendix Table 4. Clinopyroxene trace element concentrations with internal 2-sigma error (2SE) and relative percentage (%)

	DGE-1			DGE-2			DGE-3			DGE-4			DGE-5			DGE-6			DGE-8			DGO-1			DGO-2			DGO-3			DGO-4			DGO-5		
	ppm	2 SE	%	ppm	2 SE	%	ppm	2 SE	%	ppm	2 SE	%	ppm	2 SE	%	ppm	2 SE	%	ppm	2 SE	%	ppm	SD (n=	%	ppm	2 SE	%	ppm	2 SE	%	ppm	2 SE	%	ppm	2 SE	%
V	######	9.300	1.8	######	10.900	1.5	######	6.900	1.5	######	14.478	1.6	######	12.078	1.7	######	13.211	1.5	######	12.700	1.7				######	5.617	2.8	######	4.333	1.9	######	13.757	2.0	######	13.875	1.6
Ni	422	15	4	683	22	3	403	11	3	985	22	2	790	18	2	1256	79	6	374	13	3				1586	101	6	1847	50	3	1569	40	3	1619	34	2
Sc	35.812	0.998	2.8	27.039	0.516	1.9	36.218	1.147	3.2	32.279	1.129	3.5	13.789	0.780	5.7	10.732	0.397	3.7	38.172	0.784	2.1				6.162	0.502	8.1	2.116	0.280	13.2	5.736	0.423	7.4	12.915	0.645	5.0
Rb	0.000	0.000		0.000	0.000		0.000	0.000		0.015	0.008	51.5	0.000	0.000		0.142	0.027	19.0	0.075	0.020	26.4				0.067	0.018	27.5	0.069	0.013	19.4	0.043	0.017	40.0	0.000	0.000	
Th	0.062	0.015	24.8	0.175	0.034	19.4	0.061	0.021	35.0	0.192	0.040	20.8	0.021	0.017	80.2	0.277	0.042	15.2	0.072	0.022	30.3				0.057	0.023	39.7	0.049	0.023	48.1	0.071	0.031	43.5	0.160	0.048	30.0
U	0.016	0.006	41.8	0.013	0.007	50.9	0.019	0.012	65.2	0.017	0.009	50.8	0.006	0.006	103.0	0.032	0.010	29.6	0.025	0.010	39.0				0.032	0.023	70.8	0.001	0.335	######	0.002	0.002	96.8	0.013	0.009	66.0
Nb	0.991	0.104	10.5	0.222	0.037	16.6	1.035	0.109	10.6	0.323	0.078	24.2	0.419	0.084	20.0	0.915	0.069	7.5	0.171	0.036	20.9				0.212	0.054	25.6	0.023	0.016	67.9	0.103	0.038	37.4	0.985	0.119	12.0
Ta	0.149	0.025	16.7	0.013	0.007	51.9	0.167	0.030	18.1	0.000	0.000		0.020	0.011	55.4	0.030	0.011	37.9	0.008	0.004	57.5				0.011	0.005	43.5	0.001	0.002	136.4	0.004	0.004	95.6	0.037	0.017	47.3
La	3.216	0.143	4.5	1.458	0.104	7.1	3.478	0.171	4.9	1.594	0.118	7.4	0.468	0.071	15.1	2.827	0.153	5.4	1.550	0.119	7.6				0.446	0.078	17.5	0.295	0.049	16.7	0.452	0.072	16.0	1.808	0.126	6.9
Ce	11.833	0.394	3.3	4.012	0.133	3.3	12.590	0.393	3.1	2.820	0.171	6.1	1.588	0.137	8.6	10.638	0.318	3.0	5.390	0.161	3.0				0.987	0.130	13.1	0.520	0.064	12.3	0.772	0.090	11.7	3.705	0.216	5.8
Pr	1.919	0.110	5.7	0.412	0.042	10.2	2.150	0.112	5.2	0.232	0.044	19.2	0.246	0.051	20.7	1.510	0.099	6.5	0.657	0.063	9.6				0.116	0.032	27.8	0.048	0.018	36.9	0.059	0.023	38.8	0.355	0.058	16.3
Pb	0.261	0.048	18.3	0.566	0.088	15.6	0.297	0.076	25.5	0.139	0.058	41.5	0.028	0.015	52.9	0.418	0.098	23.4	0.071	0.027	37.8				0.073	0.041	55.7	0.018	0.011	63.1	0.058	0.036	61.3	0.113	0.051	45.0
Sr	######	4.278	2.2	37.426	0.788	2.1	######	3.478	1.9	38.503	1.112	2.9	56.542	1.174	2.1	81.848	1.971	2.4	92.018	2.336	2.5				28.462	5.612	19.7	16.117	0.584	3.6	9.389	0.430	4.6	47.615	1.036	2.2
Nd	10.257	0.473	4.6	1.008	0.153	15.2	10.374	0.652	6.3	0.597	0.169	28.3	1.269	0.241	19.0	5.984	0.464	7.8	2.394	0.263	11.0				0.647	0.197	30.4	0.221	0.082	37.2	0.178	0.101	56.7	0.984	0.199	20.2
Sm	2.522	0.270	10.7	0.208	0.073	35.2	2.581	0.297	11.5	0.175	0.087	49.8	0.287	0.130	45.2	0.902	0.133	14.8	0.560	0.118	21.1				0.387	0.165	42.7	0.039	0.028	72.0	0.063	0.048	76.1	0.266	0.091	34.1
Zr	40.803	1.064	2.6	3.315	0.226	6.8	41.660	1.207	2.9	3.808	0.331	8.7	5.321	0.368	6.9	12.288	0.539	4.4	12.945	0.555	4.3				10.558	0.705	6.7	1.028	0.182	17.7	0.703	0.226	32.1	8.004	0.453	5.7
Hf	1.596	0.138	8.6	0.325	0.077	23.7	1.709	0.196	11.4	0.343	0.100	29.2	0.385	0.120	31.1	0.828	0.124	15.0	0.608	0.119	19.6				0.500	0.138	27.7	0.114	0.067	59.2	0.100	0.058	58.3	0.538	0.118	22.0
Eu	0.751	0.081	10.7	0.091	0.029	32.1	0.784	0.090	11.4	0.109	0.037	33.8	0.092	0.043	47.2	0.370	0.054	14.5	0.184	0.038	20.5				0.308	0.067	21.9	0.003	0.003	96.3	0.018	0.013	71.8	0.154	0.040	26.1
Ti	3929	82	2.1	1566	28	1.8	3794	69	1.8	1372	39	2.8	2194	55	2.5	1847	33	1.8	1927	33	1.7				1830	47	2.5	1257	29	2.3	1996	55	2.7	2616	61	2.3
Gd	2.168	0.254	11.7	0.457	0.118	25.8	2.171	0.323	14.9	0.481	0.158	32.8	0.214	0.101	47.4	0.623	0.113	18.2	0.583	0.141	24.1				0.462	0.176	38.2	0.000	0.000		0.076	0.070	91.9	0.288	0.116	40.3
Tb	0.293	0.035	11.9	0.074	0.018	24.5	0.327	0.042	12.7	0.083	0.023	27.5	0.029	0.015	52.1	0.079	0.016	20.4	0.086	0.021	23.9				0.084	0.025	30.0	0.001	0.001	95.3	0.011	0.008	71.8	0.040	0.018	45.2
Dy	1.572	0.148	9.4	0.451	0.098	21.6	1.582	0.187	11.8	0.454	0.115	25.4	0.113	0.054	48.3	0.340	0.069	20.4	0.447	0.089	19.8				0.475	0.078	16.4	0.006	0.006	94.8	0.043	0.031	73.2	0.207	0.080	38.6
Y	6.386	0.259	4.1	1.740	0.105	6.0	6.848	0.307	4.5	1.853	0.151	8.2	0.503	0.093	18.4	1.073	0.087	8.1	1.645	0.104	6.3				2.533	0.183	7.2	0.043	0.026	60.9	0.189	0.053	28.1	0.659	0.087	13.2
Ho	0.278	0.035	12.7	0.077	0.019	24.6	0.298	0.045	15.0	0.089	0.027	30.4	0.029	0.020	67.2	0.045	0.016	34.5	0.072	0.019	26.8				0.097	0.020	20.5	0.001	0.001	94.3	0.008	0.006	74.1	0.030	0.014	45.1
Er	0.641	0.081	12.7	0.171	0.053	30.7	0.654	0.111	17.0	0.186	0.066	35.2	0.043	0.032	74.5	0.097	0.040	41.5	0.157	0.050	32.2				0.260	0.054	20.7	0.000	0.000		0.009	0.009	97.0	0.089	0.054	60.5
Tm	0.074	0.016	21.2	0.020	0.011	52.8	0.083	0.022	26.4	0.020	0.013	64.4	0.004	0.004	122.5	0.006	0.006	86.6	0.019	0.009	49.5				0.034	0.012	34.6	0.000	0.000		0.004	0.005	119.6	0.009	0.007	83.5
Yb	0.386	0.083	21.4	0.105	0.052	49.4	0.365	0.100	27.4	0.131	0.070	53.8	0.015	0.022	150.0	0.026	0.021	79.6	0.104	0.057	54.5				0.277	0.080	28.9	0.000	0.000		0.014	0.016	116.2	0.065	0.055	84.5
Lu	0.049	0.012	24.7	0.016	0.010	62.4	0.049	0.015	31.1	0.015	0.011	74.0	0.005	0.006	113.0	0.001	0.001	91.7	0.007	0.005	68.5				0.047	0.016	35.0	0.002	0.002	129.0	0.001	0.002	130.0	0.015	0.016	106.7

Continued ...

	DGO-6			DGO-7			DGO-8			DGO-9			DGO-10			DGO-11			DGO-12			DGO-13			DGO-14			DGO-15			DGO-16			DGO-17			DGO-18		
	ppm	2 SE	%	ppm	2 SE	%	ppm	2 SE	%	ppm	2 SE	%	ppm	2 SE	%	ppm	2 SE	%	ppm	2 SE	%	ppm	2 SE	%	ppm	2 SE	%	ppm	2 SE	%	ppm	2 SE	%	ppm	2 SE	%	ppm	2 SE	%
	######	8.975	1.5	######	10.878	1.9	######	10.011	1.8	######	15.917	1.5	######	3.617	2.1	319.388	5.663	1.8	######	20.444	2.0	######	3.567	2.2	######	15.889	0.0	######	10.613	1.6	######	12.378	1.9	######	5.233	1.8	######	10.433	1.7
	1106	26	2	1429	40	3	876	26	3	780	20	3	2241	71	3	1567	40	2.5	668	21	3	2096	52	2	1844	42	0	927	26	3	1294	36	3	3395	96	3	1134	32	3
	9.629	0.734	7.6	14.262	0.683	4.8	20.770	0.759	3.7	23.828	0.608	2.5	1.645	0.255	15.5	11.733	0.540	4.6	43.010	1.353	3.1	1.750	0.389	22.2	8.632	0.566	0.0	5.474	0.324	5.9	5.194	0.391	7.5	3.193	0.393	12.3	13.449	0.526	3.9
	0.000	0.000		0.000	0.000		0.000	0.000		0.000	0.000		0.000	0.000		0.022	0.007	32.6	0.381	0.059	15.5	0.000	0.000		0.021	0.013	0.0	0.000	0.000		0.000	0.000		0.000	0.000		0.000	0.000	
	0.177	0.051	28.9	0.186	0.041	22.3	0.323	0.048	15.0	0.081	0.022	27.5	0.037	0.022	58.1	0.042	0.012	27.7	0.230	0.045	19.4	0.043	0.024	56.4	0.105	0.031	0.0	0.058	0.024	41.1	0.049	0.017	34.5	0.058	0.027	46.1	0.186	0.030	16.2
	0.012	0.008	70.4	0.013	0.009	64.6	0.024	0.010	41.6	0.005	0.000	0.0	0.001	0.335	######	0.005	0.003	61.5	0.021	0.010	50.3	0.005	0.004	87.8	0.011	0.008	0.0	0.003	0.128	3750.0	0.004	0.004	99.4	0.005	0.005	98.5	0.012	0.006	51.4
	0.353	0.077	21.7	0.000	0.223	######	0.013	0.015	114.9	0.210	0.036	16.9	0.042	0.026	61.4	0.195	0.049	24.9	0.598	0.085	14.3	0.028	0.024	86.4	0.006	0.007	0.0	0.915	0.103	11.2	0.333	0.064	19.2	0.045	0.024	54.6	0.465	0.080	17.3
	0.023	0.013	56.1	0.000	0.000		0.000	0.000		0.007	0.004	64.9	0.007	0.006	88.0	0.003	0.002	63.0	0.030	0.012	40.1	0.004	0.004	94.6	0.001	0.001	0.0	0.023	0.012	52.0	0.011	0.007	63.0	0.012	0.009	76.2	0.027	0.011	41.5
	1.640	0.125	7.6	1.384	0.113	8.1	3.474	0.172	5.0	0.752	0.061	8.1	0.505	0.071	14.1	1.253	0.086	6.8	3.797	0.187	4.9	0.541	0.080	14.8	1.516	0.117	0.0	0.502	0.062	12.4	0.706	0.076	10.8	0.764	0.086	11.2	1.852	0.096	5.2
	3.049	0.184	6.0	2.082	0.136	6.5	7.918	0.343	4.3	1.265	0.074	5.9	1.245	0.134	10.7	2.732	0.140	5.1	10.060	0.373	3.7	1.269	0.127	10.0	2.717	0.156	0.0	1.250	0.107	8.6	1.007	0.082	8.1	1.919	0.176	9.2	2.854	0.144	5.1
	0.243	0.045	18.4	0.252	0.041	16.4	0.894	0.074	8.3	0.114	0.020	17.2	0.154	0.031	20.0	0.280	0.038	13.7	1.229	0.088	7.2	0.166	0.042	25.1	0.216	0.039	0.0	0.124	0.026	20.8	0.087	0.022	24.9	0.237	0.042	17.9	0.188	0.027	14.6
	0.173	0.052	29.9	0.314	0.076	24.3	0.389	0.081	20.9	0.091	0.029	31.7	0.035	0.021	59.5	0.270	0.068	25.0	1.083	0.680	62.8	0.027	0.018	66.7	0.181	0.078	0.0	0.011	0.012	103.3	0.019	0.012	64.5	0.069	0.043	62.0	0.197	0.049	24.7
	23.203	0.726	3.1	76.533	1.811	2.4	65.600	1.478	2.3	20.192	0.590	2.9	34.355	1.303	3.8	44.400	1.081	2.4	######	2.878	2.4	35.544	1.091	3.1	32.106	0.892	0.0	25.299	0.769	3.0	24.572	0.649	2.6	53.721	1.622	3.0	26.396	0.738	2.8
	0.703	0.164	23.3	1.170	0.203	17.4	3.102	0.297	9.6	0.365	0.091	25.0	0.468	0.116	24.8	0.729	0.150	20.6	4.486	0.411	9.2	0.422	0.152	36.1	0.712	0.181	0.0	0.358	0.103	28.7	0.268	0.082	30.5	0.674	0.170	25.2	0.437	0.104	23.8
	0.220	0.101	45.9	0.461	0.143	31.0	0.879	0.168	19.1	0.085	0.048	56.3	0.035	0.034	97.1	0.158	0.071	45.2	0.663	0.188	28.3	0.037	0.038	103.0	0.223	0.103	0.0	0.087	0.060	68.8	0.062	0.048	76.8	0.056	0.048	85.1	0.217	0.084	38.5
	6.214	0.446	7.2	11.910	0.637	5.3	12.271	0.686	5.6	1.683	0.189	11.2	1.102	0.227	20.6	3.859	0.328	8.5	5.310	0.422	8.0	1.213	0.299	24.6	6.546	0.450	0.0	0.876	0.189	21.5	1.377	0.263	19.1	1.637	0.288	17.6	6.422	0.380	5.9
	0.501	0.138	27.4	0.651	0.122	18.8	0.778	0.129	16.6	0.208	0.060	29.1	0.143	0.069	48.4	0.318	0.079	24.7	0.337	0.087	25.8	0.118	0.060	51.0	0.650	0.156	0.0	0.115	0.057	49.6	0.200	0.051	25.7	0.187	0.076	40.6	0.456	0.073	16.0
	0.125	0.049	39.4	0.331	0.063	19.0	0.415	0.064	15.4	0.032	0.016	49.2	0.000	0.000		0.093	0.034	36.2	0.180	0.038	20.9	0.030	0.027	90.4	0.103	0.045	0.0	0.019	0.012	65.5	0.047	0.024	49.9	0.043	0.025	58.5	0.139	0.031	21.9
	1709	45	2.6	1864	45	2.4	2580	64	2.5	917	20	2.2	1094	27	2.4	1716	42	2.5	1225	41	3.3	1125	36	3.2	2280	60	0.0	1529	32	2.1	1683	39	2.3	1833	40	2.2	1653	37	2.2
	0.265	0.105	39.8	0.560	0.165	29.5	1.559	0.270	17.3	0.207	0.078	37.5	0.000	0.000		0.094	0.052	55.2	0.522	0.154	29.5	0.009	0.014	155.4	0.224	0.100	0.0	0.100	0.069	69.3	0.047	0.045	97.6	0.009	0.007	76.6	0.372	0.127	34.2
	0.051	0.023	45.9	0.063	0.020	31.1	0.213	0.032	15.1	0.036	0.013	35.1	0.003	0.004	126.6	0.018	0.009	49.9	0.081	0.020	24.6	0.001	0.002	128.1	0.037	0.017	0.0	0.007	0.005	77.4	0.008	0.006	74.5	0.003	0.002	96.9	0.049	0.015	30.3
	0.202	0.085	42.1	0.355	0.103	29.1	1.113	0.152	13.7	0.244	0.075	30.9	0.018	0.024	134.3	0.098	0.054	55.3	0.451	0.113	25.1	0.014	0.023	165.9	0.201	0.071	0.0	0.027	0.021	78.3	0.046	0.030	65.0	0.007	0.006	83.6	0.260	0.078	29.9
	0.616	0.083	13.4	1.076	0.120	11.2	3.690	0.199	5.4	1.059	0.080	7.6	0.006	0.006	91.7	0.281	0.048	17.1	1.889	0.146	7.8	0.030	0.019	64.0	0.716	0.098	0.0	0.126	0.036	29.0	0.132	0.049	36.9	0.051	0.026	51.5	0.744	0.082	11.1
	0.032	0.018	56.3	0.048	0.018	37.1	0.163	0.031	19.3	0.044	0.016	36.3	0.001	0.001	109.1	0.007	0.005	65.5	0.082	0.023	27.8	0.002	0.002	110.2	0.030	0.015	0.0	0.004	0.005	109.8	0.006	0.005	87.4	0.001	0.002	158.1	0.033	0.010	30.8
	0.067	0.044	65.6	0.101	0.052	51.1	0.298	0.067	22.6	0.091	0.037	40.4	0.002	0.003	146.2	0.022	0.019	87.4	0.172	0.063	36.6	0.005	0.003	67.4	0.074	0.051	0.0	0.007	0.006	91.1	0.016	0.014	87.5	0.000	0.000		0.070	0.027	38.0
	0.008	0.006	72.4	0.013	0.010	80.2	0.034	0.017	50.2	0.012	0.008	64.0	0.000	0.000		0.003	0.003	96.8	0.019	0.012	60.8	0.000	0.000		0.007	0.007	0.0	0.000	0.000		0.001	0.001	117.8	0.000	0.001	205.6	0.006	0.004	64.5
	0.008	0.008	106.6	0.048	0.039	81.6	0.157	0.071	44.9	0.050	0.038	76.2	0.000	0.000		0.003	0.002	65.2	0.092	0.061	66.2	0.000	0.000		0.041	0.036	0.0	0.000	0.000		0.001	0.002	190.0	0.007	0.011	168.3	0.035	0.026	74.7
	0.002	0.002	103.8	0.005	0.005	102.6	0.013	0.010	74.5	0.007	0.006	77.4	0.000	0.000		0.000	0.000		0.010	0.008	77.8	0.001	0.002	158.5	0.003	0.003	0.0	0.000	0.001	409.1	0.000	0.001	174.4	0.000	0.000		0.005	0.004	82.7

*ppm = part per million; 2 SE = internal 2-sigma error; relative percentage (%) = expressed as ((2 SE)/(ppm))*100*

Appendix Table 5. Garnet trace element concentrations with internal 2-sigma error (2SE) and relative percentage (%)

	DGE-1			DGE-2			DGE-3			DGE-4			DGE-5			DGE-6			DGE-8			DGO-1			DGO-2			DGO-3			DGO-4			DGO-5		
	ppm	2 SE	%	ppm	2 SE	%	ppm	2 SE	%	ppm	2 SE	%	ppm	2 SE	%	ppm	2 SE	%	ppm	2 SE	%	ppm	2 SE	%	ppm	2 SE	%	ppm	2 SE	%	ppm	2 SE	%	ppm	2 SE	%
V	179.7	4.6	2.6	263.8	5.1	1.9	175.4	6.1	3.5	329.3	5.8	1.8	271.2	5.2	1.9	329.3	5.9	1.8	249.4	4.1	1.6	374.1	6.8	1.8	65.8	2.0	3.1	63.3	1.5	2.4	301.0	5.1	1.7	232.3	5.1	2.2
Ni	53.0	4.5	8.6	63.2	4.0	6.3	51.1	4.6	9.0	66.9	4.5	6.8	77.4	4.8	6.1	124.2	4.5	3.6	25.4	2.3	9.1	56.9	4.2	7.4	240.3	9.6	4.0	235.9	8.7	3.7	238.7	5.1	2.1	130.5	5.1	3.9
Sc	92.3	2.6	2.8	135.7	2.2	1.6	90.2	3.5	3.9	113.4	2.8	2.4	77.2	2.2	2.8	50.0	1.2	2.4	118.4	2.0	1.7	45.5	1.1	2.5	14.5	0.9	6.3	22.5	0.8	3.4	79.3	1.7	2.2	53.4	1.7	3.2
Rb	0.000	0.000					0.000	0.000		0.000	0.000		0.000	0.000		0.000	0.000		0.000	0.000		0.000	0.000		0.000	0.000		0.000	0.000		0.000					
Th	0.001	0.002		0.031	0.018	59.1	0.000	0.143		0.021	0.013	62.2	0.018	0.015	82.4	0.022	0.016	72.4	0.014	0.013	89.5	0.066	0.022	33.8	0.039	0.026	66.2	0.033	0.019	58.2	0.098	0.030	30.5	0.042	0.030	71.1
U	0.011	0.008	72.3	0.035	0.012	34.1	0.013	0.009	70.2	0.038	0.019	51.0	0.052	0.021	40.4	0.050	0.017	34.6	0.049	0.015	30.0	0.024	0.010	43.7	0.049	0.021	42.8	0.017	0.009	54.5	0.020	0.016	78.1	0.037	0.016	43.0
Nb	0.217	0.054	24.7	0.099	0.032	32.4	0.197	0.060	30.6	0.074	0.034	46.0	0.289	0.086	29.6	0.298	0.053	17.9	0.069	0.024	34.6	0.148	0.049	33.4	0.002	0.003	162.6	0.021	0.017	80.1	0.071	0.065	90.9	0.278	0.065	23.4
Ta	0.024	0.013	53.6	0.019	0.011	57.9	0.018	0.010	54.4	0.000	0.000		0.003	0.004	160.0	0.000	0.000		0.000	0.000		0.000	0.000		0.001	0.002	190.9	0.000	0.000		0.000	0.018		0.015	0.018	125.0
La	0.002	0.001	61.1	0.038	0.019	49.4	0.014	0.013	97.9	0.020	0.016	81.4	0.044	0.035	81.1	0.006	0.003	56.0	0.029	0.013	43.3	0.137	0.040	29.0	0.041	0.022	53.6	0.028	0.015	53.5	0.081	0.023	28.4	0.049	0.023	47.2
Ce	0.125	0.038	30.6	0.286	0.049	17.0	0.127	0.042	33.5	0.154	0.048	31.4	0.508	0.099	19.6	0.341	0.055	16.0	0.401	0.050	12.6	0.443	0.066	15.0	0.244	0.048	19.5	0.170	0.040	23.8	0.407	0.060	14.7	0.309	0.060	19.4
Pr	0.053	0.018	34.2	0.082	0.021	25.5	0.052	0.023	44.5	0.033	0.017	51.5	0.201	0.041	20.5	0.151	0.030	19.8	0.138	0.027	19.8	0.056	0.017	30.8	0.059	0.024	40.5	0.045	0.014	31.7	0.063	0.027	42.6	0.083	0.027	32.1
Pb	0.000	0.000		0.026	0.035	134.6	0.010	0.011	116.4	0.008	0.008	100.0	0.008	0.006	69.7	0.000	0.000		0.000	0.000		0.000	0.000		0.043	0.035	81.9	0.000	0.000		0.004	0.040		0.035	0.040	115.2
Sr	0.242	0.092	37.9	0.138	0.063	45.8	0.140	0.070	49.8	0.000	0.000		0.544	0.181	33.3	0.160	0.062	38.8	0.333	0.066	19.9	0.366	0.102	27.8	0.057	0.032	56.9	0.162	0.060	36.8	0.077	0.115	149.8	0.274	0.115	42.1
Nd	0.638	0.163	25.6	0.412	0.128	31.2	0.673	0.219	32.5	0.171	0.096	56.2	2.011	0.350	17.4	1.548	0.259	16.7	1.202	0.195	16.2	0.216	0.104	48.0	0.617	0.166	26.8	0.437	0.139	31.9	0.403	0.149	36.8	0.474	0.149	31.3
Sm	0.668	0.152	22.8	0.386	0.138	35.6	0.706	0.226	32.0	0.383	0.147	38.4	1.723	0.330	19.2	1.068	0.202	18.9	1.150	0.206	17.9	0.187	0.084	44.6	0.810	0.197	24.3	0.402	0.135	33.6	0.611	0.165	27.0	0.479	0.165	34.5
Zr	29.232	1.238	4.2	3.889	0.344	8.9	27.643	1.357	4.9	3.298	0.406	12.3	11.683	0.680	5.8	12.637	0.689	5.5	7.317	0.373	5.1	0.344	0.166	48.4	17.377	0.762	4.4	5.061	0.343	6.8	5.539	0.545	9.8	8.116	0.545	6.7
Hf	0.368	0.096	26.1	0.108	0.063	58.0	0.345	0.098	28.6	0.085	0.058	67.7	0.259	0.114	43.8	0.231	0.115	49.6	0.111	0.060	54.0	0.029	0.021	74.0	0.355	0.098	27.6	0.123	0.077	62.1	0.257	0.082	32.0	0.179	0.082	45.9
Eu	0.355	0.070	19.9	0.361	0.085	23.6	0.377	0.092	24.3	0.395	0.091	23.1	0.935	0.132	14.1	0.866	0.130	15.0	0.687	0.093	13.5	0.133	0.047	35.6	0.643	0.097	15.1	0.443	0.080	18.0	0.495	0.093	18.8	0.579	0.093	16.1
Ti	3530	113	3	1336	27	2	3250	120	4	1072	32	3	1544	49	3	1628	33	2	1394	29	2	1167	35	3	1268	37	3	829	18	2	1510	34	2	1265	34	3
Gd	1.766	0.253	14.3	3.053	0.451	14.8	1.819	0.313	17.2	2.644	0.401	15.2	3.658	0.514	14.0	2.607	0.473	18.2	3.923	0.420	10.7	0.659	0.168	25.5	1.226	0.298	24.3	0.718	0.197		2.194	0.361	16.5	1.829	0.361	19.8
Tb	0.441	0.057	13.0	1.040	0.099	9.5	0.469	0.067	14.2	0.898	0.102	11.4	0.850	0.103	12.1	0.611	0.078	12.8	1.063	0.093	8.7	0.148	0.030	20.4	0.225	0.052	23.3	0.140	0.030		0.632	0.056	8.8	0.474	0.056	11.8
Dy	4.416	0.298	6.7	12.019	0.657	5.5	4.584	0.403	8.8	9.134	0.661	7.2	6.885	0.519	7.5	5.393	0.499	9.3	10.258	0.605	5.9	1.166	0.162	13.9	1.411	0.217	15.4	1.059	0.192	18.2	6.066	0.446	7.4	3.886	0.446	11.5
Y	33.040	1.131	3.4	95.667	2.022	2.1	34.086	1.329	3.9	73.600	1.625	2.2	43.495	1.188	2.7	33.840	1.000	3.0	68.872	1.697	2.5	7.020	0.328	4.7	7.442	0.364	4.9	5.710	0.289	5.1	43.029	0.694	1.6	27.576	0.694	2.5
Ho	1.267	0.081	6.4	3.560	0.159	4.5	1.392	0.119	8.5	2.803	0.171	6.1	1.753	0.137	7.8	1.245	0.152	12.2	2.618	0.129	4.9	0.264	0.042	15.9	0.301	0.047	15.4	0.229	0.042	18.5	1.706	0.103	6.0	1.101	0.103	9.3
Er	4.658	0.351	7.5	12.980	0.643	5.0	4.679	0.380	8.1	9.759	0.566	5.8	5.548	0.463	8.3	3.841	0.460	12.0	8.778	0.423	4.8	0.871	0.124	14.2	0.818	0.135	16.5	0.630	0.121		5.647	0.319	5.6	3.510	0.319	9.1
Tm	0.857	0.073	8.6	2.155	0.164	7.6	0.881	0.099	11.3	1.749	0.159	9.1	0.887	0.098	11.0	0.594	0.096	16.2	1.426	0.129	9.1	0.145	0.027	18.7	0.129	0.037	29.0	0.115	0.031		0.987	0.090	9.1	0.598	0.090	15.0
Yb	6.111	0.448	7.3	16.528	0.846	5.1	6.211	0.577	9.3	12.590	0.908	7.2	6.045	0.583	9.6	4.453	0.606	13.6	10.344	0.586	5.7	0.875	0.175	20.1	0.872	0.207	23.7	0.743	0.200		7.074	0.493	7.0	4.100	0.493	12.0
Lu	0.965	0.081	8.4	2.507	0.188	7.5	1.013	0.114	11.3	2.173	0.166	7.7	0.938	0.119	12.7	0.695	0.098	14.2	1.551	0.113	7.3	0.137	0.026	18.8	0.122	0.035	28.7	0.123	0.031	25.0	1.127	0.091	8.0	0.683	0.091	13.2

Continued ...

DGO-6			DGO-7			DGO-8			DGO-9			DGO-10			DGO-11			DGO-12			DGO-13			DGO-14			DGO-15			DGO-16			DGO-17			DGO-18		
ppm	2 SE	%	ppm	2 SE	%	ppm	2 SE	%	ppm	2 SE	%	ppm	2 SE	%	ppm	2 SE	%	ppm	2 SE	%	ppm	2 SE	%	ppm	2 SE	%	ppm	2 SE	%	ppm	2 SE	%	ppm	2 SE	%	ppm	2 SE	%
138.4	3.2	2.3	182.2	6.2	3.4	124.6	4.0	3.2	355.2	5.6	1.6	43.3	1.1	2.4	83.8	2.2	2.6	294.5	6.5	2.2	44.6	1.7	3.8	262.0	23.3	0.0	195.2	3.2	1.6	180.7	3.5	1.9	40.4	0.9	2.3	177.2	4.9	2.8
88.4	5.4	6.1	184.3	13.6	7.4	75.6	7.6	10.0	61.9	3.2	5.1	299.7	9.7	3.2	144.1	6.3	4.3	47.1	5.5	11.7	292.7	10.8	3.7	121.5	75.0	0.0	97.7	4.9	5.0	124.2	6.2	5.0	227.4	6.5	2.9	112.5	7.3	6.5
47.9	1.7	3.6	80.2	3.2	4.0	58.0	2.3	3.9	128.9	2.0	1.5	17.1	0.7	3.9	66.2	2.0	3.1	155.1	4.0	2.6	18.1	1.0	5.2	41.5	28.8	0.0	50.6	1.1	2.2	33.7	1.1	3.3	15.9	0.4	2.6	70.9	2.1	2.9
0.000	0.000		0.000	0.000		0.000	0.000		0.000	0.000		0.000	0.000		0.000	0.000		0.000	0.000		0.000	0.000		0.400	0.600		0.000	0.000					0.000	0.000		0.000	0.000	
0.025	0.017	68.5	0.008	0.119		0.006	0.007	118.0	0.045	0.020	45.0	0.051	0.026	52.2	0.022	0.012	54.1	0.057	0.031	54.4	0.028	0.017	59.7	0.017	0.016	0.0	0.041	0.023	56.7	0.042	0.020	46.1	0.028	0.015	53.4	0.028	0.018	63.2
0.027	0.017	63.2	0.014	0.014	100.0	0.016	0.011	66.2	0.026	0.000	0.0	0.057	0.019	34.1	0.038	0.019	48.6	0.060	0.021	35.1	0.064	0.027	42.9	0.021	0.020	0.0	0.020	0.011	56.9	0.021	0.009	43.7	0.040	0.013	32.8	0.029	0.015	53.7
0.132	0.058	43.9	0.000	0.111		0.002	0.004	200.0	0.130	0.033	25.5	0.030	0.018	60.0	0.075	0.037	49.6	0.205	0.070	34.2	0.020	0.022	114.1	0.000	0.000		0.519	0.075	14.5	0.214	0.065	30.5	0.018	0.012	66.8	0.179	0.084	46.8
0.002	0.003	122.4	0.000	0.000		0.000	0.000		0.001	0.001		0.001	0.002	162.5	0.002	0.002	70.0	0.000	0.000		0.002	0.002	106.3	0.248	0.240	0.0	0.000	0.000					0.001	0.002	122.4	0.002	0.002	101.8
0.025	0.017	69.8	0.000	0.000		0.002	0.003	140.0	0.044	0.017	37.7	0.066	0.026	39.5	0.044	0.021	47.8	0.069	0.035	50.8	0.066	0.030	45.5	0.013	0.010	0.0	0.061	0.023	37.5	0.055	0.024	43.9	0.045	0.014	30.8	0.038	0.020	51.7
0.256	0.066	25.9	0.075	0.042	55.8	0.083	0.043	52.2	0.261	0.042	16.1	0.533	0.066	12.3	0.270	0.057	21.1	0.625	0.094	15.1	0.526	0.085	16.3	0.210	0.110	0.0	0.399	0.059	14.7	0.245	0.053	21.5	0.391	0.048	12.3	0.205	0.056	27.2
0.077	0.030	39.5	0.029	0.023	77.6	0.030	0.021	70.5	0.062	0.017	27.7	0.153	0.034	22.5	0.080	0.025	31.6	0.204	0.046	22.6	0.151	0.038	25.0	0.065	0.101	0.0	0.095	0.026	27.2	0.048	0.019	39.4	0.116	0.021	18.4	0.034	0.016	47.2
0.014	0.013	91.3	0.009	0.009	101.2	0.055	0.060	109.3	0.004	0.005	112.5	0.009	0.004	50.7	0.005	0.006	133.3	0.012	0.008	67.0	0.015	0.014	95.4	0.413	1.863	0.0	0.002	0.002	121.4	0.163	0.135	82.5	0.003	0.003	93.5	0.021	0.016	73.8
0.000	0.000		0.040	0.022	55.6	0.000	0.000	#DIV/0!	0.128	0.047	37.1	0.397	0.078	19.7	0.118	0.051	42.9	0.293	0.119	40.6	0.388	0.139	35.8	0.475	1.175	0.0	0.241	0.061	25.2	0.203	0.112	54.8	0.300	0.058	19.2	0.113	0.042	37.3
0.529	0.196	37.0	0.344	0.218	63.2	0.300	0.161	53.8	0.396	0.106	26.8	0.883	0.191	21.7	0.499	0.148	29.7	1.841	0.346	18.8	0.983	0.240	24.4	0.263	0.100	0.0	0.624	0.174	27.9	0.385	0.132	34.2	0.686	0.125	18.2	0.163	0.099	60.6
0.439	0.183	41.8	0.540	0.273	50.6	0.312	0.139	44.6	0.334	0.105	31.4	0.436	0.133	30.4	0.394	0.126	32.0	1.355	0.329	24.3	0.426	0.172	40.5	1.748	1.870	0.0	0.573	0.160	27.9	0.322	0.115	35.7	0.366	0.114	31.2	0.416	0.162	39.1
6.583	0.581	8.8	11.059	1.044	9.4	4.769	0.561	11.8	2.734	0.298	10.9	6.136	0.393	6.4	5.547	0.398	7.2	4.525	0.603	13.3	6.099	0.549	9.0	5.100	0.418	0.0	4.050	0.431	10.6	3.582	0.423	11.8	4.516	0.320	7.1	6.749	0.552	8.2
0.142	0.073	51.4	0.186	0.110	59.1	0.096	0.062	64.4	0.070	0.038	53.6	0.150	0.067	44.6	0.107	0.055	51.5	0.063	0.047	75.2	0.154	0.091	58.8	0.713	1.215	0.0	0.134	0.070	52.5	0.122	0.053	43.6	0.110	0.043	39.1	0.151	0.066	43.7
0.440	0.094	21.3	0.746	0.152	20.4	0.357	0.083	23.3	0.332	0.064	19.3	0.418	0.078		0.442	0.092	20.9	0.860	0.120	14.0	0.441	0.084	19.1	0.268	0.060	0.0	0.512	0.098	19.0	0.350	0.063	17.9	0.341	0.056	16.6	0.500	0.090	18.1
957	34	4	1559	62	4	1346	56	4	780	16	2	710	17	2	1032	38	3.7	956	36	4	778	32	4	1234	236	0	1102	27	2	1156	36	3	646	13	2	1197	32	3
1.781	0.329	18.5	2.246	0.471	21.0	2.246	0.424	18.9	2.385	0.332	13.9	0.719	0.188		1.056	0.217	20.5	3.653	0.550	15.1	0.703	0.237	33.6	1.275	0.898	0.0	1.327	0.280	21.1	1.350	0.215	15.9	0.578	0.130	22.6	2.100	0.322	15.3
0.489	0.075	15.3	0.600	0.094	15.7	0.706	0.083	11.7	0.897	0.078	8.7	0.131	0.036	27.2	0.287	0.045	15.8	1.100	0.103	9.4	0.142	0.040	28.2	0.561	0.180	0.0	0.294	0.046	15.7	0.285	0.043	15.0	0.106	0.024	22.5	0.576	0.058	10.1
4.199	0.420	10.0	5.556	0.611	11.0	6.981	0.496	7.1	10.575	0.537	5.1	0.935	0.176	18.9	2.349	0.291	12.4	11.658	0.645	5.5	0.974	0.192	19.7	5.120	1.398	0.0	2.449	0.346	14.1	2.108	0.217	10.3	0.774	0.148	19.1	5.152	0.408	7.9
26.752	0.851	3.2	39.769	1.494	3.8	47.684	1.470	3.1	87.342	1.867	2.1	5.269	0.231	4.4	15.617	0.513	3.3	89.588	2.163	2.4	5.661	0.359	6.3	36.205	8.395	0.0	15.842	0.532	3.4	10.998	0.418	3.8	4.537	0.193	4.3	33.671	1.049	3.1
1.063	0.118	11.1	1.531	0.171	11.2	1.784	0.147	8.2	3.219	0.147	4.6	0.209	0.049		0.643	0.080	12.4	3.398	0.178	5.2	0.236	0.053	22.7	1.413	0.510	0.0	0.577	0.080	13.9	0.431	0.051	11.9	0.171	0.034	19.9	1.286	0.095	7.4
3.506	0.297	8.5	5.163	0.524		5.710	0.433	7.6	11.822	0.553	4.7	0.595	0.123	20.7	2.090	0.259	12.4	11.665	0.713	6.1	0.689	0.134	19.4	4.385	1.453	0.0	1.787	0.236	13.2	1.181	0.151	12.8	0.538	0.101		4.270	0.308	7.2
0.570	0.081	14.2	0.865	0.104	12.0	0.878	0.111	12.7	2.033	0.146	7.2	0.111	0.029		0.365	0.068	18.5	1.828	0.134	7.3	0.110	0.035		0.889	0.321	0.0	0.282	0.055		0.156	0.034		0.088	0.020		0.680	0.062	9.1
3.736	0.416	11.1	6.252	0.717	11.5	6.154	0.463	7.5	15.361	0.725	4.7	0.714	0.173		2.490	0.299	12.0	12.251	0.798	6.5	0.780	0.220		5.065	2.055	0.0	1.897	0.330	17.4	1.098	0.163	14.9	0.561	0.123	21.9	5.082	0.432	8.5
0.592	0.086	14.6	1.024	0.130		0.881	0.095	10.8	2.424	0.121	5.0	0.100	0.035		0.410	0.064	15.6	1.939	0.153	7.9	0.122	0.036	29.9	0.834	0.301	0.0	0.295	0.057	19.3	0.173	0.034		0.092	0.020		0.822	0.090	10.9

*ppm = part per million; 2 SE = internal 2-sigma error; relative percentage (%) = expressed as ((2 SE)/(ppm))*100*

Appendix Table 6. Additional data used in whole-rock construction

	Kyanite	Corundundum	Rutile	Mantle Rutile
Comment	An average compostition taken from 6 samples	An average comopition taken from sample DGO-1	Taken from sample DGO-8	VR19674-g4**
SiO_2	36.5	0.0	0.0	
TiO_2	0.0	0.0	98.0	
Al_2O_3	63.0	99.1	0.4	
Cr_2O_3	0.0	0.1	1.1	
FeO	0.1	0.4	0.0	
MnO	0.0	0.0	0.0	
MgO	0.0	0.0	0.0	
CaO	0.0	0.0	0.0	
Na_2O	0.0	0.0	0.0	
K_2O	0.0	0.0	0.0	
NiO	0.0	0.0	0.4	
Total	99.7	99.7	99.9	
V				
Ni				
Sc				2.6
Rb				32
Th				34.2
U				
Nb				
Ta				
La				0.29
Ce				
Pr				
Pb				
Sr				1210
Nd				470
Sm				
Zr				970000
Hf				
Eu				
Ti				
Gd				
Tb				
Dy				
Y				
Ho				
Er				
Tm				
Yb				
Lu				

*** Data from sample from Aulbach et al., (2011).*

Appendix Table 7. pMelts parameters and data used for forward modelling

Starting composition

SiO_2	51.00
TiO_2	0.35
Al_2O_3	12.10
Cr_2O_3	0.58
FeO	7.40
MnO	0.17
MgO	15.70
CaO	11.50
Na_2O	1.00
Total	99.8

Run	T (°C)	P (kbars	log(10) fO_2	liq mass (gn	wt% SiO2	wt% TiO_2	wt% Al_2O_3	wt% Fe_2O_3	wt% Cr_2O_3	wt% FeO	wt% MnO	wt% MgO	wt% CaO	wt% Na_2O
1	###	10	-3.289	100.00	51.05	0.35	12.11	1.07	0.58	6.44	0.17	15.71	11.51	1.00
	###	10	-3.593	99.78	51.16	0.35	12.11	1.06	0.46	6.44	0.17	15.71	11.54	1.00
	###	10	-3.919	99.59	51.26	0.35	12.11	1.04	0.36	6.43	0.17	15.71	11.56	1.01
	###	10	-4.268	99.42	51.34	0.35	12.10	1.03	0.28	6.43	0.17	15.71	11.58	1.01
	###	10	-4.644	99.27	51.42	0.35	12.08	1.01	0.22	6.42	0.17	15.71	11.60	1.01
	###	10	-5.049	99.12	51.50	0.35	12.06	1.00	0.17	6.42	0.17	15.70	11.61	1.01
	###	10	-5.574	88.44	51.09	0.39	13.13	0.99	0.12	6.50	0.19	13.63	12.82	1.13
	###	10	-6.141	78.42	50.77	0.44	14.31	0.95	0.09	6.38	0.22	11.55	14.05	1.27
	###	10	-7.362	45.38	51.98	0.66	18.74	0.54	0.05	5.46	0.38	7.94	12.31	1.94
	###	10	-8.268	29.37	54.98	0.80	21.46	0.31	0.04	3.95	0.58	5.23	10.12	2.53
	###	10	-8.138	8.03	58.28	1.65	19.84	0.32	0.07	3.17	2.12	3.73	9.13	1.70
	###	10	-8.124	4.57	60.56	1.92	19.03	0.30	0.08	2.41	3.72	2.78	8.11	1.09
	###	10	-8.009	3.18	62.31	1.94	18.48	0.29	0.08	1.70	5.36	2.13	6.98	0.73
2	T (°C)	P (kbars	log(10) fO_2	liq mass (gn	wt% SiO2	wt% TiO_2	wt% Al_2O_3	wt% Fe_2O_3	wt% Cr_2O_3	wt% FeO	wt% MnO	wt% MgO	wt% CaO	wt% Na_2O
	###	30	-0.343	100.0	51.1	0.4	12.1	1.0	0.6	6.5	0.2	15.7	11.5	1.0
	###	30	-0.498	99.8	51.1	0.4	12.1	1.0	0.5	6.5	0.2	15.7	11.5	1.0
	###	30	-0.664	99.7	51.2	0.4	12.1	1.0	0.4	6.5	0.2	15.7	11.5	1.0
	###	30	-0.84	99.6	51.3	0.4	12.1	1.0	0.3	6.5	0.2	15.7	11.6	1.0
	###	30	-1.027	99.4	51.3	0.4	12.1	1.0	0.3	6.5	0.2	15.7	11.6	1.0
	###	30	-1.228	99.3	51.4	0.4	12.1	1.0	0.2	6.5	0.2	15.7	11.6	1.0
	###	30	-1.442	99.2	51.4	0.4	12.1	1.0	0.2	6.5	0.2	15.7	11.6	1.0
	###	30	-1.671	99.1	51.5	0.4	12.1	0.9	0.2	6.5	0.2	15.7	11.6	1.0
	###	30	-1.917	99.1	51.5	0.4	12.1	0.9	0.1	6.5	0.2	15.7	11.6	1.0
	###	30	-2.181	99.0	51.6	0.4	12.0	0.9	0.1	6.5	0.2	15.7	11.6	1.0
	###	30	-2.733	90.1	51.4	0.4	12.7	0.9	0.1	6.6	0.2	14.1	12.7	1.1
	###	30	-3.283	77.5	51.6	0.4	13.0	0.8	0.1	6.6	0.2	11.9	14.2	1.3
	###	30	-4.133	42.3	55.2	0.8	12.4	0.6	0.1	5.8	0.4	8.5	14.5	1.9
	###	30	-4.678	24.2	60.8	1.2	12.3	0.4	0.1	4.1	0.7	5.4	12.6	2.5
	###	30	-4.537	17.6	65.6	1.5	11.8	0.3	0.1	2.7	1.0	3.7	10.7	2.6
	###	30	-4.18	13.6	69.5	1.7	11.0	0.3	0.1	1.8	1.3	2.7	9.0	2.6
	###	30	-4.277	4.1	67.9	2.9	10.7	0.2	0.1	1.4	4.1	2.3	7.6	2.9
	###	30	-4.058	1.8	64.0	4.0	10.2	0.2	0.1	1.2	9.4	2.1	6.8	2.1
	###	30	-3.728	1.1	58.1	5.5	9.6	0.3	0.2	1.0	16.2	2.0	6.0	1.1

Starting composition of sample 26 from (Falloon *et al.*, 1999).